University of Birmingham

A thesis submitted to the University of Birmingham
for the degree of

DOCTOR OF PHILOSOPHY

The role of local versus itinerant magnetism: studies of dilute magnetic semiconductors and multi-k magnets

Joshua A. Lim

July 2013

Condensed Matter Group
School of Physics and Astronomy
University of Birmingham

Abstract

The electronic properties of the materials studied in this thesis; a dilute magnetic semiconductor and a member of the actinide family, are thought to lie on the edge of local and itinerant behaviours. The role of localised versus itinerant magnetism is indirectly explored by characterising the magnetism through a range of experimental techniques.

Reports of magnetism in dilute magnetic semiconductors have been largely conflicting, with most focusing on thin films. This work characterises high quality bulk single crystals of Cr-doped TiO_2 and finds no magnetic ordering down to 4 K. This suggests that the observed thin film magnetisation is a result of non-equilibrium or impurity phases and lattice strains.

In the canonical 3-**k** magnet, USb, the spin waves soften at a temperature, T^* (well below T_N), with no change in magnetic or structural symmetries. It had been suggested that this was due to de-phasing of the different Fourier components making up the 3-**k** state: this was tested using inelastic polarised neutrons and found not to be the case. Instead, the effects at T^* are likely linked to a change in itinerancy. The magnetic domain dynamics are probed using X-ray photon correlation spectroscopy and find changes to the domains near T_N and also T^*.

This work is dedicated to Laura.

Thanks for your love and support.

Acknowledgements

I would like to thank my supervisor, Elizabeth Blackburn (University of Birmingham), for all the support and advice I have received during my PhD (and also proof-reading of this manuscript). I have really appreciated the opportunities to participate in a wide variety of experiments and also travel to international conferences which have broadened my horizons.

I have felt privileged to work with Gerry Lander (Institute for Transuranium Elements) for his insights and discussions on the uranium antimonide project, and from whom I have learned a great deal.

For the work on uranium antimonide, I also thank Roberto Caciuffo (Institute for Transuranium Elements), Nicola Magnani (Lawrence Berkeley National Laboratory) who have provided excellent discussion and ideas. I am also indebted to Arno Hiess (ESS), Louis-Pierre Regnault (ILL), Guillaume Beutier (SIMaP), Frédéric Livet (SIMaP), Alessandro Bombardi (Diamond) for help and valuable input on these experiments.

The XPCS work at the ALS could not have taken place without the help of Sujoy Roy and Keoki Seu (Advanced Light Source); who, despite the experimental problems, made these very useful learning experiences.

The work on the dilute magnetic semiconductor would not have been possible without the excellent samples from Seyed Koohpayeh (now at John Hopkins University) and his work on some of the structural characterisation.

Much of the work for this thesis was carried out at large facilities and I am indebted to the local contacts, in particular Charles Dewhurst and Ralf Schweins (ILL), who have provided unsung technical support. In Birmingham, a special thanks is due to Gary Walsh who can fix anything.

I wish to acknowledge the help of the many technicians who I have worked with (and those who have worked behind the scenes). In addition to learning lots about sample environment and mechanics; these experiments would not have been possible without your hard work. From the ILL, I wish to thank Dave Bowyer, Xavier Tonon and Eddie Lelièvre-Berna; at PSI, Markus Zolliker; at Diamond, Graeme Barlow; and the many other people who have made these places excellent user facilities.

There are also a number of projects I would like to mention that I have been fortunate to work on, which are not directly included in this thesis, but have enhanced my PhD experience.

A special mention goes to Alex Holmes (University of Birmingham), who I've worked on magnetic alignment of molecules and always has a good-humoured and tireless approach to his work with the 17 TF cryomagnet. Also on this project I would like to thank Estelle Mossou and Trevor Forsyth (Keele University) and also Pavlik Lettinga (Forschungszentrum Jülich), who has taught me everything I know about soft condensed matter.

On the vortex lattice in underdoped YBCO project I would like to thank Jon White, Niki Egetenmeyer, Jorge Gavilano (Paul Scherrer Institute) and Toshi Loew (Max-Planck, Stuttgart) who have been a pleasure to work with.

I am grateful to have worked with Ted Forgan (University of Birmingham) whose enthusiasm for physics, hands-on experimentation and puns is infectious.

Back in the office, I would like to thank other members of the the condensed matter group past and present: Georgina Klemencic, Alistair Cameron, Richard Heslop, Bindu Malini, Louis Lemberger, Ling Jia Shen for being absolutely great. A special mention

should also go to my first year tutees throughout my PhD, who provided excellent diversion and opportunity to think and communicate on some basic physics.

I really want to thank my family for all the love and support over the years. I am very grateful to Ian and Mary for opening your home to me while writing up. Finally, I want to say a big thank you to Laura - I couldn't have done it without you.

Contents

Chapter 1

Introduction

1.1 General Introduction

This thesis explores magnetism in two condensed matter systems, by characterising the magnetism through a range of experimental techniques.

In the first system, the relatively young field of dilute magnetic semiconductors, we look at careful growth and characterisation of samples to identify the presence of magnetic order in this sample. Whilst much work has previously centred on thin film samples, we provide a new perspective that is more easily comparable with theory by studying the bulk behaviour.

The second system looks at the canonical 3-**k** magnet, uranium antimonide. In contrast to the dilute magnetic semiconductor work, there have been many measurements characterising this system; however, there remain open questions about the change in characteristics around a temperature, T^*, inside the 3-**k** antiferromagnetic phase.

The motivations and common theme between these two systems lies in the role of local *vs.* itinerant interactions and the effect of this on the magnetic properties. For dilute magnetic semiconductors, it was unclear from the literature whether any derived magnetic properties arose from localised spins or a more band-like interaction.

Similarly, in the actinide compound, USb, the low temperature behaviour has been successfully understood in a localised framework; however the behaviour at higher temperatures is less clear and possibly points towards an itinerant understanding. This thesis work looks indirectly into the nature of this exchange by studying the emergent magnetic properties in these two systems.

For studies of the dilute magnetic semiconductor, the standard structural and magnetic characterisation tools of X-ray diffraction, energy dispersive X-ray analysis, scanning electron microscopy and magnetometry measurements are used. In the work on USb, the probes of inelastic neutron scattering with tri-directional analysis and X-ray photon correlation spectroscopy help bring new insights into the understanding of this system.

The experimental means to study magnetism and a more detailed discussion of the materials' physics will be presented in the respective chapters. In this introduction, the common routes of magnetic exchange in these systems that underpin the observed magnetism, will be highlighted.

1.2 Exchange mechanisms in magnetic systems

In many systems (and indeed the ones studied in this thesis) it is much easier to identify the presence of magnetic order rather than the origin. In a real material, there may be many competing interactions forming the magnetic response, though often these can be broken into simpler isolated models - a few will be discussed here.

For the purposes of constructing models, the different approaches may be broken loosely into two viewpoints: considering the electrons either in a localised or band framework. In the local view, we can imagine distinct electron spins, from various elemental orbitals, sitting at fixed points and interacting with one another: whilst in the itinerant case, we switch to a collective band picture of the electrons with

interactions dominated by the landscape of the Fermi surface(s).

The electronic properties of both of the materials studied in this thesis, a dilute magnetic semiconductor and a member of the actinide family, are thought to lie on the edge of local and itinerant behaviours. I will now break the discussion of mechanisms behind the magnetism into these local and itinerant viewpoints, before discussing some work that combines the two.

1.2.1 Local exchange interactions

The simplest magnetic exchange mechanisms are ones where the electrons can be viewed as being mostly localised: these give typically short range (nearest neighbour or even next nearest neighbour) interactions but can still lead to macroscopic magnetic ordering.

An example is superexchange, where the exchange mechanism is mediated by a non-magnetic ion placed between two magnetic ions [4, 96]. A fixed coupling between the two magnetic ions is favoured depending on the electron occupancies and local symmetry of the system, which can lead to either ferromagnetism or antiferromagnetism (see cartoon in figure 1.1) [61, 81]. Here, it is the virtual hopping of spins that affords a reduction in the exchange energy that favours (anti)-parallel configurations.

These interactions are important in understanding transition metal oxides, where there is magnetism despite the d-orbitals being largely localised and also separated by intermediary atoms (e.g. MnO and $LaMnO_3$).

The double exchange mechanism is superficially similar to superexchange mechanism. Systems with mixed valency (either through occupancy of different lattice sites or chemical doping, which draws comparisons with dilute magnetic semiconductors) can favour electron *hopping* if neighbouring ions are (anti)-ferromagnetically aligned. While this mechanism can be understood in a local framework, this interaction often results in interactions over an extended system and metallic behaviour.

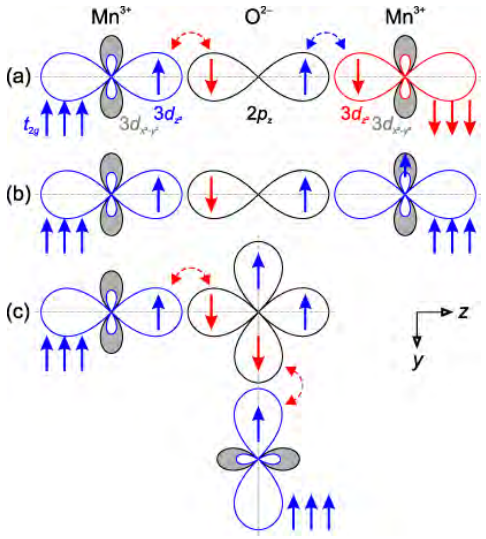

Figure 1.1: (From reference [143]). A cartoon of the superexchange mechanism between the $3d_{z^2}$ orbital of two Mn^{3+} ions and the O^{2-} $2p_z$ orbital. The t_{2g} levels are not shown, but are represented by the group of three arrows. The coupling between neighbouring Mn ions, is dependent on the electron occupancies and the symmetry of the system leading to antiferromagnetic (a) and ferromagnetic exchange (b, c).

1.2.2 Crystal fields

In a real sample, the anisotropy of the crystal often results in easy and hard magnetic axes. These result from the local symmetry of the crystal which can be reflected in the magnetism.

This prompts a discussion of crystal field theory, which describes the break of the electrons' orbital degeneracy. The idea is that interaction between the orbitals states and the surrounding *ligands* leads to an energy splitting of the previously degenerate orbitals.

For example, if an ion containing 10 d-orbitals is surrounded by charges in an octahedral environment (which can be considered to approximate bonding), this causes a splitting in the degeneracy of the orbitals: orbitals that lie closer/further to the charges will have the their energy increased/decreased. This modifies the energy landscape which can lead to changes to the magnitude and direction of the magnetisation.

This crystal field splitting is important for the d and f orbitals, especially if they are extended, as they possess a high angular anisotropy and can interact strongly with the surrounding environment. The crystal field states are dependent on a number of factors, which include the nature of the ion and its oxidation state, in addition to the surrounding arrangement of ligands and their valency [172, 198].

1.2.3 Non-local exchange interactions

One way to introduce a more itinerant picture is to consider the effect of a magnetic impurity on a free electron model. This treatment naturally lends itself to comparison with dilute magnetic semiconductors, where there is a small amount of magnetic dopant in a (semi)-conducting background, although the results are more general.

We switch from a local view describing particular sites and spins, to a broader one by writing down the magnetisation for an electron gas. Considering a single magnetic

impurity in the system as a delta function in field and expanding it in terms of it Fourier modes, one obtains:

$$H(\mathbf{r}) = \delta(\mathbf{r})\mathbf{H} = \frac{1}{(2\pi)^3}\int \mathbf{H}_\mathbf{q} e^{i(\mathbf{q}.\mathbf{r})} d^3\mathbf{q} \tag{1.1}$$

We may play a similar trick and expand the q-dependent susceptibility, χ_q, by Fourier transform and rewrite it in terms of the real space susceptibility, hence [19]:

$$\begin{aligned}
\chi(\mathbf{r}) &= \frac{1}{(2\pi)^3}\int d^3\mathbf{q}\chi_q\, e^{i\mathbf{q}.\mathbf{r}} && (1.2)\\
&= \frac{1}{(2\pi)^3}\int d^3\mathbf{q}\,\frac{\chi_P}{2}\left[1+\frac{4k_F^2-q^2}{4k_Fq}\ln\left|\frac{q+2k_F}{q-2k_F}\right|\right]e^{i\mathbf{q}.\mathbf{r}} && (1.3)\\
&= \frac{2k_F^3\chi_P}{\pi}F(2k_Fr) && (1.4)
\end{aligned}$$

where we consider $r = |\mathbf{r}|$ (i.e. spherical symmetry). Here, k_F is the Fermi wavevector, χ_P is the Pauli susceptibility and $F(x)$ is a function defined as [19]:

$$\chi_P = \frac{2k_Fg^2\mu_0\mu_B^2m_e}{\pi^2\hbar^2} \tag{1.5}$$

$$F(x) = \frac{-x\cos x+\sin x}{x^4} \tag{1.6}$$

The additional complexity in the form of Eqn. 1.3 compared to Eqn. 1.2 is that we consider the effect of the Fermi surface on the free electron gas.

In the large spatial limit ($r \gg k_F^{-1}$) we find $\chi(\mathbf{r}) \propto \frac{\cos r}{r^3}$ and the magnetisation is oscillatory (see figure 1.2).

If we now imagine this spin-polarised electron gas coupled, either ferromagnetically or antiferromagnetically, to another impurity then there is some means of exchange. This particular exchange is known as the RKKY interaction after Ruderman, Kittel, Kasuya and Yosida who first formulated this when considering the effect of a nuclear moment (a sensible approximation to a delta function) on an electron gas and later extended to understand carrier mediated ferromagnetism in metals [83, 156, 196]. It should be noted that this is not a true itinerant magnetism, but presents a long range interaction.

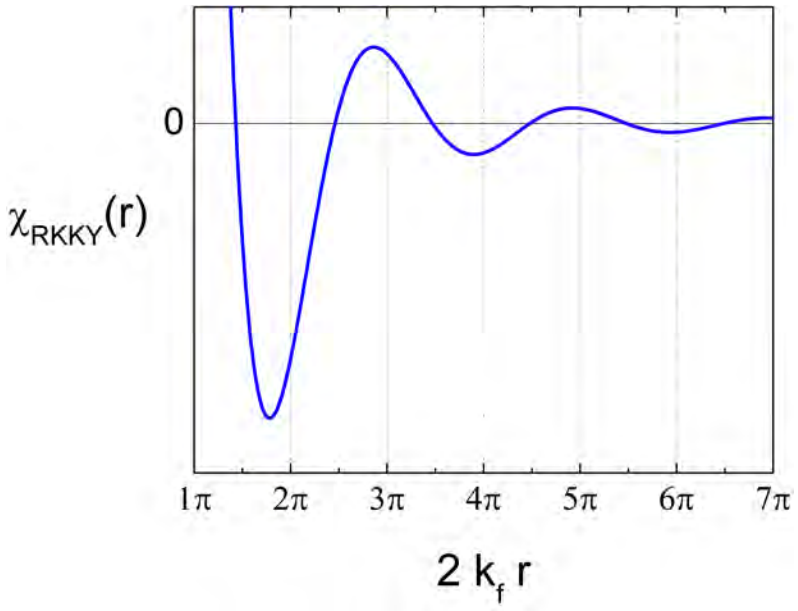

Figure 1.2: The spatial susceptibility of the RKKY interaction showing the oscillatory nature of the magnetisation.

Another route to magnetism in an itinerant system can spontaneously arise due to minimisation of the energy costs between kinetic energy and Coulombic repulsion in a system.

We take a system where there are two bands: one of spin up and one of spin down electrons both equally filled up to the Fermi energy. Now consider a population imbalance and some of the spins are transferred to the spin up band (see Fig. 1.3). This results in a reduction of the Coulombic energy but also an increase in the kinetic energy of the system (as now there are spins in a higher energy state).

If the interplay between these two effects can result in an overall reduction in the energy of the system, then it is energetically favourable allowing the bands to be spontaneously split: this difference in the number of up and down spins results in a net magnetisation.

The determining factors for whether this happens are the density of states at the Fermi level and the associated Coulombic energy which govern the energetic costs

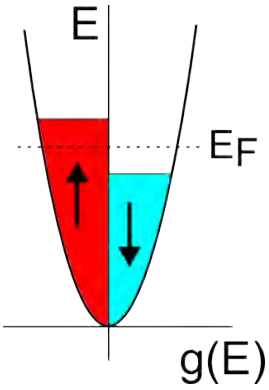

Figure 1.3: Spontaneous spin-split bands can lead to an energy saving by offsetting the increase in kinetic energy, by a reduction in Coulombic repulsion.

of the system. When there is a high density of states near the Fermi level and the Coulombic energy costs is also high, then this favours spontaneously spin-split bands. This relationship is known as the Stoner criterion, which is found in many metallic systems exhibiting ferromagnetism and expressed as:

$$Ug(E_F) > 1 \tag{1.7}$$

where U is the energy associated with Coulombic repulsion and $g(E_F)$ is the density of states at the Fermi level.

1.2.4 Local and itinerant systems

Treating the magnetic behaviour either from a local or itinerant view should not be treated too stringently and is often a matter of conceptual or theoretical convenience. Indeed, in the case of double exchange, which was approached from a local view based on mixed ionisation states, there will also be interplay between the effects of de-localisation and the band structure of the material on this interaction. Therefore in a real system, both local and non-local effects are needed to understand the emergent properties.

In the light actinides (for example, uranium) the $5f$ orbitals are partially extended. This differs from the core-like f electrons in the lanthanides and heavy actinides (Am-Lr), and for the light actinides leads to increased hybridisation with nearby $6d$ and $7s$ bands [52].

The need to reconcile both local and itinerant behaviour is especially important in heavy fermion compounds, such as $CeAl_3$ [5], UPt_3 [40] and UPd_2Al_3 [183]. These materials have localised f electrons that strongly interact with the itinerant electrons creating complicated conduction bands [41, 55]. Dealing with this duality is important in understanding the insulating, metallic, superconducting and magnetic states in these materials.

Chapter 2

$Cr:TiO_2$ - a dilute magnetic semiconductor?

2.1 Introduction & motivations

Dilute magnetic semiconductors (DMS) are materials that are semiconducting and also magnetically ordered due to the inclusion of a low concentration of magnetic dopant in a semiconducting host material. This is potentially interesting for the developing field of spintronics, where the spin, in addition to the charge property of the carriers, is used to carry information. Whilst current electronics (in both meanings of the word) utilise the charge property of the carriers; the idea of spintronics is to use a *spin polarised current* as the basic unit in these circuits and give an extra degree of freedom to enable devices to become smaller and faster.

Attempts to inject a spin polarised current into a semiconductor (by means of a ferromagnet-semiconductor sandwich) have proved difficult due to a low injection efficiency which is heavily governed by small defects on the interface [42, 80] (thus making it hard to commercialize); dilute magnetic semiconductors, where the spin polarisation is intrinsic to the material, could overcome this problem. It is also hoped

a low dopant concentration would not significantly alter the band structure of the host semiconductor, allowing compatibility with existing semiconductor infrastructure [17].

In the last decade, there has been a huge amount of interest in dilute magnetic semiconductors, due to the prediction and subsequent synthesis of *room temperature* dilute semiconductor materials [39, 129] which could be critical for the widespread commercial implementation of spintronic devices.

In addition to the potential technological applications, dilute magnetic semiconducting materials can also exhibit rich and interesting phenomena such as spin glass behaviour, short range antiferromagnetic order, giant Faraday rotation and bound magnetic polarons that make them an interesting field of study in their own right [30, 142, 148].

In spite of the successes in theoretical work and fabrication of dilute magnetic semiconductors, the magnetism found in these samples (which are mostly thin films) varies largely from study to study with different authors citing various mechanisms for the observed ferromagnetic order. It is this discrepancy on the experimental side that this thesis work attempts to address through careful fabrication and characterisation of bulk samples.

2.2 A background to dilute magnetic semiconductors

This section gives the flavour for the main theoretical mechanisms for ferromagnetism in these materials, as well as reviews the transition metal doped TiO_2 group of dilute magnetic semiconductors, particularly noting the wide range of observed magnetic properties and dependence on fabrication technique.

The dilute nature of the magnetic systems makes direct exchange and even some modes of indirect exchange unlikely. For example, mechanisms such as superexchange and Zener double exchange, where hopping to neighbouring atomic sites favours (anti-)

parallel spin configurations due to a kinetic energy saving, are precluded due to low concentrations of magnetic dopant of only a few percent. Interestingly most of the candidate systems considered are oxides, where often the magnetic exchange takes place by these direct routes.

The itinerant nature of some electrons in semiconductors allows the possibility of carrier mediated exchange, which is likely to be important in explaining the long range order that develops in these systems. Whilst a true description of these systems must include the band-like nature of semiconductors, the underlying physics can be demonstrated from the simplified picture of a single dopant and a non-interacting electron gas.

One can imagine extending this idea to a dilute magnetic semiconductor, where we invoke the RKKY interaction (discussed in section 1.2) to explain ferromagnetism (or alternatively antiferromagnetism) in these materials: the magnetic dopant plays the role of the delta function perturbation whilst the electrons (or holes) give the itinerant character of the electron sea.

Phenomenologically, this gives a reasonable idea of what could be going on inside a dilute magnetic semiconductor, but we should be careful of the assumption that the charge carriers are free, which is made in the RKKY model. To accurately model a real dilute magnetic semiconductor, the band like nature of semiconductors should also be taken into account.

An alternative theory for exchange in these systems is based around bound magnetic polarons. This non-itinerant theory requires oxygen vacancies to act as electron donors and also electron traps which can bind the electrons to defects leading to insulating behaviour [78]. These bound electrons may then couple to magnetic spins leading to a bound magnetic polaron with large moment. For a high enough concentration of defects (such that the bound magnetic polaron volumes overlap) and appropriate coupling between spins, the material may order ferromagnetically; this is illustrated in

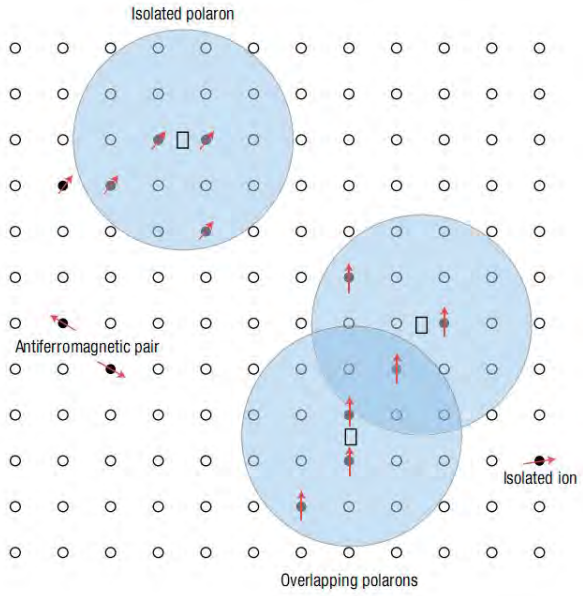

Figure 2.1: Representation of bound magnetic polarons coupling in a material [31]. Oxygen defects are shown as empty rectangles which donate carriers to a volume (large shaded circles) allowing the spins (red arrows) on magnetic sites (black circles) to couple to one another.

figure 2.1.

Although there are other possible mechanisms for magnetism in these systems [30, 33, 38], these two examples highlight the main routes for ferromagnetism: carrier mediated itinerant models (useful for spintronic applications) and localised insulating models. It should be noted that the exact mechanism may vary for system to system and there is no need for a single universal route to dilute magnetic semiconducting behaviour.

2.2.1 Prediction of room temperature ferromagnetism

The recent interest in dilute magnetic semiconductors is largely due to Dietl *et al.*'s theoretical prediction of room temperature dilute magnetic semiconducting materials in 2000 [39]. Whilst interest in magnetic semiconductors has existed since the 1980s [56]

and a lot of work (mainly theoretical) on DMS had gone on prior to this publication, this paper marks the beginning of a surge in synthesis of dilute magnetic semiconducting materials and is a good place to start the story.

Dietl *et al.*'s work was based on a model proposed by Zener to explain ferromagnetism [197]. Zener's model considered localised d-spins coupling to one another via intermediary coupling to carriers. In the DMS system, the magnetic dopants were modelled to play the role of hole donors and also localized spins.

This model was rejected at the time to explain ferromagnetism in metals, as it neglects the itinerant nature of the magnetic spins and does not include Friedel oscillations: both of which are important for a description of magnetism in metals. However, in the case of semiconductors, the Friedel oscillations average to zero as the mean distance between carriers is greater than that between spins.

To calculate the expected Curie temperature, Dietl *et al.* adopted a Ginzburg-Landau framework to approach to this problem. Ginzburg-Landau theory is a phenomenological treatment of second order transitions; although originally employed to deal with superconductors, it can be extended to many other physical systems [60]. The free energy is parametrised in terms of an order parameter (for the magnetic case, this describes the number of ferromagnetically aligned spins) with coefficients setting the energy scale and hence temperature scale for the system.

In their calculation, contributions to the free energy from carriers and localised spins were included, using values for input parameters derived experimentally (where available) and theoretically. By minimising the free energy with respect to the magnetisation at a given temperature and carrier concentration, it was found that the Curie temperature is determined by competition between ferromagnetic and antiferromagnetic interactions and was strongly dependent on the level of doping and hole concentration. The calculated values showed good agreement with some experimentally measured Curie temperatures.

The mechanism is that ferromagnetic correlations are mediated by holes that come from acceptors in a matrix of magnetically doped semiconductor. It was also suggested from this mean field calculation that Curie temperatures above room temperature were possible in several materials, where there was larger hybridisation between *p*-*d* bands and also a reduction in spin-orbit coupling.

2.2.2 Experimental review of dilute magnetic semiconductors

This review will focus on transition metal doped titanium oxide samples as these have been widely studied and can also have high Curie temperatures - attractive for potential spintronic applications. There are many designs and ideas for transition metal oxides such as transparent electronics, UV light emission, gas sensing, varistors, surface acoustic wave devices, magnetic FETs and low threshold spin-lasers [54, 148, 157, 159, 160].

Titanium dioxide has three mineral forms, with rutile and the thermodynamically less stable anatase, being the most common. Whilst large single crystals (useful for understanding electron transport properties and magnetic correlations) of rutile may be produced; anatase with high crystallinity is stable in thin film form only. The structures of rutile and anatase are shown in figure 2.2.

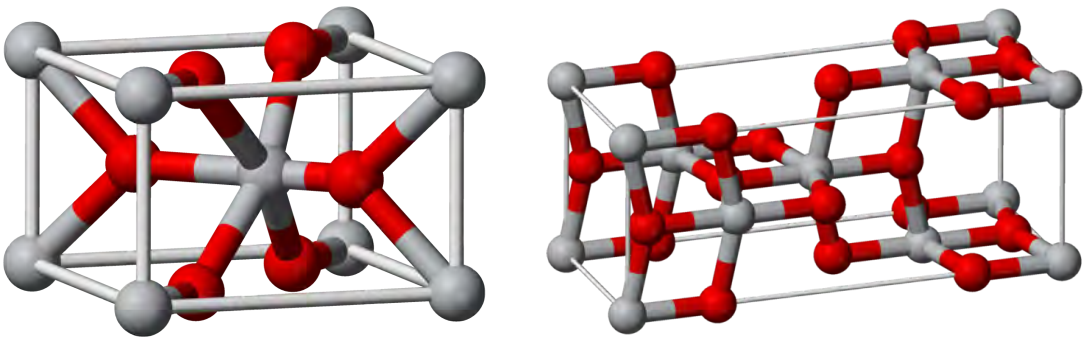

Figure 2.2: The crystal structure of rutile (left) and anatase (right) with the Ti atoms in grey, O atoms in red (from [132])

Thin film work

The first report of room temperature ferromagnetism was the serendipitous discovery in Co-doped TiO_2 in anatase thin film form by Matsumoto *et al.* in 2001 [129].

The $Co_xTi_{1-x}O_2$ samples were fabricated using molecular beam epitaxy using two different substrates, with a range of cobalt concentrations ($0 < x < 0.08$) showing no evidence for impurity segregation when looked at using a tunnelling electron microscope (TEM). Using TEM and X-ray diffraction (XRD) no structural second phases were observed.

SQUID microscopy and magnetic measurements showed evidence for ferromagnetism in the imaging of domains and observation of hysteresis loops, respectively. Data analysis suggested that the ferromagnetism in Co-doped TiO_2 is due to local cobalt spins, although a model for the coupling between ions was not put forward.

Following this work, many other groups looked at Co_x:TiO_2 anatase to try to elucidate the mechanism behind the ferromagnetism: however, the results are somewhat at odds with one another.

For example, Balagurov *et al.* [9] grew their samples by magnetron sputtering of an alloyed metal target and found the moment per cobalt ion to be $0.57\mu_B$ in the anatase form (compared to the $0.32\mu_B$/Co as reported by Matsumoto *et al*). By varying the concentration of oxygen, the resistance would change (by $\sim$4 orders of magnitude) with little effect on the observation of ferromagnetism: this largely resistance independent behaviour led the authors to the conclusion that a carrier mediated explanation of ferromagnetism is not needed. In all studies effort was made to rule out second phase inclusions.

On the other hand, Chambers *et al.* again found ferromagnetism in thin film Co_x:TiO_2 grown using oxygen plasma assisted molecular beam epitaxy (MBE) [24]. They found that increasing the cobalt concentration led to the samples changing from

ferromagnetic n-type semiconducting (with moments 1.2-1.4 μ_B/Co) to insulating non-magnetic, indicating that the transport properties are important to the magnetism in this system.

The picture becomes less clear with other transition metal-doped TiO_2 systems as there are fewer available studies. However, the story remains similar with different groups' findings conflicting with one another. In the case of Cr-doped TiO_2; Matsumoto *et al.* found that Cr_x:TiO_2 grown by pulsed laser deposition (PLD) was not ferromagnetic [128], whilst Wang *et al.* found that oxygen deficient rutile Cr_x:TiO_2 (also grown by PLD) was a room temperature ferromagnet with a large magnetic moment of 2.9μ_B/Cr [191].

Other studies by Droubay *et al.* found Cr_x:TiO_2 grown by MBE to be ferromagnetic insulators [43] and Kaspar *et al.* found that high crystallinity *reduced* the ferromagnetism in MBE grown Cr_x:TiO_2 [82]. Other transition metal doped samples [21, 151] have reported a similar requirement on defects for ferromagnetism to occur, raising questions behind the mechanism of ferromagnetism in dilute magnetic semiconductors that remain unexplained.

The possible mechanism behind ferromagnetism in these samples is further compounded by a report that room temperature ferromagnetism could occur in $TiO_{2-\delta}$ films *without* any magnetic dopant (T_c = 880 K)[195]. The magnetism was found to scale with conductivity suggesting carrier mediated ferromagnetism, but calls into question the role transition metal doping has in other studies. Here, it was put forward that anion defects on oxygen sites, brought about by a lattice-substrate mismatch and processing in an oxygen deficient environment, played an important role in the observation of ferromagnetism.

Bulk dilute magnetic semiconductors

Whilst much attention has been given to thin film preparation of samples, there are comparatively few studies that look at bulk single crystals; where effects such as lattice strain from the substrate and non-equilibrium growth, typical of thin film preparation, do not play a role.

Sangaletti *et al.* grew various transition metal doped TiO_2 bulk single crystals by the flux method using a $Na_2B_4O_7$ flux and obtained needle-shaped rutile single crystals, approximately 0.1 x 0.05 x 5.0 mm^3. They found room temperature ferromagnetism for all samples, including Co_x:TiO_2 and Cr_x:TiO_2, and although there was no detailed discussion of Cr_x:TiO_2, the coercive field was reported to be $\sim$ 50 Oe [158]. The samples grown were non-transparent and dark, indicative of oxygen vacancies and the authors could not rule out low amounts of contamination of the small sample volume during the growth method.

Koohpayeh *et al.* also looked at bulk single crystals of Co_x:TiO_2 grown by the floating zone method (see section 2.4.1) [92] and found that in contrast to Sangaletti *et al.*'s findings, growth in oxygen deficient environment led to ferromagnetism due to cobalt clusters with growth in an oxygen rich atmosphere destroying the ferromagnetism. An advantage of the float zone method over the flux method is that the need for a crucible is eliminated, reducing the risk of contamination, and also larger single crystals can be obtained using the float zone technique.

Overview

Following the theoretical prediction of room temperature ferromagnetic dilute magnetic semiconductors and the subsequent menagerie of experimental data, no encompassing model is able to explain the behaviour of these materials: however, it is clear that, in addition to the conduction properties of the materials, the local environment (structural

and chemical defects) plays an important role in the origin of ferromagnetism.

Additionally, to isolate the intrinsic behaviour occurring in these materials, careful control and understanding of the differences in sample preparation is needed (growth method, substrates, growth parameters, post-annealing processes etc.).

2.3 Motivation & aims

This work looks at the behaviour of bulk single crystals of chromium doped rutile $Cr_xTi_{1-x}O_2$ (with x = 0.02, 0.04, 0.08 and 0.12), and explores the effect of doping on their structural and magnetic properties. In particular, it would be of interest to identify deformation of the lattice with doping (effects such as change in lattice parameter/symmetry, second phase inclusions, etc.) in addition to seeing whether Cr_xTiO_2 is ferromagnetic.

Chromium was chosen as the magnetic dopant as there would be no spurious ferromagnetic signal due to clustering of the dopant (chromium is an antiferromagnet in bulk). Chromium also has a relatively high solubility limit ($\sim$ 6wt.%) into the TiO_2 rutile structure [178, 117], which in addition to the near equilibrium growth technique of the float zone image furnace, should limit second phase inclusions. The phase diagram is shown in figure 2.3.

One should note that CrO_2 is a ferromagnet (which also crystallises into the rutile structure), however if present, it can be distinguished from the TiO_2 host by measuring the lattice parameters using X-ray diffraction [173]. Furthermore it should undergo an irreversible transition to Cr_2O_3 during the sintering process [154].

From the literature, most of the Cr_xTiO_2 thin film work has focused on the anatase structure, although both polymorphs have shown evidence for ferromagnetism [43, 72, 82, 119, 191], albeit having varying magnetisation dependencies on the concentration. The electronic properties of the two structures differ, however only the more stable

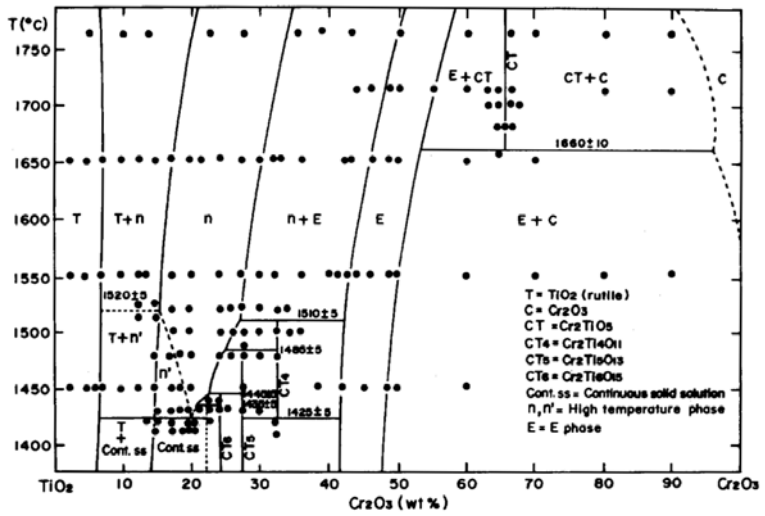

Figure 2.3: Structural phase relations of the TiO_2-Cr_2O_3 system with respect to doping and temperature (from reference [178]).

rutile form can be fabricated using the float zone method.

The crystal growth and some of the characterisation was done in collaboration with S. Koohpayeh (formerly of Metallurgy and Materials, University of Birmingham) and was looking to build on a similar study of bulk Co_x:TiO_2 grown by the float zone method [92].

The main aim was to establish whether high quality Cr_x:TiO_2 bulk rutile single crystals, prepared by the float zone method, were actually ferromagnetic or whether the result was particular to the flux method growth of Sangaletti *et al.* [158]. The properties of these well-characterised bulk single crystal samples, present a more direct and simpler link with theory than thin-film samples.

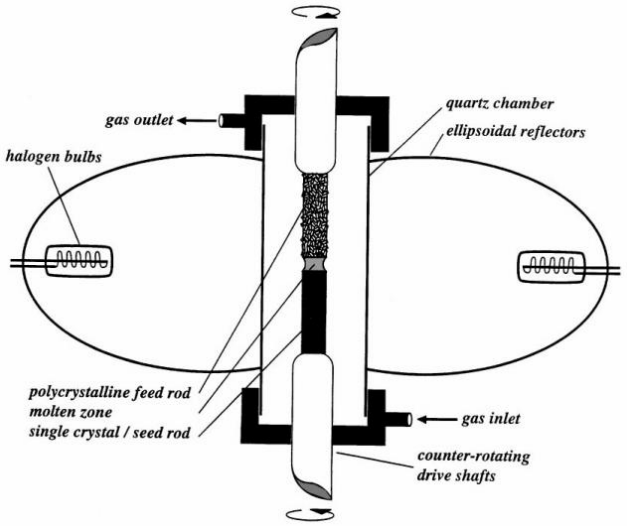

Figure 2.4: Schematic of the float zone image furnace growth [57]

2.4 Methods

2.4.1 Floating zone crystal growth

The float zone image furnace method enables growth of large single crystals in near-equilibrium conditions, as opposed to the non-equilibrium growth typical of thin-film preparation. In contrast to Czochralski or flux methods for bulk growth, float zone growth eliminates the use of a crucible and the associated potential contamination, which is critical due to the small volume and low dopant levels of the fabricated sample. This makes the float zone technique an excellent candidate for study of bulk dilute magnetic semiconductors.

The operational concept behind the image furnace is that mirrors focus light onto a vertical rod of sample to create a small molten zone (the setup is shown in figure 2.4). The sample is then slowly moved upwards; simultaneously adding more new material to the molten zone in the direction of travel, while allowing single crystal to solidify behind. The recently solidified single crystal acts as a seed for subsequent sample solidification allowing single crystals of $\sim$100 mm to be grown.

There are a large number of variables that can be altered which affect the quality of crystal growth, such as:

- **heater power:** this must be tuned to create the molten zone, keep it stable against collapse and also limit evaporation of material from the rod.
- **crystal scan speed:** generally a slow rate ($\sim$10 mm hour^{-1}) gives a planar growth front and a more homogeneous composition. However, in some cases, depending on the the samples phase stability, faster growth rates (up to 240 mm hour^{-1}) are required to limit second phase inclusions [91].
- **growth atmosphere and pressure:** changing this can limit evaporation of sample material, access different parts of the phase diagram and allow for different crystal structures. It can also lead to bubble formation in the molten zone and cracking of the sample.
- **sample rotation speed**: rotating the feed rod or seed rod (which can be done independently) can facilitate more homogeneous mixing and allow for even heating of the molten zone but also can introduce defects into the grown crystals (such as bubbles and low angle grain boundaries) [92].

It should be noted that these variables are not independent nor linear. For example; increasing the pressure increases the melting temperature required, hence heater power (which is itself a function of the materials absorption properties). A combination of experience/trial & error is needed to control the molten zone and grow quality single crystals.

Prior to growth a feed rod must be prepared. This is done by taking the stoichiometric quantities of the starting materials, shaping them into rods (roughly 70 mm in length and 6 mm in diameter) and compacting via hydraulic press. The powders were calcined at 1400°C for eight hours in a controlled air or argon atmosphere. This

sintered polycrystalline rod is then ready to be used for growth or part of it can be used for magnetic/structural characterisation.

2.4.2 Structural characterisation methods

Diffraction is a powerful tool in probing periodic crystal environments. Several different setups were used to look at the samples; however, the underlying principle of Bragg diffraction is common to them all[1]. Constructive interference occurs at the Bragg condition and is given by $2d\sin\theta = n\lambda$, where d is the spacing between planes, θ is the angle between the incident beam and the crystal planes, n is an integer and λ is the wavelength of the radiation [65].

Four circle X-ray diffraction (XRD) allows the incident angle of the beam and a single crystal sample to be orientated to match the Bragg condition. By rotating sample and detector to access different crystal planes where the Bragg condition is fulfilled, the dimensions of the crystal (including angles between lattice vectors) and symmetry can also be found.

In powder diffraction, where the crystal planes are orientated in random directions, the detector angle is scanned resulting in an intensity versus angle plot. The task is then to identify the different Bragg peaks corresponding to different planes within the crystal(s) and also the presence of other crystalline phases.

Laue diffraction can be used to check for single crystals and also to orientate a sample. The sample is illuminated with X-rays and the diffracted intensity is captured by an area detector (either a CCD or photographic film). In the case of a single crystal there will be many *distinct* Bragg spots (see figure 2.5) and for the case of a powdered sample there will be a ring/Debye-Scherrer cone (corresponding to isotropic orientation of the crystal lattice). Intermediary cases of a sample made of a few crystal grains can

[1] The details of Bragg diffraction by X-rays are assumed and will not be discussed here. Introductory texts found in references [11, 65, 122], give a good introduction into this area.

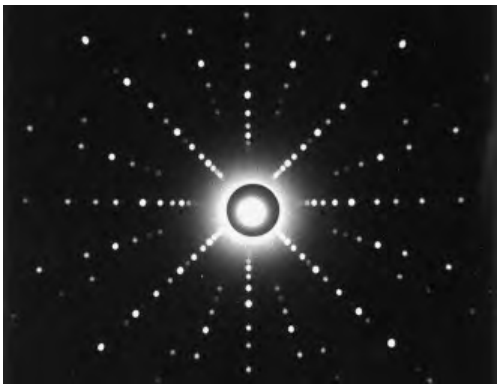

Figure 2.5: A Laue diffraction image of a single crystal of $MoSi_2$ with spots corresponding to scattering from different planes (from [168]). The four fold symmetry is from reflections along [0 0 1]-like directions.

also be resolved.

TiO_2 rutile has space group P42/mnm and is tetragonal [62] so the crystals were cleaved along the principal a and c axes. This was to ease alignment for magnetisation measurements along these axes, where some anisotropy/easy axis might be present.

Scanning electron micrographs were made of the float zone grown crystals and the compositional homogeneity was checked using energy dispersive X-ray spectroscopy (EDX) with a scanning electron microscope (this was done by S. Koohpayeh).

2.4.3 Magnetometry measurements

It was important to characterise the magnetic properties prior to single crystal growth (i.e. the sintered rods) in addition to the float zone grown single crystals. The *MPMS*© (magnetic property measurement system) SQUID magnetometer by *Quantum Design*© allowed measurements of the DC moment and AC susceptibility of samples from 5 K to room temperature and thus gave a large parameter space to look for evidence of magnetism.

Of obvious interest would be measuring $\mathbf{M}$ *vs.* $\mathbf{H}$ curves to give evidence for ferro-

magnetism with a characteristic hysteresis loop, but it would also be useful to cool the samples to see if a ferromagnetic (or even antiferromagnetic) component developed in the DC magnetisation or AC susceptibility.

The *MPMS*© measures the DC moment by moving the sample through superconducting pickup loops which changes the flux through the loop. This results in a change in current which is coupled out to a pre-amplifier stage via a flux transformer then measured by a SQUID detector. A measurement will comprise of many such readouts at each sample position to give better averaging. The superconducting nature of the SQUID sets the measurement scale down at the flux quantum which will be mitigated by electrical, magnetic and thermal noise. AC magnetic susceptibility measurements can can also be made by applying a small oscillatory field and measuring the dynamic magnetic response.

Data was gathered using the *MPMS*© *Multiview* Software© which automated control of the data acquisition and the sample environment.

2.5 Results & discussion

There are three main parts to the results section: the growth of the $Cr_xTi_{1-x}O_2$ samples, structural characterisation and magnetic measurements.

2.5.1 Crystal growth

The feed rod was prepared by taking the stoichiometric quantities of TiO_2 (99.9 % in rutile and anatase forms) and Cr_2O_3 (99 %) to give x = 2, 4, 8 and 12 % concentrations of Cr_x:TiO_2; making them into rods (roughly 70 mm in length and 6 mm in diameter) and compacting via hydraulic press. The powders were calcined at 1400°C for eight hours in either air or argon atmospheres. The polycrystalline rods were then characterised in terms of their structural and magnetic properties and also used for

feed in float zone growth.

The crystals were grown using a four mirror float zone furnace (*Crystal Systems Inc.*© FZ-T-10000-H-VI-VP) with four 1 kW halogen lamps as the heating source. Single crystal TiO_2 were used as feed rods. A growth rate of 25 mm/hour without rotation of the feed or seed rod shaft provided a stable growth environment. It was found that growth in air (at a range of pressures) led to evaporation of material, with deposition on the surface of the growth chamber blocking further growth. Float zone growth was successfully conducted under a 1 bar argon atmosphere.

2.5.2 Structural characterisation

Phase identification of the polycrystalline $Cr_xTi_{1-x}O_2$ feed rods using XRD (see figure 2.6a) showed that for $x = 0.02$ & 0.04 there was no noticeable shift in the peak positions, implying conversion to the rutile structure and no evidence for other phases.

For higher Cr concentrations, unidentified secondary phase peaks in the XRD pattern are apparent with increasing concentration of dopant. These secondary phase reflections are consistent with published data on $Cr_{0.12}Ti_{0.78}O_{1.74}$ [50].

The float zone grown samples were powdered for XRD phase analysis. In figure 2.6b, the 2 at.% and 4 at.% Cr samples appear to be rutile only and in the case of the 8 at.%, the intensity of the peaks corresponding to secondary phases is reduced. It is unclear whether there is any relative intensity change of the secondary phase to rutile in the case of the 12 at.% sample.

X-ray Laue diffraction taken across various cuts through the sample length showed the 2-8 at.% crystals to be of high crystalline quality with evidence for microcracks in the 12 at.% sample. The samples were measured using four circle XRD and no detectable change in the lattice parameter was observed. This implies chromium substitution into the rutile matrix with little structural distortion and below the resolution limit of the X-ray setup (<0.05 Å).

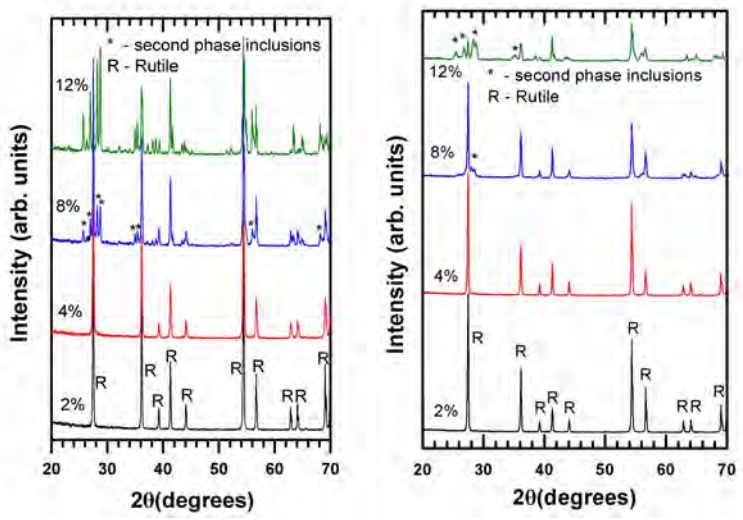

(a) Sintered feed rods (b) Float zone grown samples

Figure 2.6: XRD from a) sintered feed rods and b) float zone grown samples of $Cr_xTi_{1-x}O_2$ (with x=0.02, 0.04, 0.08 & 0.12) in an argon atmosphere plotted on a linear scale. Synthesis in air gives the same XRD pattern for a), but prevents growth for b).

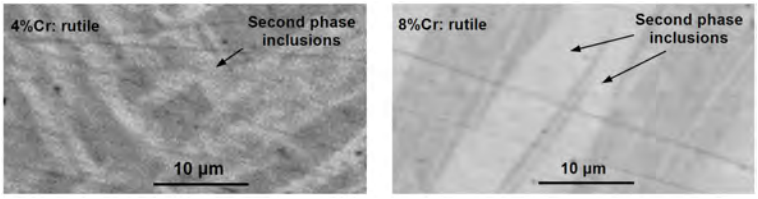

Figure 2.7: Scanning electron microscope backscattered micrographs showing cross sections of polished sections float zone crystals with 4 & 8 at.% Cr. The second phase inclusions appear white in the figures.

Whilst powder XRD did not give any evidence for second phases in the 4 at.% samples, scanning electron microscope backscattered micrographs show evidence for inclusions (see figure 2.7). Energy dispersive X-ray spectroscopy (EDX) analysis shows the second phases to have chromium contents of ∼5-6 at.% Cr relative to Ti (white regions in figure 2.7) with chromium concentration in the rutile portions ∼3 at.%. Scanning electron microscope data for the 8 at.% crystal showed the larger second phases to have a higher chromium content of 13 at.% Cr.

2.5.3 Magnetic characterisation

Sintered powders

Preliminary magnetisation measurements were made on the sintered samples and are shown in figure 2.8. There is evidence for ferromagnetism in both preparation atmospheres (air and argon) and whilst both have similar paramagnetic backgrounds, larger coercive fields were seen in the sample prepared in air. The coercive field decreased with increasing Cr content in both cases.

The source of the weak ferromagnetism in these samples is hard to pinpoint, although some second phase inclusion below the resolution of XRD is likely. Ferromagnetic CrO_2 clusters should not be present as an irreversible transformation to Cr_2O_3 should have occurred during the sintering process [154].

Cr:TiO_2 float zone grown crystals

Magnetisation *vs.* field curves for the 2-8 at.% Cr were measured at room temperature (on a vibrating sample magnetometer) and at 5 K (using the *MPMS*©) along the a and c crystallographic directions and did not show evidence for ferromagnetism (see figure 2.9). Paramagnetic behaviour was observed and was fitted using the Brillouin function [19]. Some anisotropy was noticed between the a and c axes and will be discussed

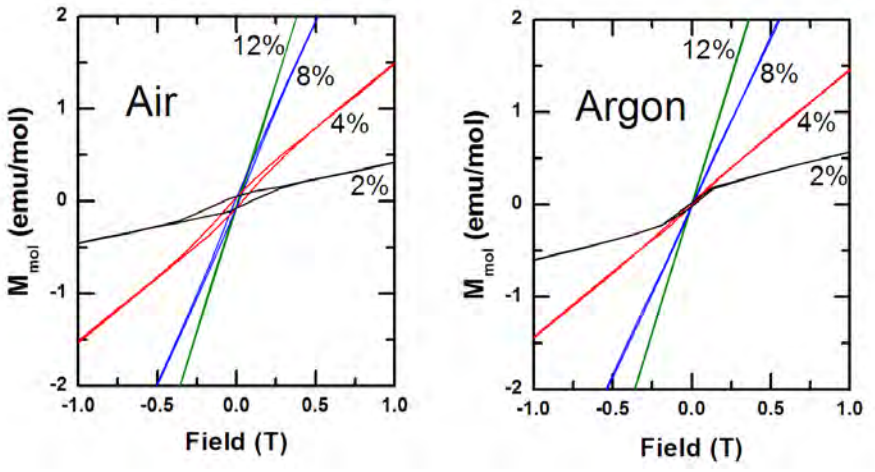

Figure 2.8: Magnetisation measurements of the 2-12 at.% Cr-doped TiO_2 sintered powder by synthesis in air and argon taken at 300 K.

later. It is interesting to note that whatever the cause of the ferromagnetism present in the sintered powders, this effect was removed after float zone growth; presumably as trace amounts of unidentified secondary phase were converted to rutile.

A Brillouin function describes the paramagnetic response for an ensemble of electrons with total angular momentum (**J**) and gives for the magnetisation:

$$M(\mathbf{H}) = M_S B_J(\mathbf{H}) \tag{2.1}$$

where M_S is the saturation magnetisation and B_J is the Brillouin function [19]. The saturation magnetisation is given by:

$$M_S = n g_J \mu_B \mathbf{J} \tag{2.2}$$

where n is the number of moments per unit volume and g_J is the Landé g-value for the electron. The Brillouin function depends on the the total angular momentum (**J**), temperature, Landé g-value, applied field (**H**), and has the form:

$$B_J(H) = \frac{2\mathbf{J}+1}{\mathbf{J}} \coth\left(\frac{2\mathbf{J}+1}{2}\frac{g_J \mu_0 \mu_B H}{k_B T}\right) - \frac{1}{2\mathbf{J}} \coth\left(\frac{g_J \mu_0 \mu_B H}{k_B T}\right) \tag{2.3}$$

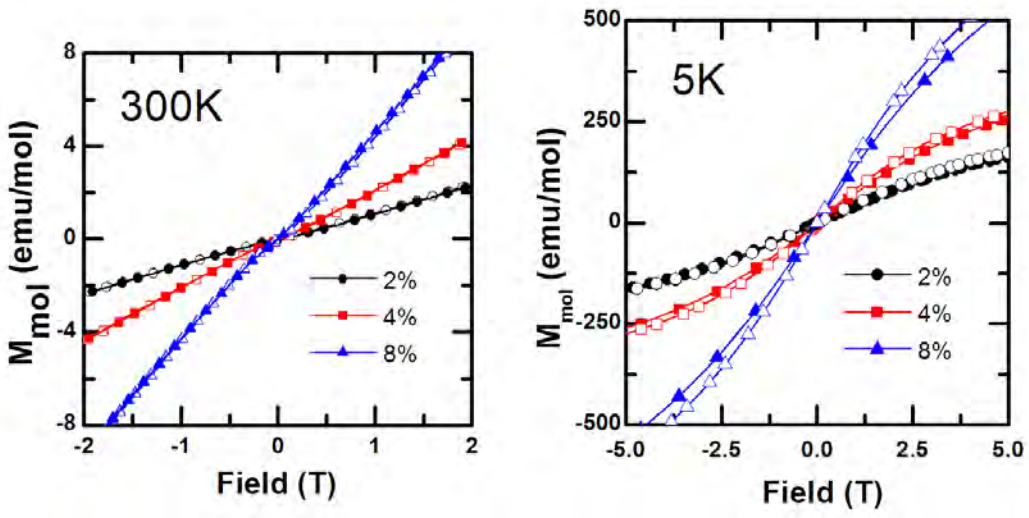

Figure 2.9: **M** *vs.* **H** measurements of the 2-8 at.% Cr-doped TiO_2 float zone grown crystals along *a* (open symbols) and *c* (closed symbols) crystallographic directions at 300 K and 5 K. Points have been omitted for clarity.

The experimental data was fitted using two Brillouin functions simultaneously consisting of the likely contributions to the paramagnetic response from the sample: one Brillouin function corresponding to substitution of Cr^{4+} ions for the Ti (where $\mathbf{J} = 1$) and the second contribution from Cr_2O_3 inclusions (where $\mathbf{J} = \frac{3}{2}$).

The expected oxidation states were determined by considering a 2^- valence on the O ions and charge neutrality. The Cr atom, with ground state configuration [Ar] $3d^5\ 4s^1$, if directly substituted for Ti would form CrO_2 and hence be Cr^{4+} with electron configuration [Ar] $3d^2$ and $\mathbf{S} = 1$ by Hund's rules considerations. Similarly, the second phase Cr_2O_3 would give rise to a [Ar] $3d^3$ and a Cr^{3+} configuration with $\mathbf{S} = \frac{3}{2}$.

Implicit in the assumptions for the choice of **J** was that the orbital angular momentum, **L**, was quenched for the Cr ions (i.e. $\mathbf{L} = 0$ and hence $\mathbf{J} = \mathbf{S}$). This is a sensible and common approximation for ions with 3d electrons, but as we will see later spin-orbit coupling may play a role and we cannot completely ignore **L**.

It was assumed that only a chromium contribution to the magnetic signal was

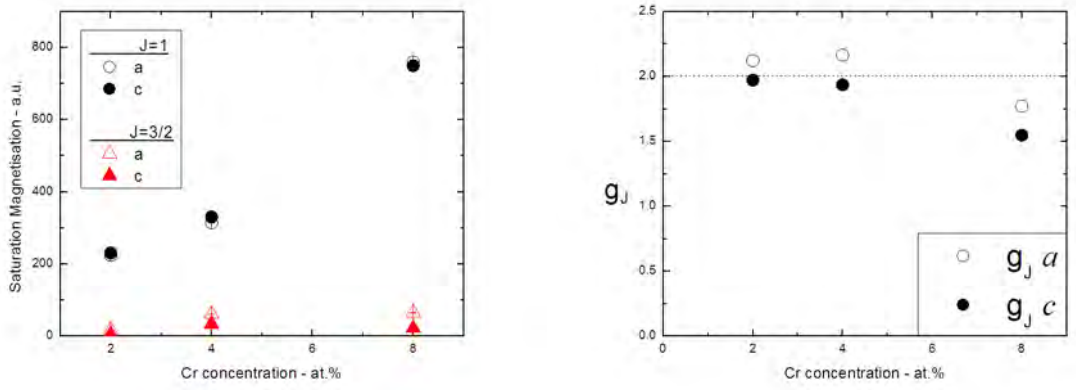

Figure 2.10: Extracted parameters from Brillouin fit to the magnetisation data (with error bars shown). Left panel: results from fitting saturation magnetisation showing the contributions from **J**=1 and **J**= $\frac{3}{2}$. Right panel: results from g_J fit (dashed line is g_J value for a fully quenched system).

present, which is consistent with the very weak paramagnetic signal that was measured from pure TiO_2. The TiO_2 measurement was used as a background and subtracted from all Cr-doped TiO_2 data after appropriate scaling for mass.

The data was fitted in *Origin*® (a data graphing and analysis software environment) using a Levenberg-Marquardt fitting algorithm with $\mathbf{J} = 1$ and $\mathbf{J} = \frac{3}{2}$ and the free parameters as the saturation magnetisation of each **J**-component.

The results of this fit are shown in the left panel of figure 2.10, which show the sample to be largely made up of $\mathbf{J} = 1$ with small amounts of $\mathbf{J} = \frac{3}{2}$ present in the 4 and 8 at.% samples. The $\mathbf{J} = 1$ amplitude scales roughly linearly with increasing Cr concentration, indicative of chromium incorporating into the rutile structure with increased doping.

Using the known mass of samples, it was possible to convert the saturation magnetisation into the magnetisation per Cr atom. It was found that the magnetisation was $1.9 \pm 0.2\mu_B$ per Cr atom: as expected for this oxidation state [33].

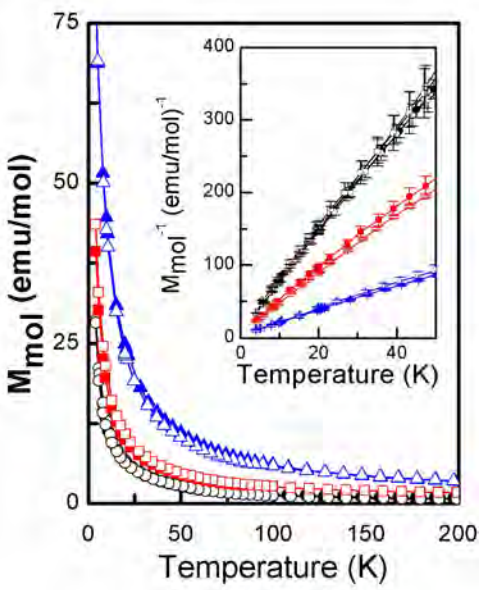

Figure 2.11: The temperature dependence of magnetisation measured in 0.1 T. Inset: inverse magnetisation as a function of temperature. Points were omitted for clarity.

For a paramagnet, one expects the saturation magnetisation to be independent of orientation. It was postulated that the difference observed arose from some anisotropy of g_J and to extract this; the saturation magnetisation was held fixed (at the mean value of the magnetisation obtained from the previous fit) for each concentration with g_J as the only free parameter.

The results for the $\mathbf{J} = 1$ fit are shown alongside a dashed line showing the expected value in the right panel of figure 2.10. The anisotropy ratio, g_J^a/g_J^c was 1.1 and 1.3 for $\mathbf{J} = 1$ and $\mathbf{J} = \frac{3}{2}$, respectively.

The physical motivation for this correction was to account for the earlier assumption that the orbital angular momentum was completely quenched. Whilst this approximation is supported by close agreement in the fits, if the angular momentum is only partly quenched and some finite $\mathbf{L}$ exists (i.e. $\mathbf{L}\neq 0$), then the spin-orbit interaction may be included as a perturbation to mix in states with non-zero angular momentum.

This can result in a quenched ground state but a g-factor that is not exactly equal

to the value of 2, as expected for the $\mathbf{L} = 0$ state [19]. In this Cr-doped system, the anisotropic g-factor is attributed to some spin-orbit coupling of the Cr ions with the local crystal field environment of the rutile lattice.

Measurements on the temperature dependence of the magnetisation (see figure 2.11) show the sample to be paramagnetic down to low temperatures, rising asymptotically at T = 0 K. No anisotropy was measured in the low applied field of 0.1 T. Thermal and field cycling had no effect on the values of the temperature curves.

AC measurements were difficult to obtain due to the small paramagnetic signal, but showed no evidence for a phase transition at finite temperature, including at the antiferromagnetic ordering of Cr_2O_3 at $T_N = 307$ K (where T_N is the Néel temperature) [35].

2.6 Conclusions, impact & outlook

Sintered powder rods of Cr-doped TiO_2 showed weak ferromagnetism when prepared in air and argon, with a smaller magnetic hysteresis from processing in an oxygen deficient environment. The ferromagnetism in these polycrystalline samples decreased with increasing Cr concentration, which also had the effect of introducing secondary phases. The source of ferromagnetism in these samples is unidentified and disappeared after float zone growth.

High quality single crystals were grown using the float zone method and characterised using powder XRD, Laue diffraction, four axis XRD, SEM, EDX and also magnetometry measurements. This showed the 2 at.% Cr doped TiO_2 to be free of second phase inclusions, with a growing amount of inclusions on higher doping. A complementary use of techniques led to a rounded understanding of the structural characteristics of the samples.

The magnetisation data was fitted using the Brillouin function and this identified

the compositional contributions from primary & secondary phases. The results showed good agreement with the expected ionisation states and g-factor for Cr substituting for Ti in the rutile structure. Anisotropy in the magnetisation was observed and this was attributed to spin-orbit coupling of the chromium moments with the tetragonal lattice resulting in anisotropy of the Landé g-factor.

It appears that if ferromagnetism does occur in Cr:TiO_2 then it must be a non-equilibrium effect peculiar to thin films and not bulk single crystals. This conclusion is well supported by the disappearance of ferromagnetism in the sintered powders (where *apparently* no secondary phases were present) after float zone growth which seems to have effectively annealed away these *defects* (possibly made of unknown secondary phases, oxygen deficiencies or strain). Importantly, we show no ferromagnetic ordering in bulk Cr:TiO_2 single crystals at any temperatures in contrast to previously published work looking at this system [158]. As no ferromagnetic component was measured, it is not possible to comment on the role of local versus itinerant magnetism in this system.

This work is unable to answer what makes a dilute magnetic semiconductor, but does make an important and already well known point: the physics occurring in thin films is subtle and often hard to translate from bulk theoretical predictions. This mismatch between theory and experiment is in the process of being readdressed, with studies that include the crucial ingredient of *disorder* now taking place [23, 33, 34]. In particular, recent theoretical work has specifically looked at the origin of magnetism in Cr-doped TiO_2 rutile and anatase systems, with focus on the role of oxygen defects [33], however the results for rutile are not fully clear.

Since the publication of this work[2], there have been other studies that show ferromagnetism in similar oxide samples is largely a characteristic of their film nature. This is demonstrated most clearly in the studies where ferromagnetism is explored in

[2]This work was published in the Journal of Applied Physics [94] and has since been cited six times as a clear example of an ideal bulk transition metal doped oxide [33, 93, 124, 146, 147, 174].

undoped TiO_2 films [174, 195]. Our work supports the picture that the observed magnetism is not a bulk phenomenon, but is instead possibly related to oxygen content [6, 13, 48] .

In this thesis work, the conductivity properties of the samples have not been studied. In many semiconductors, solubility of electronic or magnetic dopants is generally not conducive to coexistence of carriers and spins in high densities - this creates a further obstacle in the development of practical applications. In the search for practical dilute magnetic semiconducting devices it has been assumed that single phase magnetic materials are needed, however, there may be potential for multi-phase materials in magneto-optical applications [148].

Taking a wider look at the field; following the bursting (or rather slowing) of the dilute magnetic semiconductor *bubble* in recent years, the focus of dilute magnetic semiconductor research has switched from a race to high T_c to a more careful characterisation of growth and property measurement of samples. This trend, from large number of rapid publications to more careful studies, has been seen many times before in many other fields (especially ones with attractive practical applications, e.g. high temperature superconductors).

In the introduction of this chapter (section 2.1), it was put forward that in addition to pure research aims, the study of dilute magnetic semiconductors is in part motivated by the potential application of them in spintronic devices (as the spin polarisation of any charge carriers would be intrinsic). However, since the start of this work, there has been a growing interest in the field of topological insulators. These materials also have the spin polarisation intrinsic to the material, not by ferromagnetic ordering of the charge carriers as in the case of dilute magnetic semiconductors, but by having topologically protected spin states.

Whilst it is beyond the scope of this thesis to discuss topological insulators in detail,

there are interesting parallels to be drawn between the two areas[3]. In contrast to many phenomena in condensed matter, the underlying theory and prediction for both these systems way proceeded their experimental discovery: dilute magnetic semiconductors and topological insulators were theoretically discussed in the 1950's and 1980's, respectively. There also exists a noticeable trend that has made these materials *à la mode*, when following a breakthrough experimental measurement, there is a surge in output as seen in conferences, publications and overall effort.

[3]There are several excellent reviews of topological insulators such as J. Moore, Nature **464** 194-198 (2010) and M. Z. Hasan and C. L. Kane, Rev. Mod. Phys. **82** (2010).

Chapter 3

Inelastic neutron scattering studies in uranium antimonide

We now move from the relatively new and dynamic field of dilute magnetic semiconductors; to the well studied and mature topic of multi-**k** magnetism in uranium antimonide. Despite being well established, there are still similar challenges in measuring and understanding the emergent magnetic properties.

There is also a shift in topic from the study of ferromagnets to multi-**k** magnetic order, where the spins are no longer collinear and there is no net magnetisation. The underlying themes that unite these two topics are in the role of local *vs.* itinerant magnetic interactions, as well as using available experimental techniques to probe and understand the emergent magnetism.

3.1 Introduction

Identifying the magnetic structure is central to studies in magnetism, akin to how crystal structure is key to chemistry [105]. However, clear experimental understanding of a magnetic properties is often obscured by the many effects present within a

system, which make prediction of the emergent properties very difficult. One example is the oldest known magnetic substance, magnetite (Fe_3O_4); which despite having a net magnetisation was thought to be a ferromagnet until work by Néel revealed it to show ferrimagnetism [136]. This ordering was later understood to be due to the double exchange mechanism (discussed in section 1.2).

In the case of antiferromagnets, the magnetisation vanishes on macroscopic length scales, which means determining the configuration of the magnetic order requires a probe sensitive to these length scales. Neutron scattering (discussed in section 3.4) has successfully become a choice method in determining the spin configuration and properties of antiferromagnets [20, 170].

The uranium monopnictides have a simple face-centred cubic structure, but can exhibit widely different magnetic symmetries depending on the composition: from ferromagnetism, to a range of multi-**k** magnetic orders (this is discussed in more detail in the following sections). In particular, it is the multi-**k** magnetic ordering that has provided many surprises: rather than simple antiferromagnetic stacking of spins in a single **k** direction, these systems can exhibit **k**-vectors ordered in multiple directions simultaneously. This configuration was unexpected and only through careful study was their ordering revealed [105].

Key themes in this field that are still being explored are identifying the type of antiferromagnetic order, which has proved experimentally challenging, and also the lack of quantitative understanding of the individual interactions - in particular, the extent of hybridisation that occurs between the uranium's $5f$ electrons with conduction electrons and its role for magnetism is not fully understood [79, 84, 105, 194].

This chapter discusses one of the uranium monopnictides: the 3-**k** antiferromagnet uranium antimonide, which has proved a rich field of study for over thirty years. Whilst the low temperature behaviour has been well characterised by many methods, there still remain puzzles at higher temperatures that give insights into the magnetic order

in this material.

This study uses inelastic neutron scattering with tri-directional polarisation analysis, which is used to learn about the disappearance of the spin waves in the system - a point that, as we shall see, is crucial in understanding the stabilisation of the multi-**k** state in USb.

This chapter will discuss the physics of multi-**k** magnetism and the uranium antimonide system, and show how developing experimental techniques are able to reveal new discoveries in this canonical 3-**k** system.

3.2 Background to multi-k magnetism

The aims of this section are to provide a brief background to multi-**k** magnetism in general, with particular attention on the focus of this chapter: uranium antimonide.

3.2.1 Multi-k magnetism

Any ordered magnetic structure can be described by a general on-site term

$$M_{\mathbf{k}\alpha} = \mathbf{M}_{\mathbf{k}_\alpha} \exp(i\theta_{\mathbf{k}_\alpha}) \tag{3.1}$$

where $\mathbf{M}_{\mathbf{k}_\alpha}$ is the polarisation vector (containing the magnitude and direction of the moment), $\theta_{\mathbf{k}_\alpha} = \mathbf{k}_\alpha.\mathbf{r}_i + \theta_\alpha$ gives the phase of the spin density wave on the i^{th} site and $\mathbf{k}_\alpha$ is the propagation wave vector. Note that the magnetisation and propagation wave vector do not have to be collinear or commensurate - for example, in the case of a helimagnet.

Systems with a single propagation vector are known as single-**k** magnetic structures. This can be extended to define a multi-**k** magnet as a system where there are *multiple* and *equivalent* $\mathbf{k}_\alpha$ components. For localised spins, a magnetically ordered multiple-**k**

system can be thought of as being made up of a superposition of multiple equivalent **k** ordering vectors on each spin site.

In general, there may be competing magnetic orders present (such as spin glass materials), in which case additional frequency components ($\theta_{\mathbf{k}_\alpha}$) may be also introduced. It should be noted that whilst these have different **k** components, they are not referred to as multi-**k** magnets as they are not long range ordered.

The existence of multiple and equivalent propagation vectors makes these systems highly symmetric: these systems must have crystal symmetry high enough to support multiple equivalent **k** components. In fact it remains an open question as to whether, the multi-**k** nature is reflecting the high crystal symmetry or enforcing it. This symmetry, in addition to being theoretically interesting as we shall see, also presents experimental challenges in probing these systems.

Justification for the multi-k state

The existence for multi-**k** magnetic ordering as energetically favourable shall now be presented. We start by considering a face centred cubic (fcc) magnetic structure with localised spins. The observed magnetisation is given by

$$M(\mathbf{r}) = M_{\mathbf{k}_\alpha} + M^*_{\mathbf{k}_\alpha} = \mathbf{M}_{\mathbf{k}_\alpha} e^{i(\mathbf{k}_\alpha.\mathbf{r}+\theta_\alpha)} + \mathbf{M}_{\mathbf{k}_\alpha} e^{-i(\mathbf{k}_\alpha.\mathbf{r}+\theta_\alpha)} \tag{3.2}$$

where $\mathbf{k}_\alpha$ is the propagation vector(s). Due to symmetry, the spin density waves along equivalent directions must have the same energy (otherwise there must be a distortion away from cubic symmetry along a preferred direction so that the **k**-vectors can no longer be equivalent).

We now consider the Landau free-energy expansion, which expresses the free energy of a system in terms of the order parameter. For the magnetic case (in the absence of an external magnetic field), only even terms exist due to symmetry which gives

$$\Phi(T,k) = \Phi_0 + a(T,k)\eta^2 + b(T,k)\eta^4 + ... \tag{3.3}$$

where $\Phi(T,k)$ is the free energy and η is the order parameter. The relevant order parameter is given in Equation 3.1 if we now interpret $M_{\mathbf{k}_\alpha}$ not simply as an on-site term, but over many sites. We are free to do this as the free energy must be translationally invariant under the operation $\mathbf{r}_i \rightarrow \mathbf{r}_i + \mathbf{R}_n$ (where $\mathbf{R}_n$ is a multiple of the lattice vector).

The simplest multi-**k** expression for the free energy expansion (up to second order) is then

$$\Phi - \Phi_0 = \sum_\alpha A(k_\alpha, T)(M_{\mathbf{k}_\alpha}.M^*_{\mathbf{k}_\alpha}) + B_1 \sum_\alpha (M_{\mathbf{k}_\alpha}.M^*_{\mathbf{k}_\alpha})^2 + B_2 \sum_{\alpha \neq \beta} (M_{\mathbf{k}_\alpha}.M^*_{\mathbf{k}_\alpha})(M_{\mathbf{k}_\beta}.M^*_{\mathbf{k}_\beta}) \tag{3.4}$$

where $A(k_\alpha, T)$ depends on both temperature and the magnitude of $\mathbf{k}_\alpha$ and the B_n terms are assumed to be temperature and wave vector independent in this approximation. This expression is still generally valid for the 1-**k** case, which sets the off-diagonal, B_2, terms to zero (as by definition there is only one **k** in a given volume), therefore

$$(\Phi - \Phi_0)_{1k} = A(k_\alpha, T)|\mathbf{M}_{\mathbf{k}_\alpha}|^2 + B_1|\mathbf{M}_{\mathbf{k}_\alpha}|^4 \tag{3.5}$$

Minimising this free energy with respect to $|\mathbf{M}_{\mathbf{k}_\alpha}|^2$ gives $|\mathbf{M}_{\mathbf{k}_\alpha}|^2 = -A(k_x, T)/2B_1$ (where k_x is chosen without the loss of generality). A stable minimum for the free energy can be found by considering the second derivative, which shows that the 1-**k** state is stabilised when $B_1 > 0$.

The assumption here to ignore the temperature dependence of the B parameters is supported by noting $|\mathbf{M}_{\mathbf{k}_\alpha}|^2 \propto A(k_x, T)$. In the simplest approximation the $A(k_x, T)$ term will be linear in temperature (with the form $[T - T_N]$, where T_N is the ordering temperature), so including any temperature dependence to the B parameters now only adds fourth-order terms to the free energy.

To consider the 3-**k** case, we assume three equivalent propagation vectors and hence three equivalent order parameters (needed to preserve the cubic symmetry): $|\mathbf{M}_{\mathbf{k}_x}|^2 = |\mathbf{M}_{\mathbf{k}_y}|^2 = |\mathbf{M}_{\mathbf{k}_z}|^2 = |\mathbf{M}|^2$. Also from symmetry considerations these **k**-vectors must all

be orthogonal to one another and must lie along symmetry directions of the underlying crystal.

From Equation 3.4, the free energy of the 3-**k** state is then

$$(\Phi - \Phi_0)_{3k} = 3A(k_\alpha, T)|\mathbf{M}|^2 + 3B_1|\mathbf{M}|^4 + 3B_2|\mathbf{M}|^4 \tag{3.6}$$

If we assume there is a fixed total amount magnetic moment available in the system, we note that $3|\mathbf{M}_{3k}|^2 = |\mathbf{M}_{1k}|^2$. Therefore, in order for the 3-**k** state to be energetically favourable over the 1-**k** state and by comparison with Equation 3.5, the off-diagonal terms must bring some energy saving (i.e. $B_2 < 0$).

The free energy of the 3-**k** state is minimised when $|\mathbf{M}|^2 = -A(k,T)/2(B_1 + B_2)$ and is a stable energy minimum when $B_1 + B_2 > 0$. Hence, with the previous condition, this means that only when $-B_1 < B_2 < 0$ is the 3-**k** state energetically favourable over the 1-**k** state and stable.

Similar arguments can be made to show that 2-**k** magnetic order is also possible, where higher order terms in the free energy are needed to stabilise it over the 3-**k** case.

These arguments show that by careful selection of the coefficients in the free energy expansion, multi-**k** order is possible, however it says nothing about why a given system should choose these values.

Magnetic 3-k order on the fcc lattice

The 3-**k** state is defined as a state made up of three equivalent propagation vectors. In principle, this can exist in many different topologies and have different forms. If we consider the fcc lattice (important in many 3-**k** materials, and in particular for USb studied in this thesis), then the 3-**k** state may be made up of 3 equivalent **k**-vectors of the form $\langle 0\ 0\ 1 \rangle$. These 3-**k** components can be summed to give the resultant magnetisation which points along $\langle 1\ 1\ 1 \rangle$-type directions for each spin.

An illustration of a lattice populated with $\langle 0\ 0\ 1 \rangle$-type ordering of spins (pointing

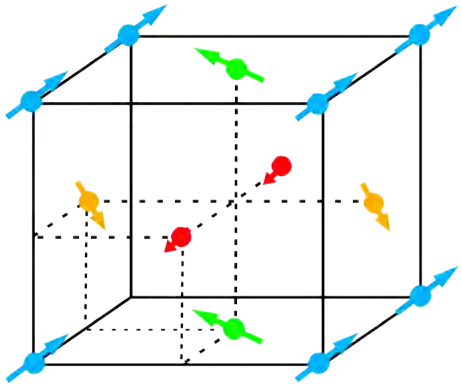

Figure 3.1: Spins on an fcc lattice pointing along ⟨1 1 1⟩ directions made up of ⟨0 0 1⟩-type propagation vectors making up a longitudinal 3-**k** structure. The different colours denote the four different lattice points of the fcc basis.

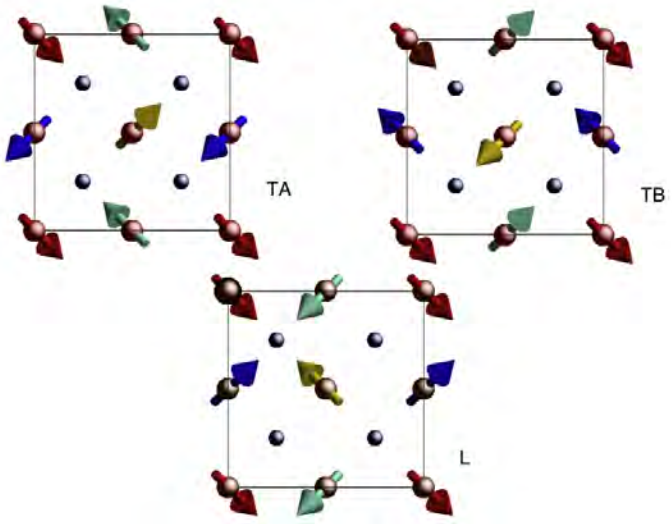

Figure 3.2: 2D spin projections of the two possible 3-**k** structures on an fcc lattice with ⟨0 0 1⟩-type propagation vectors (from reference [126]). There is one longitudinal configuration (the same as Fig. 3.1) denoted by L, which has propagation vector parallel to the polarisation. The two possible degenerate transverse domains labelled, TA and TB, have propagation vector perpendicular to the magnetisation.

along $\langle 1\ 1\ 1 \rangle$ directions) is shown in figure 3.1. In this case, the coupling of spins gives the magnetic polarisation, $\mathbf{M}_{\mathbf{k}\alpha}$, which is parallel to the propagation vector, $\mathbf{k}_\alpha$, and is therefore known as a *longitudinal* 3-**k** structure. It is also possible for the magnetic polarisation to be perpendicular to the propagation vector in which case this is known as a *transverse* structure. Longitudinal and transverse structures are shown in figure 3.2, with the actual observed order depending on the material in question.

Measurements of multi-k magnets

Neutron diffraction is often the choice probe to resolve magnetic order. The neutron's magnetic moment makes it an ideal microscopic probe to detect a periodic spin structure and, as they are deeply penetrating, they are useful for studying the bulk behaviour (rather than being limited to the sample surface). By studying the Bragg reflections from the system; the direction, periodicity and magnitude of the ordered moments can be deduced.

However, whilst neutron scattering intrinsically operates on a microscopic scale (by interference of scattered neutron amplitudes within a coherence volume [14, 47]), the measured quantity (the square of the amplitudes) is a sum over the whole sample - thus there is no way to differentiate between a mixed phase and phase separated regions. This presents a problem for the high symmetry case of the multi-**k** magnets where there is a superposition of ordered **k** vectors on each site: there is no way of distinguishing the 3-**k** state from three equally populated phases of 1-**k** magnets.

To study these high symmetry systems using neutron diffraction outlined above, it is clear something is needed to *crack* the symmetry: this can be done by either studying the excitations of these systems away from their equilibrium positions (i.e. a study of spin waves, which is detailed in Section 3.2.3) or by polarising the neutron spin to isolate different components of the magnetisation (detailed in Section 3.4 and is the main theme of this chapter).

Another approach could be to impose some external action to break this symmetry; for example uni-axial pressure, which could in the case of a 1-**k** magnet, preferentially populate a single domain only (and hence confirm this is a 1-**k** rather than 3-**k** magnet). Whilst this was an important step historically in providing evidence for multi-**k** magnetism [155], this method and others like it should be treated with caution. Apart from the question of how much pressure to apply to cause this change, this forcibly attempts to destroys the symmetry of the 3-**k** state that we want to study.

In addition to neutron scattering, the usual toolbox of bulk probes are important to identify phase transitions in these materials; such as magnetisation, specific heat, resistivity and lattice parameters measurements.

3.2.2 Magnetic order in the uranium monopnictides

In the periodic table, uranium lies in the actinide series and, in general, shares many of the properties (both chemical and physical) that make actinide compounds interesting. The electronic configuration of the actinides is made up of a radon-like core, with the remaining electrons filling the $7s$, $6d$ and $5f$ shells. In particular, for the lighter elements in the actinide series (of which uranium is included), the $5f$ electrons are partially extended. If there is overlap between shells of neighbouring atoms, this can lead to the formation of a $5f$ band and metallic behaviour. Hybridisation of this band can then occur with the $6d$ and $7s$ bands, which are nearby in energy, resulting in a complicated band structure. In addition, the large amount of angular momentum associated with the $5f$ electrons (and indeed to some extent the $6d$) can lead to spin-orbit interactions altering this energy landscape further.

In general, the local environment of the actinide ion plays a very important role in the expression of these effects (for example insulating *vs.* metallic behaviour) and understanding the resulting properties.

The uranium monopnictides, UX (where X is N, P, As, Sb, Bi) all crystallise into

face centred cubic rock-salt structures (part of the $Fm\bar{3}m$ space group) and may be thought of as two inter-penetrating fcc lattices, with uranium and the pnictide atoms on each sub-lattice, respectively. They all magnetically order and display a range of magnetic structures (see table 3.1).

	a (Å)	T_N (K)	k	Ordering	Easy axis
UN	4.890	53	$\langle 0\ 0\ 1 \rangle$	$1k$ type I	$\langle 0\ 0\ 1 \rangle$
UP	5.589	122	$\langle 0\ 0\ 1 \rangle$	$1k$ type I	$\langle 0\ 0\ 1 \rangle$
		22	$\langle 0\ 0\ 1 \rangle$	$2k$ type I	$\langle 0\ 1\ 1 \rangle$
UAs	5.779	124	$\langle 0\ 0\ 1 \rangle$	$1k$ type I	$\langle 0\ 0\ 1 \rangle$
		62	$\langle 0\ 0\ \frac{1}{2} \rangle$	$2k$ type IA	$\langle 0\ 1\ 1 \rangle$
USb	6.191	213	$\langle 0\ 0\ 1 \rangle$	$3k$ type I	$\langle 1\ 1\ 1 \rangle$
UBi	6.364	285	$\langle 0\ 0\ 1 \rangle$	type I	?

Table 3.1: A table showing the magnetic properties of the uranium monopnictide series (from reference [105]).

The ordering in these compounds was found to be longitudinal, due to the absence of the (0 0 1) magnetic Bragg reflections from powdered neutron measurements, meaning the moments must be parallel to the propagation direction (this is discussed more in section 3.4.1). From this information, it was initially supposed that these materials had a single longitudinal wavevector; later experimental evidence was able to show this not to be the case.

Experiments on mixed uranium pnictide-chalcogenide systems, such as $UP_{1-x}S_x$ [101, 106] and $UAs_{1-x}S_x$ [116, 108], were able to show a continuous transition between $k = 1$ antiferromagnetism, through incommensurate ordering, right up to $k = 0$ ordering in US (ferromagnetism). Here it was put forward that it was the conduction

electrons that were important through a RKKY-like coupling [64].

Whilst there are some similarities between compounds in the pnictide series, such as the gradual increase of the Néel temperature, there are also clear differences such as the absence of a low temperature transition in USb and UBi. With the magnetism mostly associated with large $5f$ spins, these differences highlight a possible electronic influence and dependence on local environment from the pnictide species.

3.2.3 Multi-k magnetism in USb

This section introduces the properties of uranium antimonide; with particular attention to the magnetic order, how this was realised experimentally through study of the magnetic excitations and then the evolution of these excitations at higher temperatures.

USb: a physical overview

USb is an insulator (the room temperature resistivity is approximately $600\mu\Omega$cm [140]) and so it appears that the uranium $5f$ electrons are largely localised. The temperature dependence of the resistivity is shown in Fig. 3.3 and shows several interesting features;

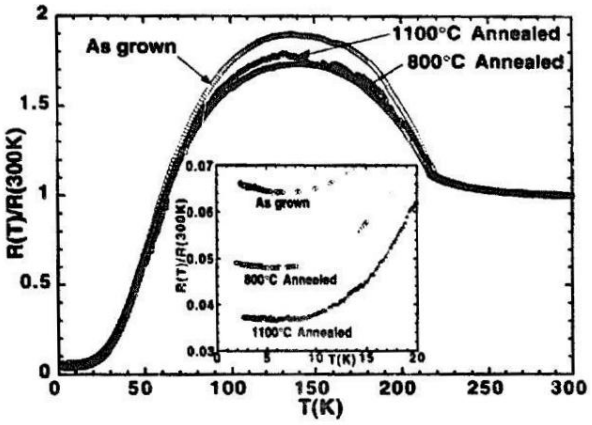

Figure 3.3: The temperature dependence of resistivity in USb from reference [140]. The different curves are due to different annealing conditions.

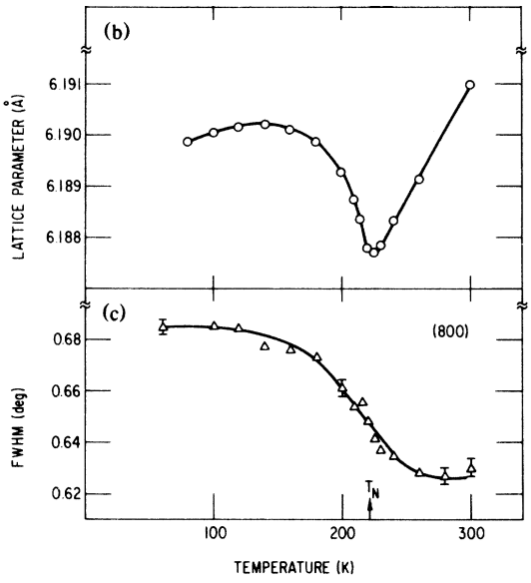

Figure 3.4: The temperature dependence of lattice parameter magnitude (top panel) and FWHM of the $\mathbf{Q} = (1, 1, 0)$ reflection (lower panel) in USb from reference [87].

for example, a change in gradient around 210 K due to magnetic ordering.

The temperatures where these features occur are also mirrored in lattice parameter measurements (Fig. 3.4) [87]. However, the dependencies of these measurements are not fully understood, but will be referred to later in section 3.6.1.

Specific heat measurements were able to identify a phase transition around 210 K, with no further transitions below this temperature (Fig. 3.5) [140].

Early neutron scattering measurements on USb were able to identify the emergence of magnetic order ($T_N \approx 215\ K$)[102, 115]. Measurements showed that there were Bragg reflections from the $\mathbf{Q} = [1\ 1\ 0]$, but not from the $[0\ 0\ 1]$ reflection, corresponding to a purely longitudinal moment. This is because an ordered magnetic moments along the $\pm(0, 0, 1)$ direction cannot not give rise to a Bragg reflection at $\mathbf{Q} = [0\ 0\ 1]$ as the neutron is sensitive to ordered moments perpendicular to the scattering vector (this is discussed in more detail in Sec. 3.4.1). Therefore, it was initially supposed that the ordering was made of $+\ -\ +\ -$ planes with the moments parallel to the $[0\ 0\ 1]$

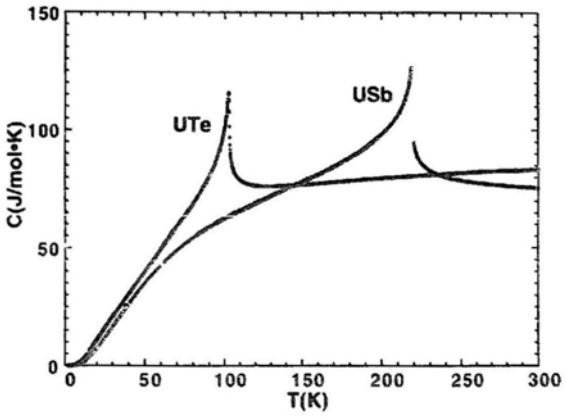

Figure 3.5: The specific heat capacity of USb (and UTe) from reference [140].

directions (type-I antiferromagnetism) [111, 112, 115]. However as discussed in Section 3.2.1, these types of measurements represent ensemble averages and are not sensitive in resolving three equally populated and spatially separated 1-**k** domains from real 3-**k** ordering.

In the next section we will see that the 1-**k** type-I AFM order proposed above, is not the case for USb. There were two important hints against this simple picture. One was the observation in USb, and also related actinide monopnictides, of the preservation of cubic symmetry in antiferromagnetic compounds below T_N (but not ferromagnetic ones) [87, 107] which is puzzling for single-**k** magnetism - the structural symmetry must be lowered when lowering the magnetic symmetry.

Furthermore, careful measurement of the elastic neutron cross section and calculation, in addition to bulk magnetisation measurements, showed that the crystal-field ground state selects the $\langle 1\ 1\ 1 \rangle$ as the magnetic easy axis, raising questions as to how this could result in ordered moments along the $\langle 0\ 0\ 1 \rangle$ directions as seen by neutron diffraction [109, 105].

Spin excitations in USb

Understanding the spin excitations in USb was key in realising the magnetic order in this system. The results for the spin wave dispersion are shown in Figure 3.6 and were obtained by inelastic neutron scattering [79, 112].

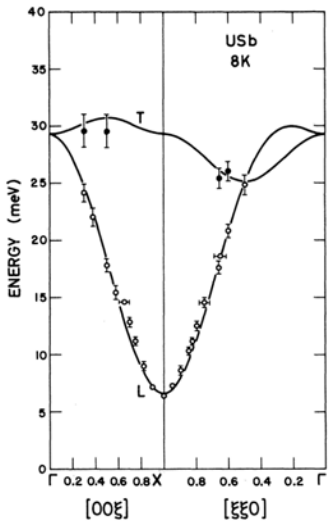

Figure 3.6: The spin wave dispersion in USb at low temperatures (from reference [79]). The solid points were experimentally obtained from reference [112] and the solid lines are calculated based on 3-**k** longitudinal magnetic order.

The lower of the two modes was identified as being longitudinally polarised (i.e. parallel to the magnetic propagation vector), with the upper mode transversely polarised. This result is surprising as one normally expects the low energy spin waves to have excitations transverse to their polarisation: this semi-classical understanding is illustrated in Figure 3.7a, which show the precession of spins to always be transverse to the magnetisation propagation vector.

However, now consider the 3-**k** structure, which is made of equivalent wave vectors of the form [0 0 1] that add to give spins (residing on the uranium sites) pointing along local ⟨1 1 1⟩-type directions. Within each (0 0 1) plane, the fluctuations of the spins from the equilibrium positions have transverse and longitudinal components with

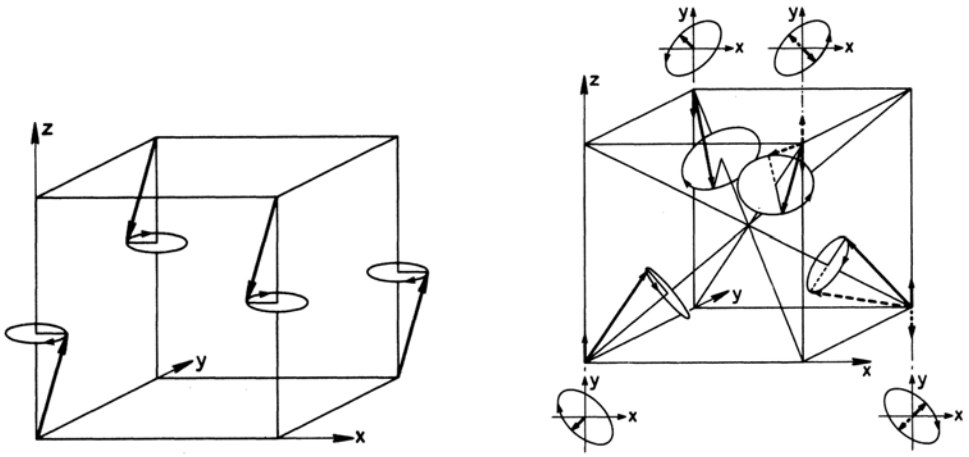

(a) Low energy excitations in a type-I AFM are purely transverse relative to the propagation vector.

(b) A cartoon showing spin excitations of the 3-**k** state.

Figure 3.7: Cartoons of spin excitations of 1-**k** and 3-**k** structures (from reference [79]).

respect to the wave vector of the propagating excitation (as shown in Figure 3.7b).

By direct analogy with phonons, the resultant spin waves can either arise from coupling spins in-phase or in antiphase with one another, giving acoustic and optical magnons, respectively. Without a loss of generality, we can consider modes relative to $\mathbf{k} = [0\ 0\ 1]$ (i.e. in the z-direction) and also perpendicular to this (i.e. in the xy plane).

Looking first at the acoustic mode (the solid lines in Fig. 3.7b), one finds the in-plane components of the $xy-$plane cancel, whilst the precession of the longitudinal components along **k** occurs in-phase: hence the low energy acoustic mode appears to be longitudinally polarized.

For the higher energy optical mode, the opposite situation occurs (this is shown by the dashed lines in Figure 3.7b) and the mode appears as a transverse one.

The spin wave dispersion (solid lines in Fig. 3.6) was calculated based on a 3-**k** configuration of localised uranium spins, originally carried out by Jensen and Bak [79]. The Hamiltonian of this model (Eqn. 3.7) has three terms: a nearest neighbour

Heisenberg exchange (H_{Iso}), an anisotropic pseudo-dipolar interaction ($H_{Dipolar}$) and a crystal field term (H_{CF}).

$$
\begin{aligned}
H &= H_{Iso} + H_{Dipolar} + H_{CF} \qquad (3.7)\\
H_{Iso} &= -\sum_{nm} J_{Iso}\, \mathbf{S}_i.\mathbf{S}_j \\
H_{Dipolar} &= -\sum_{nm} J_D \left(\mathbf{S}_i.\hat{r}_{ij}\right)\left(\mathbf{S}_j.\hat{r}_{ij}\right) \\
H_{CF} &= B_4^0 \left(O_4^0 + 5O_4^4\right)
\end{aligned}
$$

The O_m^n terms are the fourth order Stevens operators and are chosen to give cubic symmetry to represent the crystal field environment [76]. $S = \frac{9}{2}$ (or $S = 4$) corresponding to the $5f^3$ (or $5f^2$) configuration were considered for USb. It was found that the bilinear terms give the same ground state configuration for the 1-**k** and 3-**k** states and that it is the crystal field term in the Hamiltonian that is responsible for stabilising the structure and selecting the [1 1 1] easy axis.

The spin wave calculation was based around the standard Holstein-Primakoff transformation, using experimentally estimated values for the exchange constants where available.

These results were key in crucially establishing USb as a multi-**k** structure over a multi domain single-**k** magnet [105].

More recently, inelastic neutron scattering experiments with tri-directional polarization analysis have been able to unambiguously confirm the 3-**k** nature in some materials [16, 126]. By judicious choice of neutron polarisation directions relative to the scattering vector and the underlying crystal axes, the scattered intensity is generated by different components of the magnetization fluctuation operator and allows insight into spin-wave excitations in these high symmetry, complex magnetic structures [22].

In a previous study of USb using knowledge of the expected spin wave polarisations

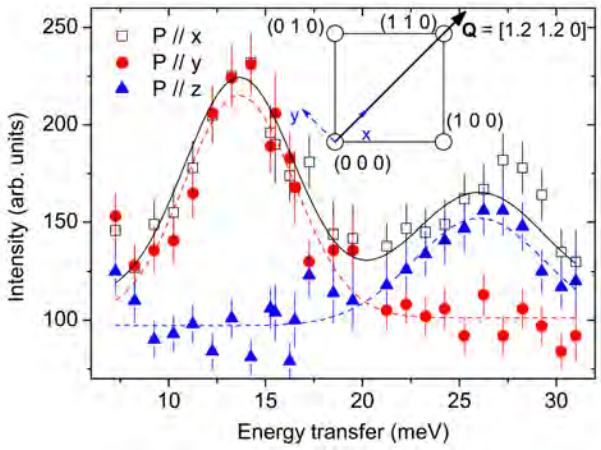

Figure 3.8: Typical inelastic polarised neutron spectra from USb at low temperatures (50 K), along the x, y and z neutron polarization axes (from reference [126]). The y and z neutron polarisation channels are able to pick out the acoustic and optical modes, respectively. The total magnetic signal is measured in the x polarisation channel. Inset: a schematic of the sample-polarization scattering geometry.

described above, the authors were able to pick the neutron polarisations such that the spin waves only appeared in the corresponding neutron polarisation channels [126]. The results from this are shown in Fig. 3.8 which shows the lower acoustic mode in the y-channel and the higher energy optical mode in the z-channel (the x-channel is sensitive to the total detectable magnetic component). This polarised neutron technique is key to this chapter and will be discussed in more detail in Section 3.5.1.

USb spin excitations: getting warmer

At low temperatures, USb is understood as a well-localized 3-**k** antiferromagnet, with clearly defined spin waves that are characteristic of the 3-**k** state.

Above a temperature $T^* \approx 160$ K inside the AFM phase, previous studies have shown evidence of changes in the physical properties. For example, the lattice parameter (Fig. 3.4) [87] and resistivity (Fig. 3.3) [140] reach a maximum at this temperature.

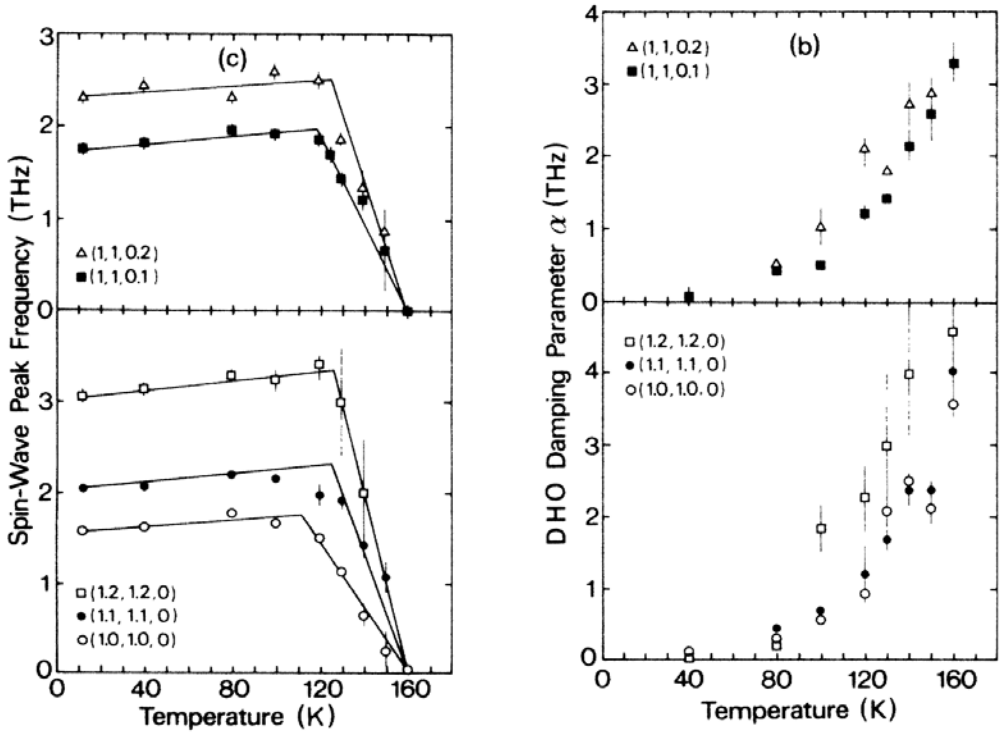

Figure 3.9: Temperature dependence of the spin wave parameters as a function of temperature [66]. The points come from fitting to the measured inelastic spectra and the solid lines are guides to the eye only. Left: spin wave peak frequency *vs.* temperature showing the collapse of the characteristic spin waves of the 3-**k** state at T^*. Right: the damping of the spin waves *vs.* temperature, which shows the spin waves becoming heavily damped approaching T^*.

More notable are the inelastic neutron scattering measurements looking at the spin waves that are also sensitive to this change.

The results for the spin wave peak frequency, shown in left panel of Fig. 3.9, show a small initial increase in the spin wave peak frequency at low temperatures, followed by a steep drop at T^* across a range of different scattering vectors, which represents the collapse of the acoustic mode, as the excitations go from gapped to continuous. By analysis of the width of the spin wave feature, the damping can be obtained, which was found to increase approaching T^* and is shown in right panel of Fig. 3.9.

Often the collapse of a spin wave mode to zero energy is an indicator that a system is unstable against fluctuations and an associated magnetic phase transition is nearby - a feature seen in many materials [29, 95, 163, 175, 181]. It is therefore puzzling that there is no structural or magnetic phase transition associated with this mode softening and collapse at T^*. No changes have been reported in the magnetic order from neutron scattering experiments (including this work) and specific heat shows no evidence for a transition [66, 115, 140]. The cubic symmetry of the 3-**k** state is also preserved at all temperatures [87].

Muon spin rotation (μSR) measurements find a distinct change in the relaxation rate at T^* [8, 97]. Here, it was suggested that this change-over and collapse of the spin waves is due to de-phasing of the individual Fourier components making up the 3-**k** phase [8, 110]. Many other multi-**k** systems show changes in the number of Fourier components locked in as a function of temperature, often in a non-intuitive fashion [100, 121]. It is the de-phasing hypothesis at T^* in USb that is the subject of this thesis chapter.

3.3 Motivation & aims

It had been suggested that the change-over and collapse of the spin waves at T^* is due to phase de-locking of the individual Fourier components making up the 3-**k** state [8, 110]. However, clear observation of this de-phasing has remained elusive: μSR studies are difficult to interpret and lack spatial information [8, 97], whilst straightforward neutron scattering experiments probe the total projection of the magnetisation onto the scattering plane and so are unable to resolve changes to a specific mode, which has a particular direction of propagation.

Only a few UX compounds have well defined spin waves. This has been explained as being due to an interaction between the localized magnetic $5f$ electrons and the

$6d$ conduction electrons, leading to a strong damping of the spin waves [67]. In this picture the presence of spin waves in USb is assigned to its localised moments and lower 'metallicity'; there is little overlap between the f and d electrons. In this case, the change in the spin waves at higher temperatures could be due to an increased $f-d$ coupling. There is no obvious reason for this to effect the 3-**k** structure, and so if this is the only factor in play, the spin wave polarisation should remain unchanged. Interestingly, this model of almost localised $5f$ electrons has been challenged by the interpretation of recent photo-emission experiments on USb [99].

The aim of this work is to use polarised neutrons to measure the inelastic spectrum from below T^*, where there are well defined spin waves, to above T_N, where there is only quasielastic scattering. By monitoring the change with temperature of the different neutron polarisation channels, and hence polarization of magnetic fluctuations that are particular to the 3-**k** structure [16, 126], this gives a clear way to test whether the de-phasing occurs or whether the physics at T^* arises from a change in the itinerancy. If the 3-**k** structure de-phases, then the polarisation differences should disappear above T^*. If the 3-**k** structure remains fixed up to the Néel temperature, the polarisation differences will be maintained as the spin waves broaden and disappear.

3.4 Methods

The principles behind inelastic neutron scattering will be presented, with an emphasis on the neutron polarisation in the context of inelastic polarised neutron scattering with tri-directional polarisation analysis which is heavily used in this work,

3.4.1 Neutron scattering theory

The neutron has a magnetic moment so it can scatter from both nuclear and electron spins, whilst also interacting with nuclei via the strong force. The spatial periodic-

ity found in magnetic materials means that, similar to the use of X-rays for probing structural properties (Sec. 2.4.2); neutron diffraction from ordered electron spins is an invaluable tool in probing these correlations.

Thermal neutrons (i.e. having kinetic energies corresponding to temperatures of $\sim$ 300 K) have wavelengths similar to inter-atomic spacings and also energies on the order of 10 meV, so are well matched to probe the relevant length and energy scales found in many condensed matter systems. Neutrons have a high penetration depth (in part due to them being uncharged) and so are ideally suited to probe bulk behaviour: a useful regime to work in theoretically, as surface effects can be safely neglected.

In a neutron scattering experiment, the measured quantity is the *partial differential cross section* ($\frac{d^2\sigma}{d\omega d\Omega}$) which gives the number of scattered particles into a given solid angle ($d\Omega$) and energy range ($d\omega$). This quantity depends on the interaction between the neutrons and the structure & composition of the material. Neutrons scatter weakly from nuclei and magnetic fields so can be treated using first order perturbation theory. A justification for the cross section will now be put forward, following the approaches in texts by Lovesey and Squires [122, 180]

It is first useful to consider the *differential cross section* ($\frac{d\sigma}{d\Omega}$) by integrating the partial differential cross section across all energies, which simply gives the number of particles scattered into a solid angle. We will now switch to a more microscopic viewpoint by considering the neutron changing from state $k \rightarrow k'$ and the sample transitioning from a state $\lambda \rightarrow \lambda'$. The differential scattering cross section is given by:

$$\left(\frac{d\sigma}{d\Omega}\right)_{\lambda\rightarrow\lambda'} = \frac{1}{\Phi}\frac{1}{d\Omega}\sum_{\mathbf{k}'} W_{\mathbf{k},\lambda\rightarrow\mathbf{k}',\lambda'} \tag{3.8}$$

where Φ is the incident neutron flux and $W_{k,\lambda\rightarrow k',\lambda'}$ is the transition ratio from state k, λ to k', λ'. One may recognise the right hand side of equation 3.8 as a standard and important result in quantum mechanics which is given by *Fermi's golden rule*: this states that the transition rate between states is proportional to the final neutron

density of states and the square of matrix element betweens initial and final states (subject to the conservation of energy), and is expressed as:

$$\sum_{\mathbf{k}'} W_{\mathbf{k},\lambda\to\mathbf{k}',\lambda'} = \frac{2\pi}{\hbar}\rho_{\mathbf{k}'}|\langle\mathbf{k}'\lambda'|\hat{V}|\mathbf{k}\lambda\rangle|^2 \tag{3.9}$$

where $\rho_{\mathbf{k}'}$ is the final momentum density of states for the neutron per unit energy range and $\hat{V}$ is the potential operator for the system that describes the interaction between the neutron and the sample.

By adopting a standard box normalisation approach, where the neutron and sample system exist in a box of large but finite volume, Y, the density of momentum states, $\rho_{\mathbf{k}'}$, may be evaluated. By imposing this boundary condition, only a discrete set of wave vectors are allowed (i.e. neutron states that are periodic in the volume of the box), which form a lattice in $\mathbf{k}$-space. with volume

$$v_k = \frac{(2\pi)^3}{Y} \tag{3.10}$$

For a neutron with mass, m, the final neutron energy is

$$E' = \frac{\hbar^2}{2m}k'^2 \tag{3.11}$$

and hence

$$dE' = \frac{\hbar^2}{m}k'dk' \tag{3.12}$$

We note that $\rho_{\mathbf{k}'}dE'$ is, by definition, the number of states in $d\Omega$ with energy between $E' \to E' + dE'$, which is equal to the number of wavevector points in an element of volume $k'^2dk'd\Omega$ and therefore

$$\rho_{\mathbf{k}'}dE' = \frac{1}{v_k}k'^2dk'd\Omega \tag{3.13}$$

hence from Eqn. 3.10 and 3.12

$$\rho_{\mathbf{k}'} = \frac{Y}{(2\pi^3)}k'\frac{m}{\hbar^2}d\Omega \tag{3.14}$$

The result should not depend on our choice of box size and so we may begin to evaluate the matrix element from Eqn. 3.9 by considering plane waves and a single neutron in the box volume, Y. In this scheme, the matrix element in Eqn. 3.9 must be normalised by $\frac{1}{Y^2}$. The incident neutron flux in Eqn. 3.8 is the product of the neutron density and velocity, so

$$\Phi = \frac{1}{Y}\frac{\hbar k}{m} \tag{3.15}$$

We may now use these results from Eqn. 3.14 and 3.15 with the original definition of the differential cross section (Eqn. 3.8) to find that this cross section is independent of the choice in box size and is given by

$$\left(\frac{d\sigma}{d\Omega}\right)_{\lambda\to\lambda'} = \frac{k'}{k}\left(\frac{m}{2\pi\hbar^2}\right)^2 |\langle \mathbf{k}'\lambda'|\hat{V}|\mathbf{k}\lambda\rangle|^2 \delta(\hbar\omega + E_\lambda - E_{\lambda'}) \tag{3.16}$$

where the conservation of energy is explicitly included using a δ-function. This labels the neutron energies by E_λ and $E_{\lambda'}$ for initial and final neutron energies, respectively; and introduces the *energy transfer*, $\hbar\omega$, as the difference in energy between initial and final sample states (i.e. $\hbar\omega = E - E'$).

This constraint on the conservation of energy, allows us to move between the differential cross section (where we integrate over all neutron and sample energy states) and the partial differential cross section and write

$$\frac{d\sigma}{d\Omega} = \int_0^\infty \frac{d^2\sigma}{d\Omega dE'} dE' \tag{3.17}$$

and hence

$$\frac{d^2\sigma}{d\Omega d\omega} = \frac{k'}{k}\left(\frac{m}{2\pi\hbar^2}\right)^2 |\langle \mathbf{k}'\lambda'|\hat{V}|\mathbf{k}\lambda\rangle|^2 \delta(\hbar\omega + E_\lambda - E_{\lambda'}) \tag{3.18}$$

In this expression, we have captured all the sample physics in the matrix element squared term. It is worth noting that in addition to the allowed quantum mechanical states, the observed scattering will also depend on a weighting factor based on the population of these states, p_λ (this is defined such that $\sum_\lambda p_\lambda = 1$). In general, this weight will depend on a thermodynamic factor and the degeneracy of the states.

The motivation for splitting the perturbative term into a weighting factor and matrix element terms is that in a real scattering experiment, the focus is on the matrix elements term (which contains information about the sample states e.g. spin waves, phonons etc.) and the weighting factor gives the appropriate scaling to resolve this. This idea is later used in isolating the interesting spin wave component and the associated Bose population factor in section 3.6.

Spin dependent neutron scattering

The neutron can be defined by two parameters: a wave vector, $\mathbf{k}$, that gives the direction of neutron and wavelength, and orientation of the neutron magnetic moment σ (where σ are the Pauli matrices relative to some quantisation axis).

In an experiment, the individual spin of each neutron is not measured and instead it is often useful to focus on the polarisation, $\mathbf{P}$, which is the average neutron spin. This is defined such that $\mathbf{P} = +1$ for a fully polarised spin up beam (relative to a quantisation axis), -1 for spin-down and 0 for an unpolarized beam. An expedient way in which to describe partial polarisation uses a density matrix of the form

$$\hat{\rho} = \frac{1}{2}(\mathcal{I} + \mathbf{P} \cdot \sigma) \tag{3.19}$$

where $\hat{\rho}$ is the quantum mechanical density matrix operator that describes the neutron beam and $\mathcal{I}$ is the identity matrix.

Recall that the partial differential cross section and hence the measured intensity is proportional to the matrix elements squared (Eqn. 3.18). If we explicitly include the occupational probability, p_σ, and considering only the neutron spin states; the partial differential cross section is proportional to

$$\sum_{\sigma,\sigma'} p_\sigma |\langle \sigma' | \hat{V} | \sigma \rangle|^2 = \sum_{\sigma,\sigma'} p_\sigma \langle \sigma | \hat{V}^+ | \sigma' \rangle \langle \sigma' | \hat{V} | \sigma \rangle \tag{3.20}$$

$$= \sum_{\sigma} p_\sigma \langle \sigma | \hat{V}^+ \hat{V} | \sigma \rangle \tag{3.21}$$

where the closure relationship has been used which assumes there are no phase correlations between neutron spin states, so assumes that the density matrix is diagonal with respect to these states. Continuing this reasoning, the occupational probability is given by the diagonal elements $p_\sigma = \langle\sigma|\hat{\rho}|\sigma\rangle$, and so

$$\sum_\sigma p_\sigma \langle\sigma|\hat{V}^+\hat{V}|\sigma\rangle = \sum_\sigma \langle\sigma|\hat{\rho}|\sigma\rangle\langle\sigma|\hat{V}^+\hat{V}|\sigma\rangle \quad (3.22)$$

$$= \sum_\sigma \langle\sigma|\hat{\rho}\hat{V}^+\hat{V}|\sigma\rangle \quad (3.23)$$

$$= \mathrm{Tr}\left(\hat{\rho}\hat{V}^+\hat{V}\right) \quad (3.24)$$

Note that the trace is independent of choosing $\hat{\rho}$ to be diagonal and so is generally valid [122].

Now without justification, we will construct the following scattering potential, $\hat{V}$, for the neutrons and later show its validity for both nuclear and magnetic scattering processes.

$$\hat{V} = \hat{A} + \hat{\mathbf{B}} \cdot \sigma \quad (3.25)$$

Here $\hat{A}$ and $\hat{\mathbf{B}}$ refer to operators for the sample.

Using this expression for the potential and the definition for the density matrix (equation 3.19), we are able to write the spin dependent cross section as being proportional to

$$\mathrm{Tr}\left(\hat{\rho}\hat{V}^+\hat{V}\right) = \mathrm{Tr}\left[(\mathcal{I} + \mathbf{P}\cdot\sigma)(\hat{A}^+ + \hat{\mathbf{B}}^+\cdot\sigma^*)(\hat{A} + \hat{\mathbf{B}}\cdot\sigma)\right] \quad (3.26)$$

$$= \hat{A}^+\hat{A} + \hat{\mathbf{B}}^+\hat{\mathbf{B}} + \hat{A}^+(\hat{\mathbf{B}}\cdot\mathbf{P}) + (\hat{\mathbf{B}}^+\cdot\mathbf{P})\hat{A} + i\mathbf{P}\cdot(\hat{\mathbf{B}}^+\times\hat{\mathbf{B}}) \quad (3.27)$$

where the properties of the Pauli matrices have been used to obtain this result. As we expect scattering from the nucleus to be polarisation independent (nuclear spins are orientated randomly except at very low temperatures), we will find the $\hat{A}$-only terms are from nuclear scattering and associate the $\hat{\mathbf{B}}$-only terms mostly with magnetic scattering. The mixed cross-terms arise from interference from nuclear and magnetic

scattering and can be used to extract values for the magnetic structure factor (and hence magnetic moments) in absolute units. This is discussed in more detail in section 3.4.1.

In order to perform a polarisation analysis experiment, it is also important to know the final polarisation of the scattered neutrons, $\mathbf{P'}$. The final polarisation is due to the interaction of the neutron spin with the sample and is made up of sampling the initial neutron spin with all possible scattering processes. This is given by the density matrix $\hat{\rho}' = \hat{\rho}\hat{V}^{+}\hat{V}$ and combining this with the definition of the beam polarisation [namely that $\mathbf{P'} = \mathrm{Tr}(\sigma\hat{\rho}')$ which follows from Eqn. 3.19], we find:

$$\mathbf{P'} \propto \mathrm{Tr}(\hat{\rho}\hat{V}^{+}\sigma\hat{V}) \tag{3.28}$$

where the cyclic properties of the trace operation have been used and the appropriate constant of proportionality is the normalisation by $\mathrm{Tr}(\hat{\rho}')$.

The measured polarisation dependent partial differential cross section is proportional to the quantity, $\mathbf{P'}$, so it is therefore important to evaluate $\mathrm{Tr}(\hat{\rho}\hat{V}^{+}\sigma\hat{V})$, which we are able to express in terms of the sample operators $\hat{A}$ and $\hat{\mathbf{B}}$ as:

$$\begin{aligned}\mathrm{Tr}(\hat{\rho}\hat{V}^{+}\sigma\hat{V}) \;=\; & \hat{A}^{+}\hat{\mathbf{B}} + \hat{\mathbf{B}}^{+}\hat{A} + \hat{A}^{+}\hat{A}\mathbf{P} \\ & + \hat{\mathbf{B}}^{+}(\hat{\mathbf{B}}\cdot\mathbf{P}) + (\hat{\mathbf{B}}^{+}\cdot\mathbf{P})\hat{\mathbf{B}} - \mathbf{P}(\hat{\mathbf{B}}^{+}\cdot\hat{\mathbf{B}}) \\ & - i(\hat{\mathbf{B}}^{+}\times\hat{\mathbf{B}}) + i\hat{A}(\hat{\mathbf{B}}\times\mathbf{P}) + i(\mathbf{P}\times\hat{\mathbf{B}}^{+})\hat{A}\end{aligned} \tag{3.29}$$

We will revisit this expression in the context of nuclear and magnetic scattering but to highlight some features of this result, we find that an unpolarized beam is polarized by the $\hat{A}^{+}\hat{\mathbf{B}}$, $\hat{A}\hat{\mathbf{B}}^{+}$ and $-i(\mathbf{B}^{+}\hat{}\times\hat{\mathbf{B}})$ terms, which is useful in the creation of polarised neutron beams (see section 3.4.2).

Nuclear scattering

Nuclear scattering, between a neutron and nucleus, can be effectively described by short-range isotropic s-wave scattering (as the range of the strong force is much smaller

than the neutron wavelength)[1]. From this, the Fermi pseudo-potential for a nuclei at position, $\mathbf{R}_l$, is then defined as:

$$\hat{V}(\mathbf{r}) = \frac{2\pi\hbar^2}{m}\sum_l b_l \delta(\mathbf{r} - \mathbf{R}_l) \tag{3.30}$$

where the subscript l denotes that each different site may have a different element and isotope which will have a different scattering length, b.

We may substitute this pseudo-potential into the expression for the differential cross section and need to evaluate:

$$\begin{aligned} \langle k'|\,\hat{V}\,|k\rangle &= \sum_l \hat{b}_l \int d\mathbf{r}\exp(-i\mathbf{k}'\cdot\mathbf{r})\delta(\mathbf{r}-\mathbf{R}_l)\exp(i\mathbf{k}\cdot\mathbf{r}) &(3.31)\\ &= \sum_l \hat{b}_l \exp(i\mathbf{Q}\cdot\mathbf{R}_l) &(3.32)\end{aligned}$$

where the momentum transfer vector, $\mathbf{Q}$, is defined as $\mathbf{Q} = \mathbf{k}' - \mathbf{k}$ and we have introduced a general scattering length operator, $\hat{b}$, which is useful for dealing with the spin dependence of neutron-nuclear scattering. For a single nucleus this is defined as $\hat{b} = \alpha + \frac{1}{2}\beta\boldsymbol{\sigma}\cdot\hat{\mathbf{I}}$, where $\mathbf{I}$ is the nuclear spin operator.

The coefficients α and β may be determined from the eigenvalues of $\hat{b}$ on the two possible spin states for the composite neutron-nucleus system. These two states, $\left|I+\frac{1}{2}\right\rangle$ and $\left|I-\frac{1}{2}\right\rangle$ give eigenvalues of b_+ and b_-, respectively; and after some manipulation:

$$\begin{aligned} \alpha &= \frac{(I+1)b_+ + Ib_-}{2I+1} &(3.33)\\ \beta &= \frac{2(b_+ - b_-)}{2I+1} &(3.34)\end{aligned}$$

Comparing these expressions to the general potential given in Eqn. 3.25, we find

[1]There is no complete theory for the nucleon-nucleon interaction and the powerful nature of the strong force means the perturbative approach is not strictly valid [88, 122, 135] and can be parametrised by a single scalar value, b, referred to as the scattering length. Note that Eqn. 3.30 is not the actual potential, but a convenient representation, that reproduces s-wave scattering in the Born approximation.

that

$$\hat{A} = \frac{2\pi\hbar^2}{m}\sum_l \alpha_l \exp(i\mathbf{Q}\cdot\mathbf{R}_l) \tag{3.35}$$

$$\hat{B} = \frac{2\pi\hbar^2}{m}\sum_l \beta_l \hat{\mathbf{I}}_l \exp(i\mathbf{Q}\cdot\mathbf{R}_l) \tag{3.36}$$

To evaluate the effect on scattering, we must consider the expression for the cross section and revisit the matrix element (see equation 3.27). We will assume that the nuclear spins are randomly orientated, which is valid expect at ultra-low temperatures [2, 162]. Any terms linear in $\hat{\mathbf{I}}$ will disappear: hence the last three term in equation 3.27 vanish, the first term is independent of nuclear spin and the second term will remain.

At this stage, it is also useful to consider the effects of different isotopes, which we do by averaging our results over the varying isotope distributions. We now find 3.27 becomes:

$$\mathcal{O}\mathrm{Tr}(\hat{\rho}\hat{V}^{+}\hat{V}) = \hat{A}^{+}\hat{A} + \mathcal{O}\left\{\hat{B}^{+}\cdot\hat{B}\right\} \tag{3.37}$$

$$= \sum_l\sum_{l'} e^{\{i\mathbf{Q}\cdot(\mathbf{R}_l-\mathbf{R}_{l'})\}}\left\{\alpha^*_{l'}\alpha_l + \tfrac{1}{4}\mathcal{O}(\beta^*_{l'}\beta_{l'}\hat{\mathbf{I}}'_l\cdot\hat{\mathbf{I}}_l)\right\} \tag{3.38}$$

$$= \sum_l\sum_{l'} e^{\{i\mathbf{Q}\cdot(\mathbf{R}_l-\mathbf{R}_{l'})\}}\times\left[|\overline{\alpha}_l|^2 + \delta_{l,l'}\left\{\overline{|\alpha_l|^2} - |\overline{\alpha_l}|^2 + \tfrac{1}{4}\overline{|\beta_l|^2 I_l(I_l+1)}\right\}\right] \tag{3.39}$$

where the average over nuclear spin orientations is denoted by the operator, $\mathcal{O}$, and the averaging over isotope distribution is included in the last line and denoted by a bar. This expression has been written with the coherent and incoherent parts separated, and shows that the cross section is independent of the starting neutron polarisation.

It is also of interest to look at the effect on neutron polarisation from the scattering process. To do this we need to evaluate equation 3.29, so after nuclear spin and isotope averaging, and following a similar approach to the derivation of equation 3.39, we find

[180]:

$$\mathcal{O}\mathrm{Tr}(\hat{\rho}\hat{V}^{+}\sigma\hat{V}) = \mathbf{P}\left\{\hat{A}^{+}\hat{A} - \tfrac{1}{3}\mathcal{O}(\hat{B}^{+}\cdot\hat{B})\right\} \tag{3.40}$$

$$= \sum_{l}\sum_{l'} e^{\{i\mathbf{Q}\cdot(\mathbf{R}_l - \mathbf{R}_{l'})\}} \times \mathbf{P}\left[|\overline{\alpha}_l|^2 + \delta_{l,l'}\left\{\overline{|\alpha_l|^2} - |\overline{\alpha_l}|^2 - \tfrac{1}{12}\overline{|\beta_l|^2}\, I_l(I_l+1)\right\}\right] \tag{3.41}$$

We may now compare equation 3.39 with 3.41, and note the following: the nuclear coherent and isotope incoherent scattering polarisations remain unchanged. However, random nuclear spin orientations reduce the polarisation by $\frac{1}{3}$; as one third of the time the interaction will scatter the neutron without spin-flip, whereas the remaining two thirds of the time, spin flip scattering will occur, reducing the polarisation and giving it opposite sign.

Magnetic scattering

Neutrons and electrons both have a magnetic moment, which leads to an interaction between them and makes the neutron an effective probe for the magnetic order of electron spins.

The magnetic component from the electrons arises from both spin and orbital contributions. The result of this is an interaction with the neutron that is more complicated than the nuclear scattering potential and has the form [123, 180]:

$$\hat{V}(\mathbf{Q}) = r_0\sigma\cdot\hat{\mathbf{M}}_{\perp} \tag{3.42}$$

where r_0 is a constant of proportionality and $\hat{\mathbf{M}}_{\perp}$ are defined as:

$$r_0 = \frac{\mu_0}{4\pi}\frac{e^2}{m_e} \tag{3.43}$$

$$\hat{\mathbf{M}}_{\perp} = \tilde{\mathbf{Q}}\times(\hat{\mathbf{M}}\times\tilde{\mathbf{Q}}) \tag{3.44}$$

and

$$\hat{\mathbf{M}} = -\frac{1}{2\mu_B}\int \mathbf{M}(\mathbf{r})\exp(i\mathbf{Q}\cdot\mathbf{r})d\mathbf{r} \tag{3.45}$$

From equation 3.45, we find that only magnetic components perpendicular to the unit scattering vector, $\tilde{\mathbf{Q}}$, give a finite contribution to the cross section[2].

In contrast to the nuclear component, there is no $\hat{A}$ term so we have $\hat{\mathbf{B}} = r_0\hat{\mathbf{M}}_\perp$. Again, we evaluate the effect this potential has on the cross section and find that it depends on the incident polarisation relative to the magnetic field generated by the electron spins:

$$\mathrm{Tr}(\hat{\rho}\hat{V}^+\hat{V}) = \hat{\mathbf{B}}^+\hat{\mathbf{B}} + i\mathbf{P}\cdot(\hat{\mathbf{B}}^+ \times \hat{\mathbf{B}}) \tag{3.46}$$

In polarised neutron experiments, it is important to calculate the effect on the final neutron polarisation, which has a cross section proportional to:

$$\mathrm{Tr}(\hat{\rho}\hat{V}^+\sigma\hat{V}) = \hat{\mathbf{B}}^+(\hat{\mathbf{B}}\cdot\mathbf{P}) + (\hat{\mathbf{B}}^+\cdot\mathbf{P})\hat{\mathbf{B}} - \mathbf{P}(\hat{\mathbf{B}}^+\hat{\mathbf{B}}) - i(\hat{\mathbf{B}}^+ \times \hat{\mathbf{B}}) \tag{3.47}$$

The first three terms describe a polarised beam. The neutron polarisation will remain unchanged (non-spin flip scattering) if the neutron polarisation is parallel to $\hat{\mathbf{B}}$; alternatively if the polarisation is perpendicular, then the scattered beam will have the polarisation reversed (spin flip scattering).

These processes are key to understanding a polarised neutron experiment and the results of these polarisation effects and the underlying geometry of the spins and scattering vector are shown in a cartoon in figure 3.10.

The last chiral $i(\hat{\mathbf{B}}^+ \times \hat{\mathbf{B}})$ term in equation 3.47 means a non-collinear magnetic structure will polarize an initially unpolarized beam.

Nuclear and magnetic scattering

In a neutron scattering experiment, both nuclear and magnetic scattering will be present. We have seen that $\hat{A}$ terms come from nuclear contributions only, while

[2]This is the reason why there is no scattering from longitudinal moments parallel to the $\mathbf{Q} = (0\ 0\ 1)$ reflection, as mentioned in section 3.2.2 and 3.2.3.

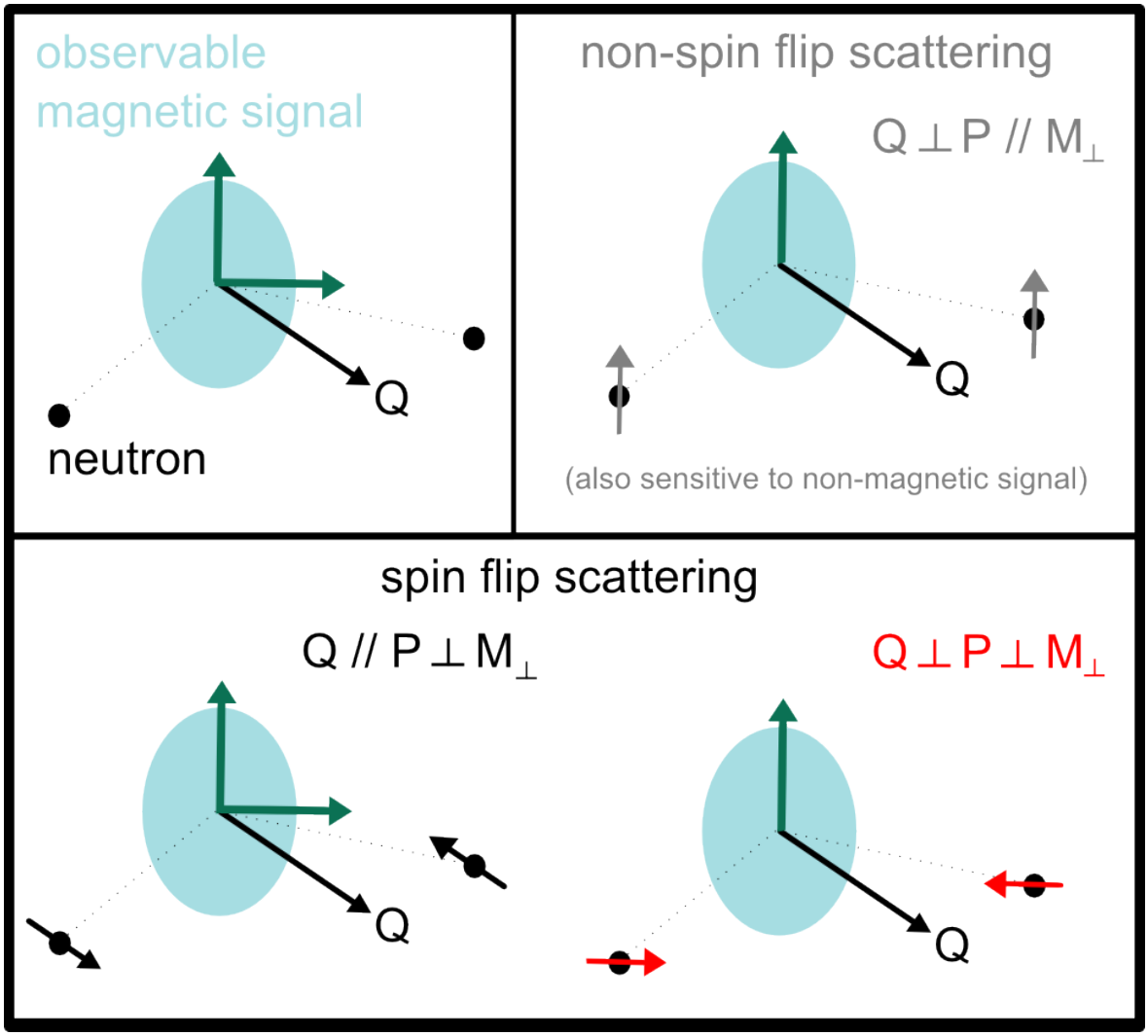

Figure 3.10: A cartoon showing the different magnetic scattering processes that are dependent on the relative orientations of neutron polarisation ($\mathbf{P}$), sample magnetisation ($\mathbf{M}_\perp$) and scattering vector ($\mathbf{Q}$). Top left: the possible observable magnetic signal is in a plane perpendicular to $\mathbf{Q}$. Top right: if the neutron spin is parallel to $\mathbf{M}_\perp$, then the neutron spin is not flipped. Bottom row: there are two possible geometries that flip the spin of the neutron: with the neutron spin either parallel or perpendicular to $\mathbf{Q}$, whilst perpendicular to $\mathbf{M}_\perp$.

the $\hat{\mathbf{B}}$ terms arise from both nuclear and magnetic parts, which can complicate the interpretation.

The expression for scattered neutron polarisation is proportional to $\mathrm{Tr}(\hat{\rho}\hat{V}^{+}\sigma\hat{V})$ (equation 3.29), which is repeated here for clarity:

$$\begin{aligned}\mathrm{Tr}(\hat{\rho}\hat{V}^{+}\sigma\hat{V}) &= \hat{A}^{+}\hat{\mathbf{B}} + \hat{\mathbf{B}}^{+}\hat{A} + \hat{A}^{+}\hat{A}\mathbf{P} \\ &\quad + \hat{\mathbf{B}}^{+}(\hat{\mathbf{B}}\cdot\mathbf{P}) + (\hat{\mathbf{B}}^{+}\cdot\mathbf{P})\hat{\mathbf{B}} - \mathbf{P}(\hat{\mathbf{B}}^{+}\cdot\hat{\mathbf{B}}) \\ &\quad - i(\hat{\mathbf{B}}^{+}\times\hat{\mathbf{B}}) + i\hat{A}(\hat{\mathbf{B}}\times\mathbf{P}) + i(\mathbf{P}\times\hat{\mathbf{B}}^{+})\hat{A}\end{aligned}$$

As nuclear and magnetic scattering occurs together, there are now interference terms from these processes that in the magnetic case, we could previously ignore (i.e. mixed $\hat{A}$ and $\hat{\mathbf{B}}$ terms that now remain).

Many materials do not have isotopes of different spin, which means the nuclear $\hat{\mathbf{B}}$ terms vanish. Also, as discussed earlier, the nuclear moments are randomly orientated (apart from at the lowest temperatures). Therefore, it is a useful approximation to associate the $\hat{\mathbf{B}}$ terms solely with the magnetic scattering (and $\hat{A}$ terms with nuclear origins) [123].

Correlation functions

The interaction of neutrons with the electrons and nuclei of system of study have been presented, which results in experimentally measured cross sections. It is now important to relate this observed quantity to the physics in the system; to do this, a brief introduction into the formalism of *correlation functions* will now be presented.

The cross section measured will be from an ensemble of nuclear and magnetic spins, so a real experiment will always probe the thermal average. The matrix element part of the cross section contains all the information about the physics in the system. We

define the scattering function, $S(\mathbf{Q},\omega)$, as

$$S(\mathbf{Q},\omega) = \frac{1}{2\pi\hbar}\int G(\mathbf{r},t)\exp\left\{i(\mathbf{Q}\cdot\mathbf{r}-\omega t)\right\}d\mathbf{r}dt \tag{3.48}$$

such that

$$\left(\frac{d^2\sigma}{d\Omega dE'}\right)_{\text{coh}} = \frac{\sigma}{4\pi}\frac{k'}{k}NS(\mathbf{Q},\omega) \tag{3.49}$$

where we have also introduced the time-dependent pair-correlation function, $G(\mathbf{r},t)$, and N is the number of elements in the scattering system [188]. The quantity $S(\mathbf{Q},\omega)$ is related to $G(\mathbf{r},t)$ by Fourier transform in the space and time domains.

For the nuclear case, the correlation functions represents the correlations in the nuclear density in either real ($\mathbf{r}$) or reciprocal ($\mathbf{Q}$) space. For magnetic scattering, the correlation functions quantify the spin density correlations.

In a scattering experiment, the neutron can either gain or lose energy when interacting with the sample. For the system to give the neutron energy, it must have sufficient energy itself and therefore is linked to temperature. This asymmetry between neutron energy loss and gain is accounted for by *detailed balance* [122] so:

$$S(\mathbf{Q},\omega) = \exp\left(\frac{\hbar\omega}{k_BT}\right)S(-\mathbf{Q},-\omega) \tag{3.50}$$

Attenuation effects

Due to the highly penetrating nature of neutrons, the effects of neutron attenuation by the sample are normally ignored, however, in some cases this can appreciable. In the case of inelastic neutron scattering, the scattered amplitudes are often low: a combination of long count times and large mass samples are needed to maximise the measured intensity and improve the signal to noise ratio. The large sample used in this work (7 g) is approximately 1.7 cm^3 and has a attenuation length $\sim$ 3 cm and so presents noticeable attenuation. In general, particularly strong scattering can also lead to secondary (or multiple) Bragg scattering from the sample.

Neutron attenuation is governed by two effects; which are from neutron scattering

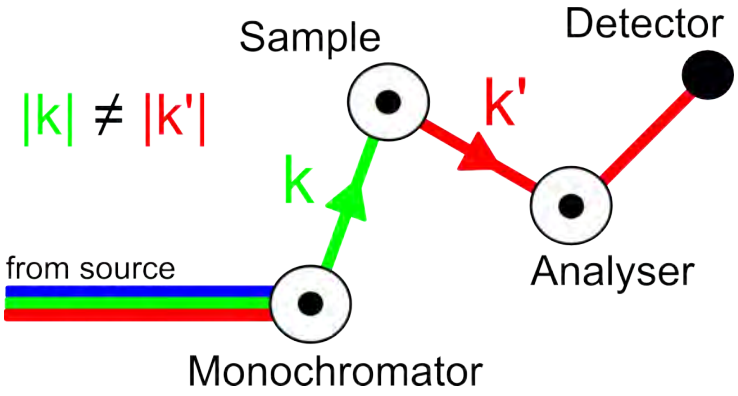

Figure 3.11: Schematic of a typical triple axis spectrometer setup. The monochromator sets the initial wavelength and by moving the sample, **k** can be selected relative to the sample's underlying crystal axes. By moving the analyser and detector, $\mathbf{k}'$ can be uniquely defined and hence also **Q** and the energy transfer.

(both coherent and incoherent cross sections contribute) and neutron absorption effects. This will not be discussed further but more details can be found in reference [166].

3.4.2 Neutron scattering instrumentation

Inelastic neutron scattering setups

When measuring scattering to finite energy transfers, $\hbar\omega$, there are currently no effective neutron calorimeters (i.e. with high enough detection efficiency and energy resolution). The main setups to measure inelastic neutron spectra are triple-axis, time of flight, backscattering and neutron spin echo spectrometers. Whilst different techniques have their advantages (such as large reciprocal-energy space coverage or excellent energy resolution), triple axis spectrometry has the most suitable geometry to place the guide fields and flippers that are needed for full polarisation analysis. The principles behind triple axis spectrometry will now be discussed and a schematic of a typical triple-axis instrument is shown in figure 3.11.

On triple axis spectrometers, neutrons of a known wave vector, **k**, impact on the

sample (this is selected by a monochromating element and is the *first* axis). These neutrons are then scattered so have a new wave vector, $\mathbf{k}'$ (this is the *second* axis). The scattering process can be described by a momentum transfer vector, $\mathbf{Q}$. Whilst the direction of $\mathbf{k}'$ is well defined (by measuring it with a detector at a given angle), the magnitude of k' and hence the energy transfer are unknown. The wavelength, and hence the energy transfer, of these scattered neutrons can be determined by Bragg scattering from an analyser crystal of known inter-atomic spacing (and represents the *third* axis).

In practise specifying any two pairs from $\mathbf{k}$, $\mathbf{k}'$ or $\mathbf{Q}$, uniquely selects the third (this is known as *closing the triangle*). It is common to operate in *constant* k_f (or k' mode, where this refers to the modulus of the scattered neutron wave vector only) as this makes the normalised intensity directly proportional to $S(\mathbf{Q},\omega)$ and resolution effects constant for a given scan [27, 32].

Neutron polarizers

The neutron beam from a reactor or spallation source is unpolarized, so the neutrons must be prepared by selecting a certain polarisation and discarding the remainder. For this reason, the intensity and resulting signal-to-noise ratio is much reduced as much of the neutron beam is unused, so high polarisation efficiencies and low losses are required.

One method for polarising neutron beams is to use a polarising monochromator. The operation of these can be understood from considering the scattered polarisation from a magnetic system (equation 3.29). Here there are three terms that give a polarisation from an unpolarised beam: the $\hat{A}^{+}\hat{\mathbf{B}}$ and $\hat{A}\hat{\mathbf{B}}^{+}$ terms from spin and nuclear interference, and the chiral magnetic term, $i(\hat{\mathbf{B}}^{+} \times \hat{\mathbf{B}})$. In polarisation setups, it is these spin-nuclear terms that are used to polarise the neutron beam.

These first two terms exist in a ferromagnet, as the nuclear and magnetic parts have

the same wavevector; assuming random nuclear spins and associating the $\hat{\mathbf{B}}$ terms with the electrons spins (section 3.4.1). The nuclear reflection ($\hat{A}^{+}\hat{A}$ terms) can be minimised by selecting a forbidden structural reflection.

At the ILL, where this work took place, the $\mathbf{Q}$ = (1, 1, 1) reflection was used to polarise the neutron beam from the Heusler alloy, Cu_2MnAl, that can achieve neutron polarisations greater than 90 % [37].

This technique can be extended to create polarizing supermirrors, where multi-layers stacks of weak ferromagnetic and non magnetic material can achieve even higher levels of polarisation [130, 161].

An alternative approach is to use ^{3}He polarizing filters. ^{3}He is a spin $1/2$ nucleus and has a strong neutron capture cross section, with anti-parallel neutron spins absorbed allowing the remaining polarised beam to be used [53].

Unlike polarising monochromators, where the system is itself highly polarised, the limiting factor for ^{3}He filters is polarizing the ^{3}He nuclei, which is achieved through optical pumping [161]. ^{3}He filters have the advantage of having a wide angular and broadband wavelength acceptance (in contrast to supermirrors).

Neutron polarisation setups

Once the neutron beam has been polarised, the beam polarisation must be maintained before and after scattering from the sample. This is achieved by use of guide fields, where constant magnetic fields ($\sim$ 1 mT) perpendicular to the neutron polarisation, maintain the beam polarisation. Furthermore, by adiabatically changing the orientation of the magnetic field, the neutron polarisation can be rotated without loss of polarization.

The field can be changed non-adiabatically causing the neutron spin to precess around the field direction. This can be implemented in a Mezei flipper which can allow the polarisation to be flipped by π or $\pi/2$. Alternatively, RF (radio frequency)

flippers (as found in our experimental setup on IN22) can flip the neutron polarisation by applying an RF pulse on the same energy scale as the Larmor frequency.

If we consider spin flippers before and after the sample and change which spin flippers are turned on, an initially polarised beam can now access the $\langle\uparrow \mid \uparrow\rangle$, $\langle\uparrow \mid \downarrow\rangle$, $\langle\downarrow \mid \uparrow\rangle$ and $\langle\downarrow \mid \downarrow\rangle$ cross sections (an additional analyser is also required to resolve final neutron polarisation state). By combining this setup with adiabatic spin rotation, polarisation can be rotated relative to the scattering vector and crystal/magnetic structure.

Since the pioneering work of Moon *et al.* [134], this technique has been used to resolve many magnetic structures and form factors. For example, if the neutron polarisation is parallel to **Q**, then magnetic and nuclear scattering can be separated from the spin flip and non-spin flip scattering (assuming random nuclear spins). In the absence of a nuclear reflection (for example at a forbidden structural Bragg reflection), the direction of the magnetic signal can be determined from the spin flip or non-spin flip components if the polarisation is perpendicular to **Q**. These processes are illustrated in figure 3.10 on page 69.

3.5 Experimental setup

Polarized neutron measurements were made using a Helmholtz coils setup on the triple-axis spectrometer IN22 at the Institut Laue-Langevin, Grenoble. Initially we had intended to use the CRYOPAD setup, which involves a superconducting jacket, to exclude magnetic fields and maintain high neutron polarisation; however, this was made unavailable due to a quench at the start of the experiment.

Measurements were made in fixed final energy mode ($k_f = 2.662$ Å^{-1}) in the standard Heusler-Heusler monochromator-analyser configuration. The beamline layout is shown in figure 3.12.

USb has an fcc NaCl structure ($a = 6.197$ Å) and a single crystal (7 g) of USb was

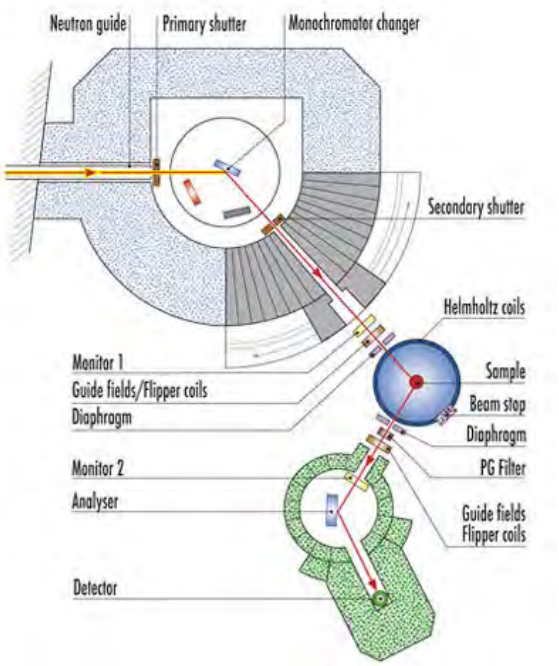

Figure 3.12: Overview of the triple axis spectrometer on the IN22 beamline, ILL, France (from Ref. [74]).

used, the same as in the study by Magnani *et al.* [126].

3.5.1 Polarised neutron scattering setup

The sample was aligned to access the (1 0 0)-(0 1 0) scattering plane. We focus on the spin flip (SF) channel in order to exclude phonon contributions and detect magnetic scattering at $\mathbf{Q}$ = (1, 1, 0) [this magnetic Bragg peak arises from the nuclear zone centre at (1 1 1) minus the magnetic propagation vector (0 0 1)]. We define the xSF neutron polarisation direction as parallel to $\mathbf{Q}$ (i.e. in the [1 1 0] direction) and it is sensitive to the total magnetic fluctuations in the plane perpendicular to $\mathbf{Q}$. ySF and zSF polarisation channels are along the [$\bar{1}$ 1 0] and [0 0 1] crystal directions, respectively: this setup is shown in figure 3.13. The former probes the component of the magnetization fluctuations along [0 0 1], the latter along [$\bar{1}$ 1 0].

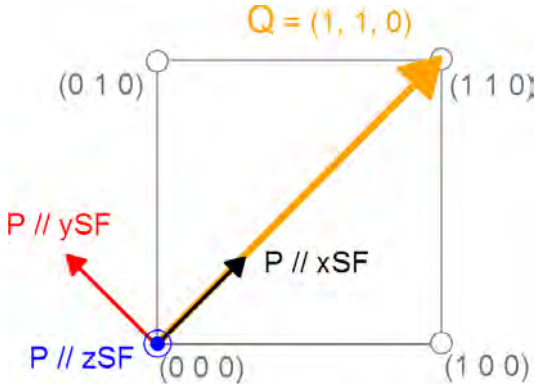

Figure 3.13: Schematic of scattering geometry showing the polarisation axes (colour) relative to underlying crystal structure (dark grey).

As in the previous work by Magnani *et al.* in this geometry [126], the *ySF* neutrons select the acoustic mode exclusively (as they are sensitive to magnetic fluctuation in the $\langle 0\ 0\ 1\rangle$-type directions), whilst the *zSF* channel selects the optical magnon (sensitive to magnetic fluctuations along $[\bar{1}\ 1\ 0]$ (this was shown in Fig. 3.8 in the original discussion of spin waves on page 55). Note that although the measurements are at a **Q** where the Bragg peak is generated by one component, the magnetic fluctuations are sensitive to the total ordered moment, which is along $\langle 1\ 1\ 1\rangle$ in the 3-**k** state.

Below T^*, where the 3-**k** structure has well defined spin waves, the ySF/zSF intensity ratio will be equal to some maximal value (equal to the flipping ratio, determined by the incident neutron polarisation). However, for spins pointing along the local $\langle 1\ 1\ 1\rangle$-directions in the absence of any phase relationship, the ratio of ySF/zSF will tend to $\sqrt{2}$ (due to projections of the spins onto the chosen polarisation axes).

This setup can unambiguously resolve the optical and acoustic modes into the different polarization channels and so makes it ideal for testing the de-phasing hypothesis above T^*, where there are no clearly defined spin waves and the spectral weight becomes quasielastic. Therefore, if the Fourier components de-phase, the relative integrated intensities in the *ySF* and *zSF* channels must also change.

The flipping ratio was found to be 13.7 in the x, y and z channels. The inelastic polarized spectrum was measured at $\mathbf{Q}$ = (1, 1, 0) from -2 to 13 meV (we focussed on the acoustic mode only). We measured at nine temperatures: from 40 K to 300 K at $\mathbf{Q}$ = (1, 1, 0) (from below T^*, to above T_N). Measurements were also made at $\mathbf{Q}$ = (1.2, 1.2, 0), in both spin-flip and non-spin-flip (NSF) channels at a few key temperatures to provide a cross-check of our results.

3.5.2 Data analysis methods

The resolution function for the setup was not directly measured during the experiment. However, the resolution function was estimated by normalising the fitted the elastic response (minus a constant background signal) at low temperatures, where the Debye-Waller broadening due to thermal motion should be minimal. From this analysis, the energy resolution was 0.56 meV full width half maximum at the (1, 1, 0) elastic position in good agreement with expected values based on the particular instrumental setup.

It was found that all inelastic spectra could be parametrised using the same three components:

- an inelastic two-pole Lorentzian function (for positive and negative energy transfer) weighted by the Bose distribution and convoluted with the instrumental resolution function (details can be found in reference [165]). This function was chosen as it allows for a continuous variation of this component from an inelastic spin wave type-component at finite energy transfer, to a quasielastic response centred about zero energy transfer.

- an elastic component, centred about the zero of energy, convoluted with the resolution function

- a constant background term.

A Levenberg-Marquardt nonlinear regression fitting algorithm was used to fit the data in MATLAB®. The normalisation was carried out using a built-in MATLAB function, *quadv*, which uses an adaptive Simpson quadrature able to numerically evaluate integrals. The convolution between the response and the resolution function was calculated using the *conv* function.

It proved difficult for the fits to distinguish the weak quasielastic response above a strong (and fairly broad elastic line) and background, which led to large uncertainties in the quasielastic integrated intensity and width: the fitting algorithm was preferentially fitting closely to the elastic line, at the expense of the quasielastic signal. To give more reliable quasielastic fits, the $\log_{10}$ of the normalised intensity was fitted (and the errors treated accordingly) to bring more weight to low intensity, whilst still giving excellent parametrisation of the strong elastic signal (and close agreement with linear fits to the data).

A graphical front-end was also written in MATLAB to allow easy modification of fit parameters and fast display of results, whilst also allowing batch processing of data sets to be scripted (this is shown in appendix 3.A).

All counts were assumed to have a Poisson noise distribution, i.e. the errors are $\sim \sqrt{N}$, where N is the number of counts. This error was used for weighting the residuals ($\sim \frac{1}{N}$) and calculating the fit curve.

3.6 Results & analysis

A proxy for the AFM order parameter as a function of temperature was obtained by measuring rocking curves of the elastic $\mathbf{Q} = (1, 1, 0)$ Bragg reflection and extracting the integrated intensity (figure 3.14). The effect of extinction is clearly present at the lowest temperatures as a kink in integrated intensity however, no correction for this is made. The data near the transition were fitted to a general order parameter function

of the form:

$$\begin{aligned} I = \quad & I_0 \left(1 - \tfrac{T}{T_N}\right)^{2\beta} + BG \qquad && \text{for } T < T_N \\ I = \quad & BG && \text{for } T > T_N \end{aligned} \tag{3.51}$$

where I is the integrated intensity, I_0 is the integrated intensity at zero temperature, β is the critical exponent and BG is a constant background term.

The Néel temperature ($T_N = 216.8 \pm 0.8$ K) and critical exponent ($\beta = 0.33 \pm 0.06$) were extracted. These results were in close agreement with published values [87, 111, 139].

Inelastic spectra were measured in the temperature range 40 to 300 K at $\mathbf{Q} = (1, 1, 0)$ using polarised neutrons: a sample of the results are shown in figure 3.15 (the full results can be found in Appendix 3.B on page 95). At low temperatures, a well defined

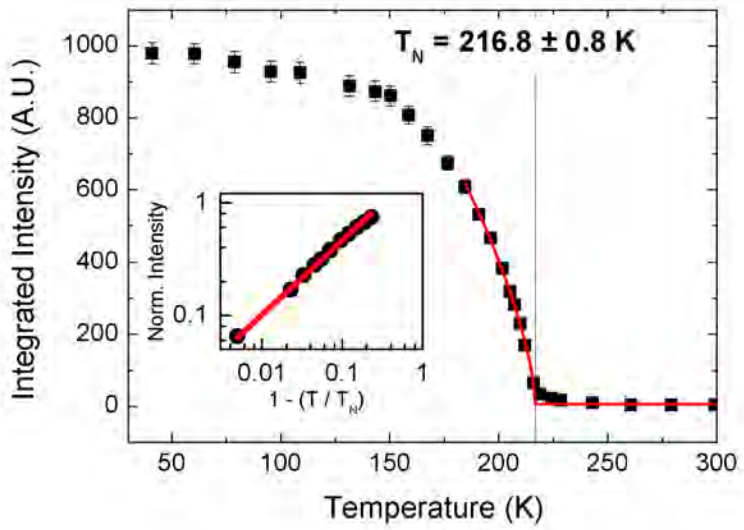

Figure 3.14: The $\mathbf{Q} = (1, 1, 0)$ Bragg integrated intensity (black squares) serve as a proxy for the AFM order parameter (fitted with order parameter - red curve). Inset: log-log plot of the (1, 1, 0) intensity against reduced temperature. The error bars are based on the fit errors on the integrated intensity.

spin wave was measured in the xSF and ySF channels, that broadened and became quasielastic around T^* (see Fig. 3.15a & 3.15b), in excellent quantitative agreement with previous results [66, 126].

We note that in the zSF channel, there is a small amount of narrow quasielastic broadening at 150 K (and also at 120 K, not shown), which is absent at 40 K. Although fits to this feature and extraction of the integrated intensity were unsuccessful because of the relatively strong elastic signal; there is a clear quasielastic contribution in the zSF which is present above leak-through (see dashed-dotted line in Fig. 3.15). The origin of this scattering is as yet unknown. One possibility might be magnetic domain wall motion appearing in all polarisation channels, which freezes out below T^* and this is discussed in the following section.

Figure 3.15c shows the inelastic polarized neutron spectrum above T^* and is characteristic of all spectra in the range T^* to T_N: centred about zero energy transfer is the AFM elastic Bragg peak and a smaller broad quasielastic contribution.

Here, the intensity in the tails is much greater in the ySF channel compared to the zSF channel. This relationship was also observed at 170 K with $\mathbf{Q} = (1.2, 1.2, 0)$, where magnon-phonon coupling can be safely ignored. The large differences in intensities between the different polarisation components indicates that the Fourier components do not fully de-phase above T^*.

Measurements were taken at $\mathbf{Q} = (1.2, 1.2, 0)$ (in SF and NSF channels) and the data, away from the strong elastic leakthrough from the magnetic Bragg peak, supports the picture at $\mathbf{Q} = (1, 1, 0)$ both above and below T^* (this data can be found in Appendix 3.B, Fig. 3.20, page 95). The NSF channel contained a phonon contribution at low temperatures that would be problematic for the data parametrisation at higher temperatures. During the experiment we chose to focus on the $\mathbf{Q} = (1, 1, 0)$ spin flip scattering to allow us to study the critical scattering over a wide range of temperatures and is the basis for the following discussion.

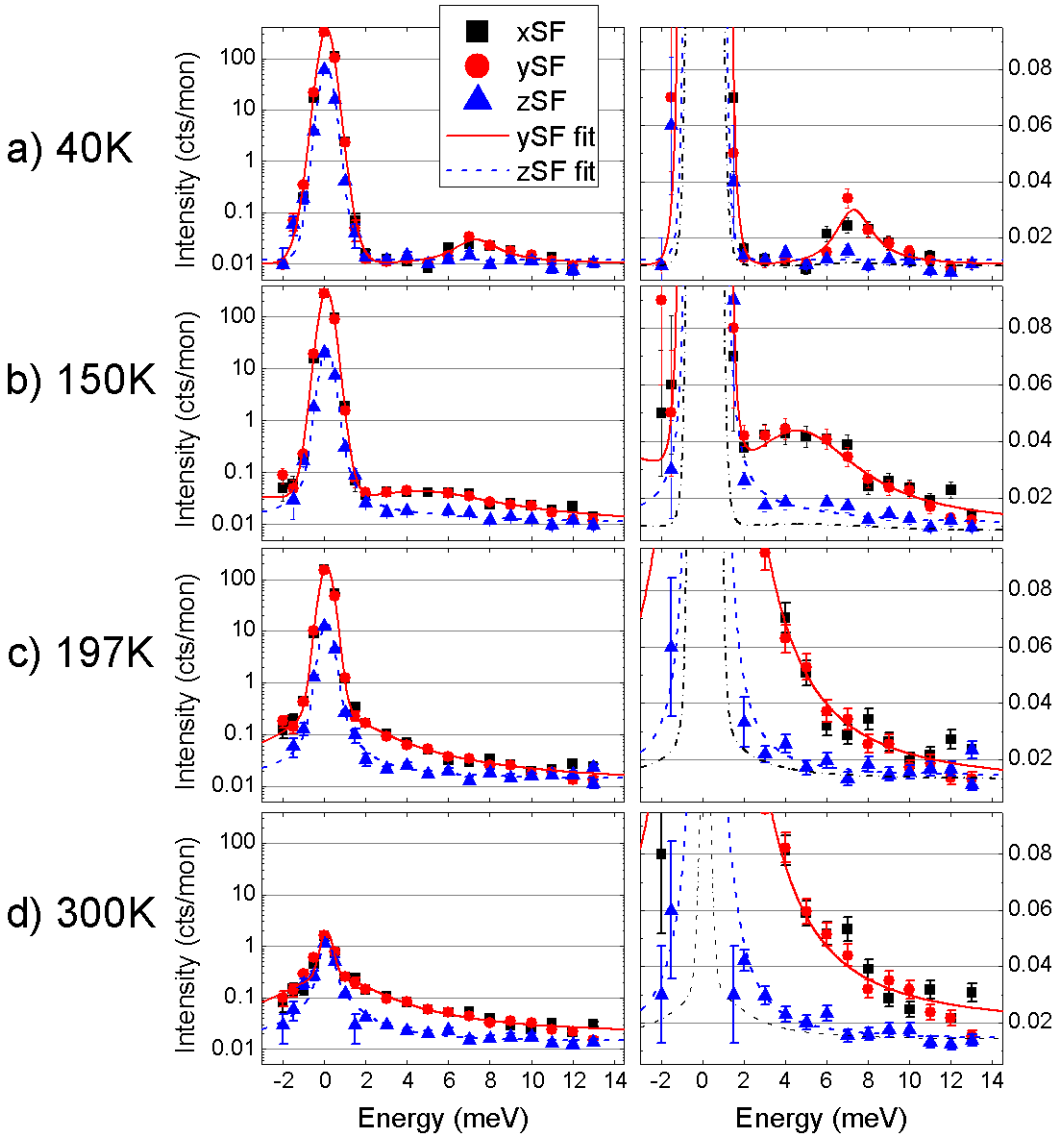

Figure 3.15: Inelastic polarized neutron spectra from the (1, 1, 0) reflection at different temperatures with the experimental data as solid points (with error bars) and lines showing fits to the data. Figures 3.15(a) & 3.15(b) show the spin waves in the xSF and ySF channels only, which broaden and collapse towards the elastic line with increasing temperature. Figures 3.15(c) and 3.15(d) show that the Fourier components do not fully de-phase above T^* and T_N, respectively. The black dash-dotted line shows an estimate of the polarisation leak-through (calculated from the flipping ratio) from the xSF into the zSF channel, showing there is a finite quasielastic component above 40 K.

The spectra above T_N (e.g. see Fig. 3.15d) no longer shows an elastic contribution from the magnetic Bragg peak and quasielastic broadening is all that remains. Surprisingly, the broad tails show the polarisation conditions remain the same above T_N, with greater spectral weight in the *ySF* channel relative to *zSF*. This noticeable anisotropy between the *ySF* and *zSF* channels implies phase correlations remain present even in the absence of static magnetic order up to $T = 1.4\ T_N$.

The quasielastic behaviour can be studied by extracting the fit parameters and a summary of results is shown in Fig. 3.16 (the full results can be found in Appendix 3.C). Due to the large elastic signal, the magnitude of the *zSF* quasielastic components could only be reliably extracted at elevated temperatures where the elastic response is

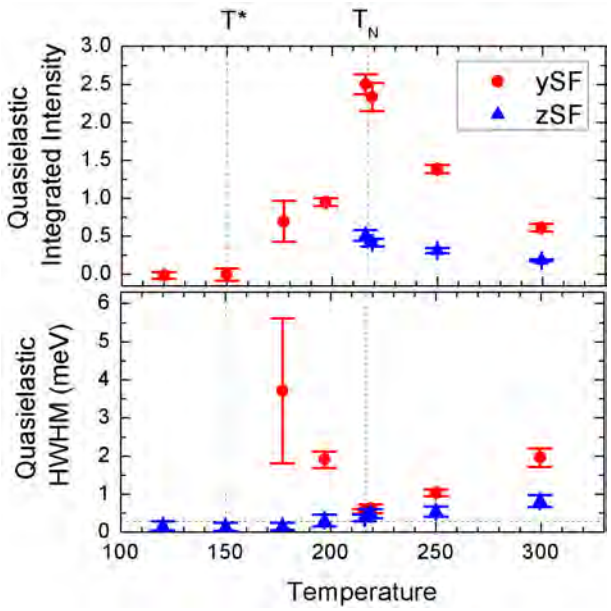

Figure 3.16: Upper panel: extracted quasielastic integrated intensities. The quasielastic signal develops only above T^* and shows divergent behaviour as expected around T_N in the *ySF* channel, however this is not seen in the *zSF* intensity. Lower panel: HWHM of the quasielastic signal, where again critical behaviour is seen in the *ySF* but not in the *zSF* (the instrumental resolution is shown by the dashed horizontal line).

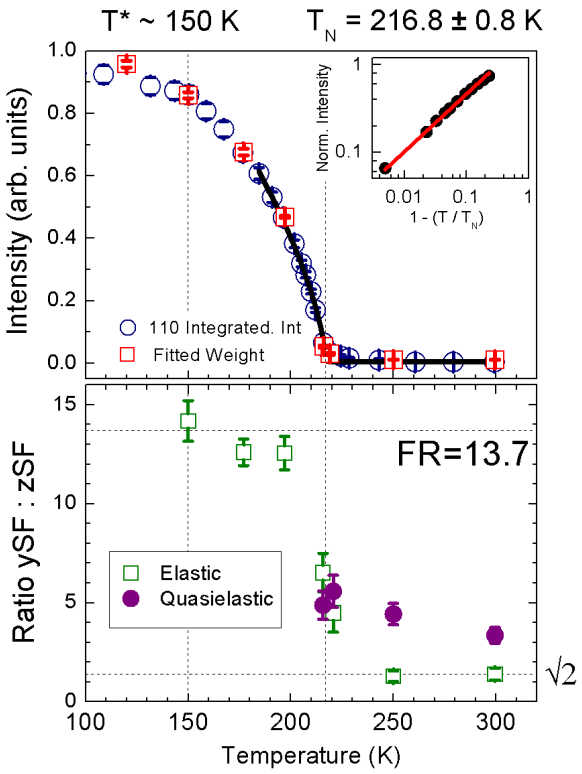

Figure 3.17: Upper panel: (1, 1, 0) Bragg integrated intensity (blue circles) and the extracted elastic intensities from fitted spectra (red squares) serve as a proxy for the AFM order parameter (fitted with critical exponent - black curve). Inset: log-log plot of the (1, 1, 0) intensity against reduced temperature. Lower panel: spectra were fitted with elastic and quasielastic components and the ratio of these integrated intensities is plotted *vs.* temperature. The ratio of the elastic components exactly follows the expected behaviour for the ordered 3-**k** state, whereas a value of the quasielastic ratio greater than $\sqrt{2}$ indicates 3-**k** correlations.

diminished. This limitation could be due, in part, to an inadequate resolution function, which was not measured directly.

Around T_N in the *ySF* channel, the quasielastic integrated intensity diverges and the width becomes narrower. This behaviour is expected and has been previously reported [66]. However, the quasielastic features in the *zSF* channel are strikingly different: the feature is much narrower and does not change on passing through the Néel temperature. This feature will be discussed in more detail later.

For comparison, it is useful to consider the ratio of the *ySF* spectral weight divided by the *zSF* spectral weight. This ratio, split into elastic and quasielastic contributions, is shown as a function of temperature in the lower panel of Fig. 3.17.

Below T_N, the elastic ratio reaches a maximal value (determined by the incident beam polarization), indicating that the *zSF* elastic intensity is due to leak-through only. Above T_N, where there is only a small non-zero elastic component to the fit, the elastic scattering equals the value of $\sqrt{2}$, as expected for incoherent magnetic scattering from spins randomly pointing along local $\langle 1\ 1\ 1 \rangle$ directions. The clear agreement of the elastic fit component with theory, indicates the data is well parametrized and the remaining signal is solely quasielastic magnetic scattering.

Above T^* in the quasielastic channel, the unequal intensities between the *ySF* and *zSF* channels mean that polarisation conditions are similar to when in the 3-**k** state (see Fig. 3.15). Around T_N and above, we are able to quantify the relative intensities in the quasielastic ratio and show this phase relationship remains and, whilst decreasing slowly, appears robust to ∼100 K above T_N (see lower panel of Fig. 3.17). The quasielastic signal cannot be from phonon leak through as this spectral weight should increase with temperature.

This result also confirms that the correlations above the Néel temperature, seen previously in neutron scattering and bulk measurements, are indeed magnetic in origin [66, 140].

3.6.1 Discussion

This discussion contains two main parts: the observed behaviour between T^* and T_N, where the spin wave becomes quasielastic with sample still antiferromagnetically ordered, and the behaviour above T_N, where there are correlations in the neutron polarisation data in the absence of long range-order.

The collapse of a spin wave mode to zero energy is often an indicator that a system is unstable against fluctuations and an associated magnetic phase transition is nearby - a feature seen in many materials [29, 192]. It is therefore unusual that on approaching T^*, no transition is seen - either in the specific heat data or in the nuclear or magnetic structure [66, 87, 140]. A possible explanation for this change is that the spins, making up the 3-**k** structure, de-phase with one another. We have been able to test this hypothesis using polarized neutrons and conclude that it does not occur.

We attribute a non-$\sqrt{2}$ value of the quasielastic ratio (i.e. greater than expected intensity in the ySF over the zSF channel) as evidence for 3-**k** correlations. This interpretation is in good agreement with theoretical and experimental results at low temperatures [79, 126] and can be generalized to higher temperatures. Hence, if the spins are uncorrelated or de-phase with one another, then the ratio should tend to $\sqrt{2}$. Conversely if some correlation persists, the ratio should be greater than $\sqrt{2}$.

Whilst we are unable to explain the cause of the mode softening at T^*, we suggest understanding of the behaviour may rely on the itinerant-local duality found in many $5f$ electron systems. In particular this points towards a more itinerant picture of USb, considering the quasielastic nature of the spin waves. Whilst much work has been done on measuring and modelling the low temperature behaviour (e.g. de Haas van Alphen measurements, spin density functional theory calculations, etc. [73, 86, 194]), more study is needed to understand the high temperature behaviour [99, 140].

It should be noted that polarized inelastic neutron scattering is unable to discern

whether any partial de-phasing is due to a mixture of fully phase-locked and fully de-phased 3-**k** structure or partial de-phasing of the whole magnet; however, one would not expect a coexistence of locked and unlocked spins considering the large temperature range over which this behaviour is seen (~ 60 K).

At low temperatures, the physical properties of USb are very well described by a mean-field model where the electrons are localized and the exchange interaction dominates, thus generating large magnetic moments pointing along the cubic cell diagonal. On the other hand, the angle-resolved photoemission spectroscopy (ARPES) determined band structure seems more consistent with an interpretation based on itinerant electrons [99]. The possible transition toward a larger degree of itinerancy at high temperatures might also help to explain some peculiar bulk properties, such as the resistivity peak corresponding to T^* [140, 164]. The spin wave becoming quasielastic at T^* is clearly an indication that the transition between the localized exchange levels, which gives rise to the observed excitations, can no longer be understood from a mean-field point of view at such high temperatures. If so, and considering that the present work disproves both the de-phasing hypothesis and any involvement of interactions with phonons, it seems natural to propose that the softening is linked to a higher degree of itinerancy, which could reduce the value of the magnetic moment, broaden the spin-wave transition and therefore also lower its energy range.

The measurements above the Néel temperature are also striking and unexpected. As the material exits the ordered AFM phase, there is little change in the zSF quasielastic scattering and the ySF:zSF ratio remains distinctly different from $\sqrt{2}$ (see lower panel of Fig. 3.17). This suggests that even in the absence of long-range order, the spins maintain a strong, partial phase relationship with one another. Indeed, the presence of these phase correlations may indeed be important in forming the multi-**k** state in USb.

It should be noted that this precursor regime (above T_N) shows persistent 3-**k**-

like correlations, which have not been previously reported. It is surprising that these correlations should extend to such high temperatures; particularly as it is the fourth order terms in a Landau free energy expansion that are needed to stabilize the 3-**k** over the single-**k** state.

It could be interesting to realize whether the strong exchange interaction, which dominates at low temperatures, is itself pushing the system toward stronger localization or if the magnetic properties are simply reflecting the effect of another driving force. The peculiar properties of the 3-**k** structure allow us to observe directly the magnetic response of the itinerant states in the zSF channel which, remarkably, does not show any critical behaviour at T_N. At a glance, the interplay between these itinerant states and the localized moment seems somewhat indirect, with the appearance of the former linked to T^* and the disappearance of the latter linked to T_N; on the other hand, the effect of the exchange interaction on the high-temperature behaviour is still clearly visible in the strong phase correlations.

A final interesting feature is the origin of the zSF signal: acoustic spin wave excitations should not give any signal in the zSF channel. It remains unclear where this signal comes from although speculation into some possible sources will now be presented.

It is uncertain from the data obtained whether this signal comes from a strong non-magnetic quasielastic feature polarised along the z-direction. The necessary data is absent so we are unable to confirm this hypothesis and although data at $\mathbf{Q} = (1.2, 1.2, 0)$ hint against this (see Appendix 3.B, Fig. 3.20), they do not directly cover the quasielastic region.

Another possibility is that the zSF signal comes from magnetic domains. As discussed in Section 3.2.1, there is one possible domain for a longitudinal 3-**k** structure of USb. We may still create a domain wall by changing the coupling (i.e. flipping or rotating) of nearby spins along some boundary: this will result in multiple and equivalent

3-**k** domains that are now separated by a phase shift: a domain wall.

Neighbouring domains are distinct from one another, not by any orientational or symmetry constraints as is usually the case, but by a phase difference at the domain wall: we may think of these different domains as *phase* domains - locally identical regions of 3-**k** longitudinal order, but separated by a phase shift in the magnetic propagation vector at the domain wall.

These domains may be mobile and if so, will give contributions in all directions (including the zSF polarisation channel). Furthermore, if domain motion is able to produce a quasielastic signal, this may explain the presence of a quasielastic ySF and zSF signal above T_N. As the spins still point along the $\langle 1\ 1\ 1 \rangle$ directions (supported by the value of the ratio in Fig. 3.17 and the large crystal field energy), fluctuations of these domains would give observable signal in the ySF and zSF channels, although expected relative make-up of the contributions (i.e. more ySF intensity over zSF) remains unclear.

It would be interesting to study these domains further and explore whether the physics at T^* has any effect on these domains and vice versa.

It should be noted that it is likely that these phase domains do exist in USb (or rather it is *unlikely* that there are no domains at all in a macroscopic sample), however, these have never been previously studied or realised. It remains unclear, however, if these domains and their dynamics are responsible for the observed inelastic neutron scattering measurements or whether it is the localised-itinerant cross-over (or a combination of both) that gives the changes in physical properties. In the next chapter, the possibility of domain dynamics will explored further using the probe of X-ray photon correlation spectroscopy.

3.7 Conclusions & outlook

The inelastic spectra of the multi-**k** antiferromagnet USb have been explored using polarised neutrons, across a broad range of temperatures. At the lowest temperatures, we observe a well defined spin waves from a localised 3-**k** magnet. However, tri-directional polarisation analysis has shown that, contrary to prediction, the Fourier components do not de-phase above T^*. The cause of the spin wave softening at T^* still remains an open question.

Notably, USb maintains phase correlations to at least $\sim 1.4\ T_N$ in its quasielastic excitations, despite possessing no long range magnetic order. This precursor region above the Néel temperature is unexpected but may be important for the formation of the 3-**k** state in USb.

This work has been published [118] and continues to give new insights and surprises into the long-standing problem of spin waves in this canonical 3-**k** magnet[3].

Two possible qualitative explanations for the change in behaviour have been put forward: a local to itinerant cross-over and a change in phase domain dynamics. It is not clear which of these two (or combinations) are responsible, however, a local-itinerant duality is found in many other actinide and uranium monopnictide systems and this change in itinerancy is the more simple of these two explanations, so might be favoured in this respect.

However, the study of domains in a 3-**k** magnet is an exciting new proposition that can be tested. A continuation of this work is proposed to again use polarised inelastic neutron scattering and carefully study the quasielastic spectra around T^*.

Here the aim is to systematically measure the temperature dependence of the quasielastic signal looking for evidence of phase domains and their dynamics (for more

[3]This work has recently been cited by Normile *et al.* as an example of resolving multi-**k** order in a material [138].

details see appendix 3.D). Using a cold neutron source increases the instrumental resolution and allows us to study the quasielastic signal more clearly. In particular, it would be of interest to study and parametrise the zSF quasielastic signal below T^* and compare this to the ySF spectral weight, around the onset of the spin wave softening.

The next chapter details the work carried out using X-ray photon correlation spectroscopy to try to resolve changes in the dynamics over longer time scales and probes the magnetic domains in USb.

Appendices:

Inelastic neutron scattering studies in USb

3.A Matlab analysis program

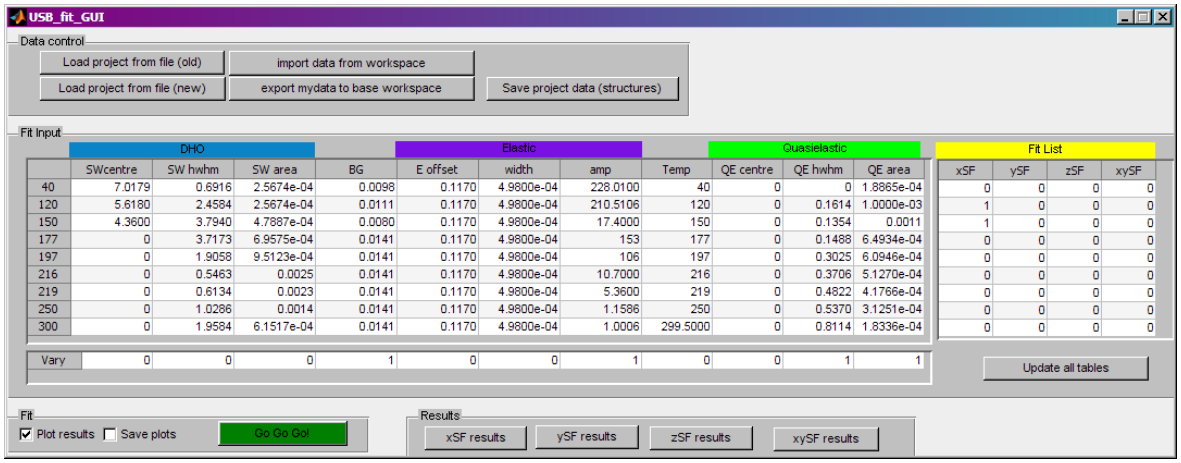

Figure 3.18: Screenshot of the GUI used to manage fits to the spectra.

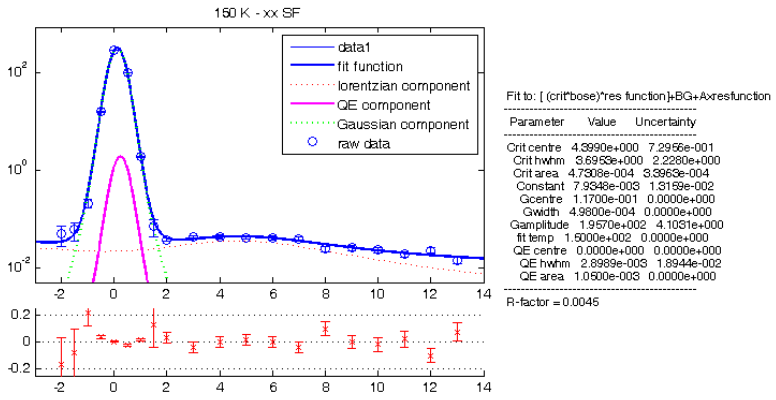

Figure 3.19: Screenshot of the output from the fitting GUI. The lower panel shows the residuals on a fixed scale (which can be set by the user) to give easy comparison between fits.

A fitting routine based on the MATLAB® code by S. P. Collins was used. A graphical front end to this routine was written in MATLAB to intuitively allow parameters to be set and change which parameters were varied (see Figure 3.18). This allowed for some play and exploration in different starting parameters, which would have otherwise been more taxing in a command line environment.

To allow batch processing of the data, it was important to be able to switch from the graphical user interface (GUI) to the MATLAB command line environment. It was also important to sensibly organise and allow saving of different fit attempts. This was implemented by holding the data in structures and automatic saving of data using check boxes.

The fit(s) would be executed with the "*Go Go Go*" button, and the user could also optionally display and save the fit results. The original data, fit curve and components, parameter summary, labels and residuals are automatically plotted to give fast feedback (see Figure 3.19).

3.B USb polarised inelastic spectra

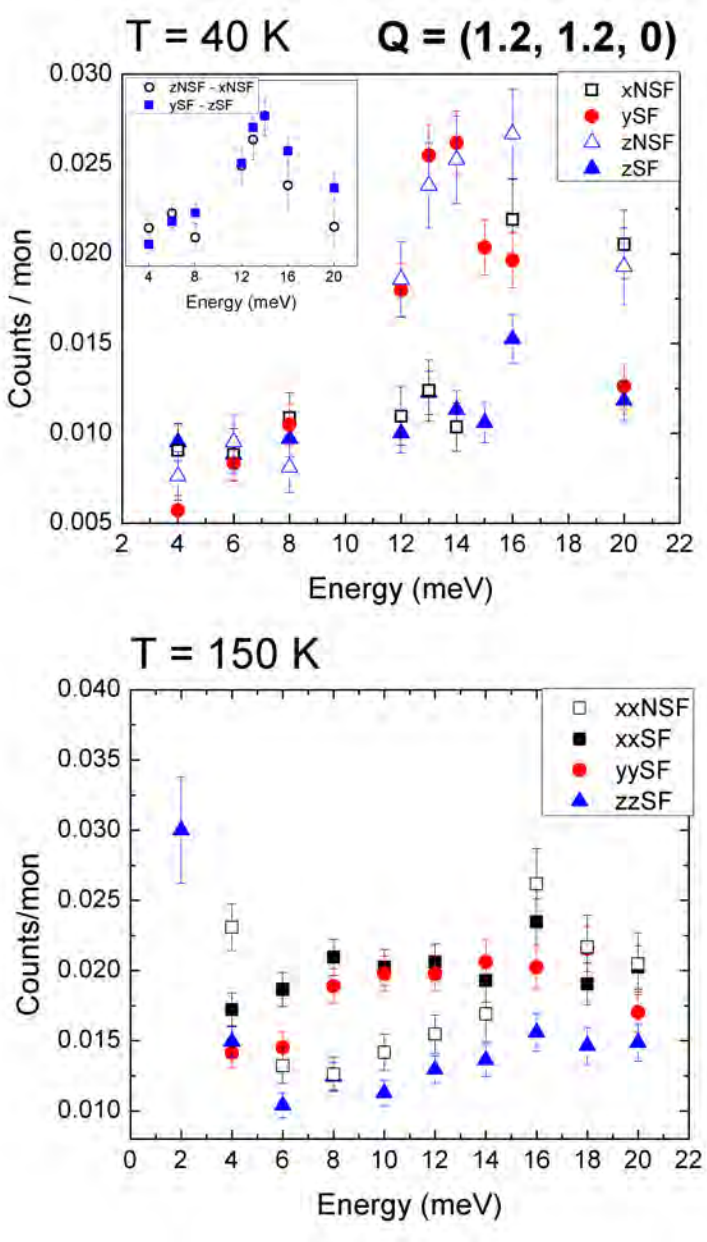

Figure 3.20: The inelastic polarised neutron spectra at $\mathbf{Q} = (1.2, 1.2, 0)$ showing the acoustic longitudinal excitation at 40 K and 150 K. Top inset: the subtractions give an estimate of the magnetic signal less background showing the spin wave clearly.

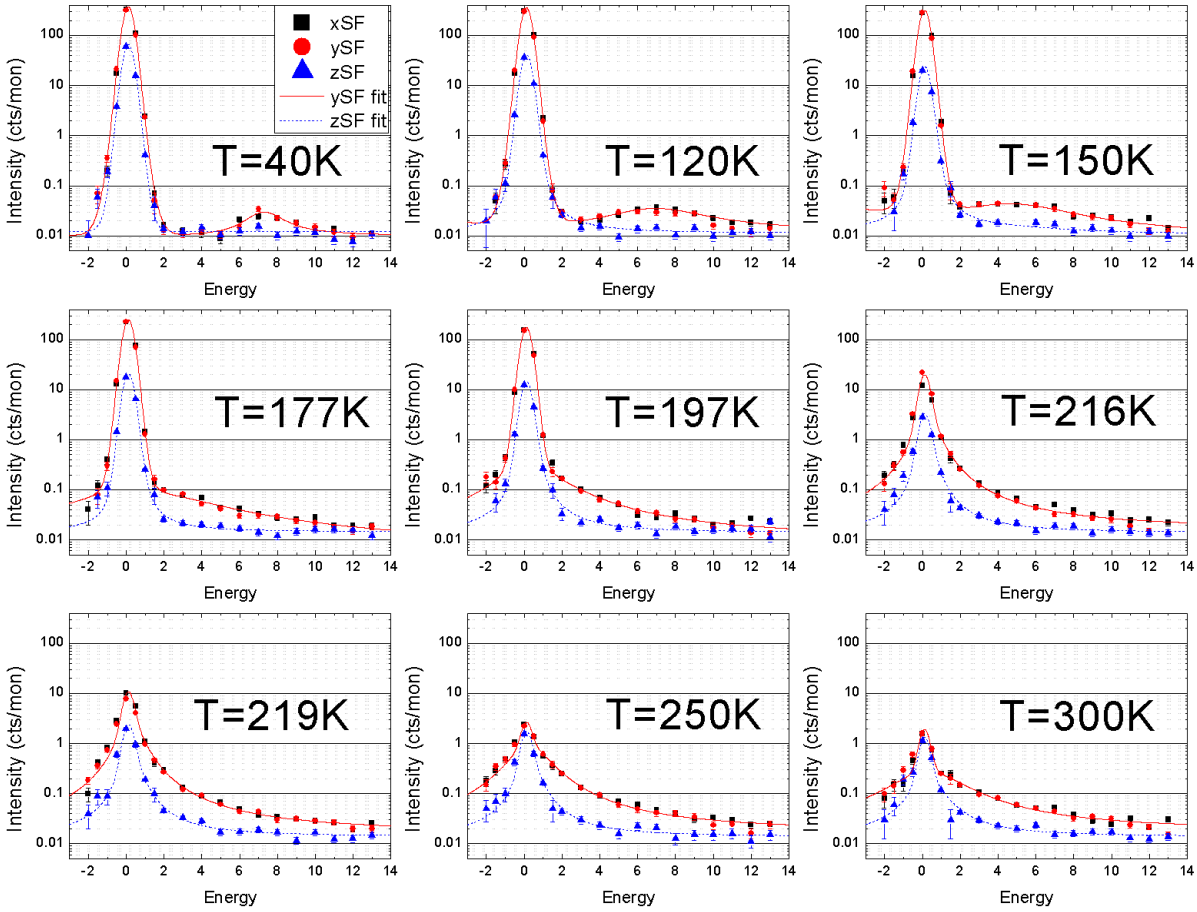

Figure 3.21: The inelastic polarised neutron spectra from USb from 40 - 300 K at $\mathbf{Q} = (1, 1, 0)$ (the solid lines are fits to the data). The damping of the spin wave and collapse can be seen with increasing temperatures. The anisotropy between the ySF and zSF is clearly present at all temperatures, indicative of 3-$\mathbf{k}$ like correlations.

3.C Fit overview to inelastic spectra

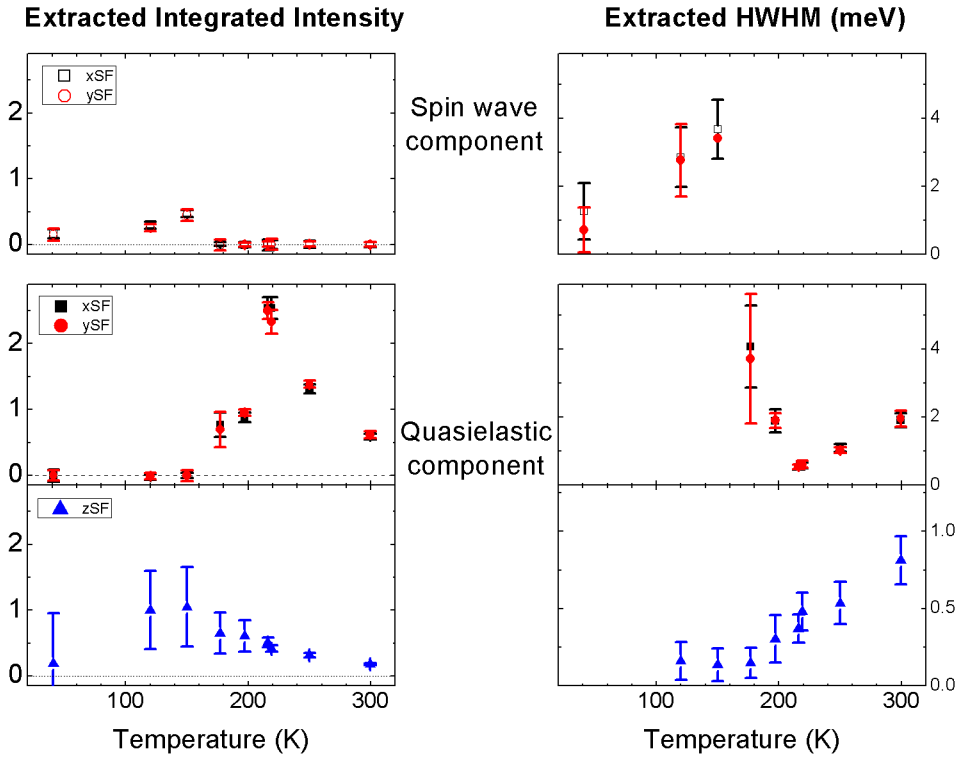

Figure 3.22: Extracted fit parameters from fitting inelastic spectra. Top panels: fits to spin wave components show dampening and collapse of spin wave approaching T^*. Lower panels: Quasielastic fit components showing critical behaviour in the case of xSF and ySF (middle panels) and smooth broadening of the zSF quasielastic signal (lower panels) that is insensitive to T_N.

3.D Proposal for continuation of inelastic studies on USb

Probing fluctuations of antiferromagnetic phase domains in USb

Scientific case

The *5f* electrons in uranium based compounds have proved a rich field of study for well over 30 years. At low temperatures, uranium antimonide (USb) looks like a well-localised 3-**k** antiferromagnet (T_N = 213 K) with well defined spin waves [1]. One surprise was that the acoustic modes appear to be longitudinal, but this is now well understood as a consequence of the 3-**k** structure, and not due to any change in the magnitude of the spins [2].

This picture is well supported at low temperatures, however, above a temperature T* (T*<T_N), the spin waves collapse with no corresponding change in the structural or magnetic symmetries [3, 4]. This change was attributed to the unlocking of the different phase components making up the 3-**k** state [5] but a recent study using polarised neutrons showed that this was not the case (see Figure 1) [6]. The change of spin wave characteristics at T* is still an open question.

Our measurements, using inelastic neutron scattering with XYZ polarisation analysis, were able to track the static and dynamic magnetic signal as a function of temperature and show that the Fourier components making up the 3-**k** state do not unlock above T* and even persist above T_N, up to at least 300 K [6].

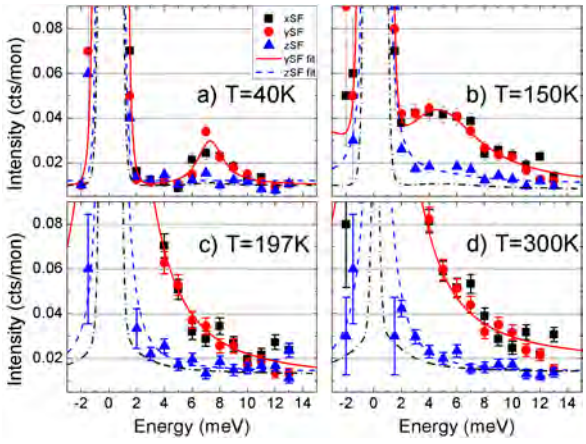

Figure 1: Inelastic polarized neutron spectra at **Q** = (110) at different temperatures (solid points are data, lines are fits to the data). Figures 1a) & 1b) show that the spin waves only exist in the xSF and ySF channels. They broaden and collapse towards the elastic line with increasing temperature.

Figures 1c) & 1d) show most of the signal remains in the ySF channel and hence the Fourier components do not fully de-phase above T* and T_N, respectively.

The black dash-dotted line shows an estimate of the polarisation leakthrough into the zSF channel, showing there is an extra quasielastic component in the zSF above 40K.

Figure 1 shows energy scans of spin-flip scattering in USb at a range of temperatures: from below T*; to above T_N. Below T* (Fig. 1a, 1b), the geometry (detailed in Ref. [7]) is such that the acoustic mode appears in the y-polarised spin flip (SF) channel and is absent in the z-SF channel. This anisotropy in the polarisation conditions is characteristic of the 3-**k** state and remains unchanged above T* and T_N, indicative of remnant 3-**k**-*like* correlations.

At all temperatures above 40 K, there is a non-zero quasielastic component (above nominal polarisation leakthrough) in the zSF channel that is not expected based on current understanding. We were able to rule out phonon contributions to this signal.

Inside the 3-**k** state, it is possible to have domains based on the phase correlations between nearby spins. These domains have no associated magnetoelastic distortions and so the energy barrier to domain wall motion might be expected to be small.

At temperatures between T* and T_N, we hypothesise that the motion of these domain walls is on a faster timescale than the spin waves, which washes out the spin wave signal, and leaving only the quasielastic excitations from the domain wall motion. Below T*, these domains walls would then freeze-in, allowing the spin waves to be observed.

This domain wall motion is a way of explaining the zSF signal observed, as this motion should give rise to a magnetic signal in all polarisation channels. It would also explain the persistence of phase correlations above T_N - here there is no static long range order, but fluctuations of these domains can be seen.

We therefore ask for beam time on a cold triple axis spectrometer with polarisation analysis to investigate this quasielastic signal, which we attribute to the motion of domains. We plan to carry out a systematic study to characterise the quasielastic spectra above and below T*, at magnetic and structural Bragg reflections to test this dynamic domain picture.

Detailed Experimental Proposal

A single crystal (7 g) is available, as used on IN22 for the work in Ref. [6, 7] and is currently at the ILL. USb has an fcc NaCl structure (a = 6.197 Å). It is a type I antiferromagnet (Q_{AFM} = [0 0 1]) with T_N = 217 K.

The sample is currently aligned to give a (100)-(010) scattering plane using the polarisation setup as described in Reference [7]. The points of interest in reciprocal space are:

- Q = [110] – we have studied this magnetic Bragg peak before, but want to use cold neutrons and the excellent energy resolution available on PANDA to focus on small energy transfers and the quasielastic signal, as a function of temperature between 40 K and 150K.
- Q = [111] (or [002]) – will act as a reference. Changes in the magnetic domains should not effect the reflections from this structural peak, as there can be no elastic energy associated with the domains of the 3-**k** structure.
- Q = [001] – For 3-**k** USb, the structure is longitudinal and parallel with the scattering vector so no static magnetic signal is expected here or has been seen before [2, 8]. However, the suggested domain fluctuations could have a small but finite quasielastic component that we will look for. As Fig. 1 illustrates, this will be very small, and so this part should initially be done without polarisation analysis to maximise the incident flux.

We have successfully used this technique to look at multi-**k** structures on UO_2 [9] and USb [6, 7], and anticipate from the previous experiments on IN22 at the ILL that, despite the size of the crystal, the signal is weak when full polarization analysis is needed. In order to resolve any small broadening, particularly below T*, a reference measurement of vanadium would also be made (note that the due to the large sample mass and associated extinction effects, the structural peaks are unsuitable to calibrate the resolution).

After consultation with Dr. A. Schneidewind, we request 8 days of beam time on PANDA to complete this study. This includes: 1 day setup, 5 days to measure energy scans at three points in reciprocal space across seven different temperatures (40 – 200K) and 2 days for unpolarised measurements at Q=[001]. We will work in fixed k_f mode at 1.5 $Å^{-1}$ with a Be filter and use the standard Heusler-Heusler monochromator-analyser configuration.

References

[1] M. Hagen, W. G. Stirling and G. H. Lander, Phys. Rev. B **37**, 1846 (1988)
[2] J. Jensen et al., Phys. Rev. B **23**, 6180 (1981)
[3] A. Ochiai et al., Physica B: Cond. Matt. **199**, 616 (1994)
[4] H. W. Knott et al., Phys. Rev. B **21**, 4159 (1980)
[5] L. Asch et al., Hyperfine Interactions **85**, 193 (1994)
[6] J. A. Lim et al., ILL expt. report 4-01-991 (2011) and J. A. Lim et al, submitted to Phys. Rev. B (2013)
[7] N. Magnani et al., J. Phys.: Condens. Matter **22**, 116002 (2010)
[8] G. H. Lander et al., Phys. Rev. Lett. **40**, 523 (1978)
[9] E. Blackburn et al., Phys. Rev. B **72**, 184411 (2005)

Chapter 4

XPCS measurements on uranium antimonide

4.1 Introduction & aims

Dynamics can occur across a range of timescales: from femtoseconds in molecular vibrations states [1], to kiloseconds for domain wall motion [25], however measuring this requires a probe with time resolution to match. In magnetic systems, inelastic neutron scattering and neutron spin echo are often the probes of choice; however they have upper bounds limited to nanosecond and microsecond timescales, respectively [131, 145, 180].

X-ray photon correlation spectroscopy (XPCS) (also known as speckle spectroscopy) uses X-rays to take snapshots and correlate processes occurring on Angstrom length-scales, from microseconds to kiloseconds, and is a useful probe to capture dynamics across a range of timescales [133, 167, 171].

In the previous chapter, we have seen that partial phase correlations remain way above the Néel temperature in USb and also an unexpected contribution to one of the polarisation channels. An explanation for this may be local regions within the sample

where the nominal phase relationships remain, leading to local *phase* domains (see Section 3.6.1).

The aims of this study were to use magnetic X-ray photon correlation spectroscopy to look for magnetic domain fluctuations in the 3-**k** magnet USb. In a macroscopically ordered sample, it is highly likely that these magnetic domains are present, although little is known about their spatial extent of these domains or the timescales over which the domains change. For reasons discussed later the dynamics are expected to be slow and the study of 3-**k** domains should be well suited to the XPCS technique, which has a broad dynamic range and should also be sensitive to change in the magnetic domains. In particular, it is of interest to see how the magnetic domains change near T_N and also T^*.

4.2 Magnetic domains in a 3-k magnet

In a macroscopically ordered sample, it is highly likely that spatial magnetic domains are present. Often, these arise from a need to minimise the magnetostatic energy (as is the case for ferromagnets) or due to sample morphology/defects (antiferromagnets).

Neighbouring domains are separated by a domain wall that incurs some additional exchange energy cost, which is balanced against the magnetocrystalline anisotropy of the system and any magnetoelastic energy.

There are many possible configurations for a domain wall in a 3-**k** magnet. Local regions around a straight domain wall are illustrated in figure 4.1. In the first case, the crystal has a single magnetic 3-**k** domain (grey boxes are guides to eye showing similar spin configurations: all pointing either in/out of a tetrahedra). In the other two cases the domain wall is created by changing the spins in the fourth column, which results in a domain wall between spins in column three and four (highlighted in green).

In the centre panel of figure 4.1, the spins in the fourth column have been flipped

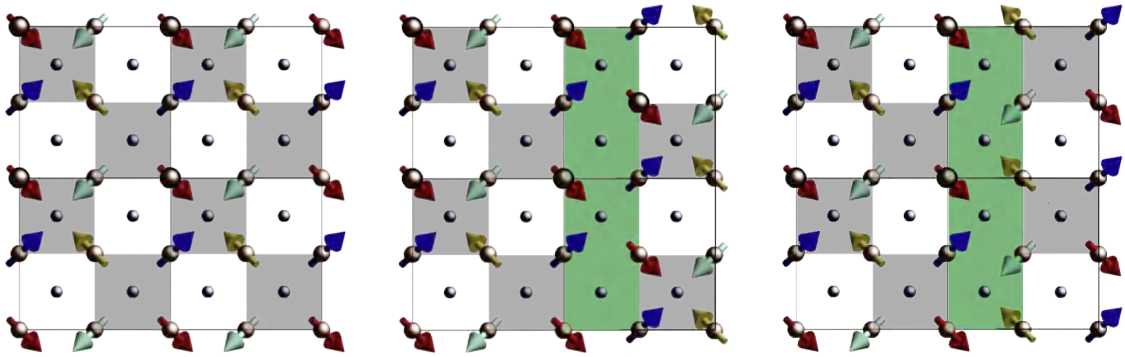

Figure 4.1: Possible domain spatial magnetic domain configurations in a 3-**k** magnet (adapted from [126]). Left: a longitudinal 3-**k** mono-domain. Centre: a canted ferromagnetic domain wall with net moment to the right. Right: an antiferromagnetic domain wall, but with transverse 3-**k** coupling across the wall. The grey boxes highlight tetrahedra with spins pointing all in or out.

relative to the monodomain configuration (a common approach to making domains in an antiferromagnet). The fifth column of spins is generated by continuing this tiling from the previous column. This results now in two domains that are separated by a canted ferromagnetic domain wall (in this case with net moment to the right).

In the right panel of figure 4.1, the spins in the fourth column have again been altered, but this results in no net magnetisation for the domain wall. If one looks along either side of the domain wall we note that there is regular longitudinal 3-**k** coupling similar to the bulk. However, looking across the domain wall, we find the transverse 3-**k** structure (recall figure 3.2 on page 45).

In both of these cases, the local cubic symmetry is broken by the domain wall as a preferred axis is chosen. One expects this to be important for USb as the local cubic symmetry is necessary for, and preserved by, the 3-**k** state. For this reason, and due to exchange energy costs, the domain wall is expected to be relatively slow (compared to other antiferromagnets, say), although little is known about domain dynamics in a multi-**k** system.

One should note that this is not a consideration for 1-**k** antiferromagnets, as the cubic symmetry has already been broken [113]. This difference, in part, motivates this thesis work as domain dynamics have been studied for 1-**k**, but not 3-**k** magnets [25, 26, 90, 167, 187].

In addition to the configurations discussed here, there are other possible domain walls one could consider and the simple cubic symmetry is broken there too. Note, that these illustrations are simple 2D projections and so the domain wall, rather than being a simple 1D object, is a 2D plane of spins which results in many different domain wall possibilities.

The other aim of this study is to explore the effect T_N and T^* have on the domain configurations and dynamics. At T_N, one expects a break-up in the domains and faster dynamics as the sample turns paramagnetic. It would be interesting to realise whether there are similar changes around T^*, which is associated with a softening of the spin wave modes but shows no change in the structural symmetry or magnetic order.

To explore the domains and their dynamics, a probe is needed that is sensitive to this order and also matches the relevant timescales - this prompts a discussion of X-ray photon correlation spectroscopy.

4.3 X-ray photon correlation spectroscopy

X-ray photon correlation spectroscopy (XPCS) has been able to probe structural dynamics (for example, diffusion in colloidal systems) from microseconds to kiloseconds [133, 171]. Recently, this technique has been applied to the study of antiferromagnetic domain motion.

In contrast to microscopy techniques, which are often surface sensitive (such as photoelectron emission microscopy (PEEM) [98, 137, 141, 190] and transmission X-ray microscopy [46, 49, 89]), X-ray photon correlation spectroscopy is a bulk probe

that captures an ensemble average of the domain properties. This is advantageous as the sample surface breaks the symmetry of the 3-**k** state which can lead to complex behaviour [10, 113]

A brief introduction to the XPCS technique will be presented, highlighting the suitability of studying magnetic dynamics.

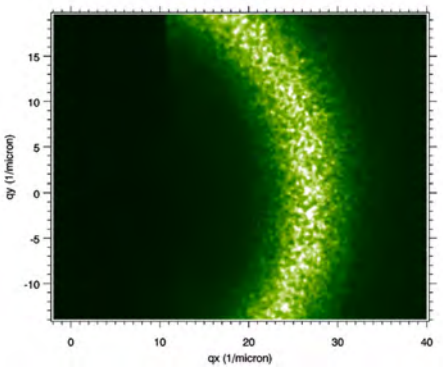

Figure 4.2: Speckle from magnetic stripe domains in a 350 Å film of $GdFe_2$ measured at the Gd M_5 resonance. Image from Ref. [63] attributed to [150]

4.3.1 Principle

If a sample is illuminated by coherent X-rays, then the diffracted beam will exhibit interference from the sample morphology and give rise to a spatially varying scattered intensity pattern: this is known as *speckle* (see figure 4.2). If the sample is undergoing thermal fluctuations, then this speckle pattern will vary as a function of time. Correlation spectroscopy looks at fluctuations in the speckle pattern, at time instants t' and $t' + t$ and compares them, giving useful information about the time evolution and dynamics of the system.

The measure of correlation in XPCS is the intensity-intensity autocorrelation function, $g_2(\mathbf{Q}, t)$, which is defined for wavevector, $\mathbf{Q}$ and time interval, t, as:

$$g_2(\mathbf{Q}, t) \equiv \frac{\langle I(\mathbf{Q}, t')I(\mathbf{Q}, t' + t)\rangle}{\langle I(\mathbf{Q}, t')\rangle^2}; \;\; t \geq 0 \tag{4.1}$$

where $I(\mathbf{Q}, t')$ is the intensity for a given wavevector at time t' and $\langle ... \rangle$ denotes a time average over time t'. For short time intervals, the speckle pattern does not change and in this limit, the numerator goes as $\langle I(\mathbf{Q}, t)^2 \rangle$. Considering the long time interval limit, the intensities in the numerator will be uncorrelated from one another so will tend towards $\langle I(\mathbf{Q}, t) \rangle^2$. The correlation function, $g_2(t)$, will therefore decay from a maximal initial value to a constant at long times (note that $\langle I(\mathbf{Q}, t)^2 \rangle > \langle I(\mathbf{Q}, t) \rangle^2$); and using the Siegert relationship [149] can be expressed as [125, 182]:

$$g_2(\mathbf{Q}, t) = 1 + A[f(\mathbf{Q}, t)]^2 \tag{4.2}$$

where A is defined as the speckle contrast (a sample independent, beamline parameter, determined experimentally) and $f(\mathbf{Q}, t)$ is the normalised intermediate scattering function linked to the dynamic structure factor, $S(\mathbf{Q}, t)$, by

$$f(\mathbf{Q}, t) = \frac{S(\mathbf{Q}, t)}{S(\mathbf{Q}, 0)} \tag{4.3}$$

A cartoon of the data acquisition procedure for a XPCS experiment is shown in figure 4.3. At a given temperature, a series of N speckle diffraction patterns are obtained on a CCD, spaced apart by a time interval, t (the finite time of exposure will be ignored for now). For a chosen region $\mathbf{Q} = \mathbf{Q}'$, $g_2(\mathbf{Q}', t)$ is calculated in the discrete limit of equation 4.1, which is given by:

$$g_2(\mathbf{Q}', t) = \frac{\frac{1}{N} \sum_{t'>0} I(\mathbf{Q}', t') I(\mathbf{Q}', t' + t)}{\langle I(\mathbf{Q}', t') \rangle^2} \tag{4.4}$$

If one considers a sample whose dynamics are governed by a process that follows a single exponential decay, then it will have the autocorrelation function:

$$g_2(t) = 1 + Ae^{-2\Gamma t} \tag{4.5}$$

where the relaxation rate of the process of the equilibrium fluctuations is governed by the relaxation constant, Γ. Jakeman [77] has shown that the effect of counting for a

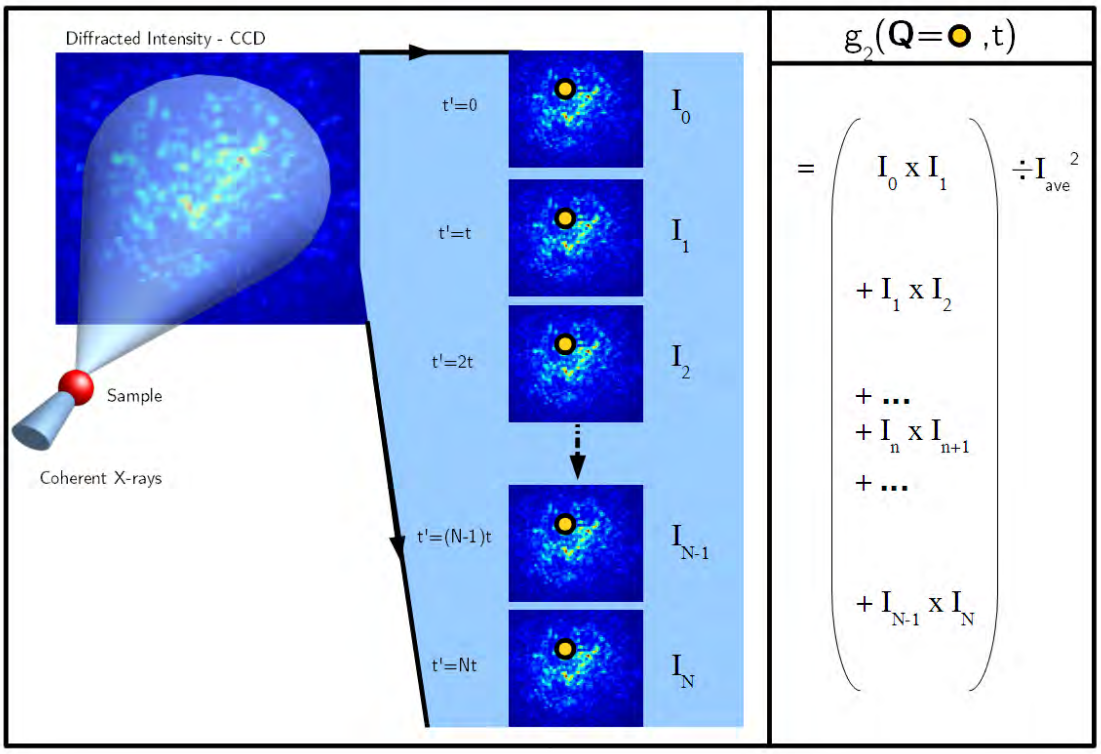

Figure 4.3: Speckle diffraction patterns are obtained for time steps, t, and then correlated using equation 4.4 to find $g_2(\mathbf{Q}, t)$. In the above example the yellow dot region is chosen for a particular $\mathbf{Q}$, however this is illustratory only; in practise an annular sector at constant $\mathbf{Q}$ about a Bragg reflection would be chosen.

finite time does not change the form of the auto-correlation function (in most cases) and leads to a decreased optical contrast: $A \rightarrow A'$ (where $A' < A$).

In a typical XPCS experiment, the aim is to calculate $g_2(\mathbf{Q}', t)$ over a particular detector region $\mathbf{Q}$', where dynamical processes are occurring and then to look at its form for a given temperature in order to extract a characteristic time scale(s). The next step would be to look at how the relaxation time varies with temperature.

The time window of an XPCS experiment is limited by finite count and detector read-out time mitigating the fast event resolution; and beam coherence and setup stability limiting the long time scale processes. Across all time regimes, photon intensity is critical to give meaningful statistics for a technique that requires a good signal to noise ratio.

Beam spatial-coherence is generated by a pinhole aperture, which massively reduces the incoming flux. It is due to bright synchrotron sources with a large number of coherent photons and fast CCD detector hardware that have made XPCS possible [125].

4.3.2 Previous XPCS studies

To date XPCS has been used successfully as a structural probe for colloidal systems and other problems in soft condensed matter [125, 171, 186]. These systems have characteristic length scales that are well matched by X-ray wavelengths and dynamics that can span many orders of magnitude.

Magnetic XPCS, however, is a field still in its infancy. A challenge facing the measurement of spin dynamics using XPCS is tuning the X-ray beam to be an effective probe at picking out the magnetic correlations, over and above any structural signal and other fluctuations that will be present.

In an antiferromagnet there exist domains and also domain fluctuations. Unlike ferromagnets, where these fluctuations in domains give rise to volume changes and

associated Barkhausen noise [189], detecting fluctuations in antiferromagnetic domains is more subtle: for antiferromagnets, mesoscopic probes have not proved useful as the net magnetisation vanishes on these length scales.

XPCS on the other hand provides a suitable tool to probe the magnetic domain configurations and their dynamics. The principle of generating a series of speckle patterns and then correlating them remains the same. In the magnetic case, the speckle is generated from interference between different magnetic domains (recall figure 4.1).

The first reported use of this technique was in the case of elemental chromium, an antiferromagnet. Here the magnetic domain dynamics were studied by measuring changes in the autocorrelation function of the charge density wave satellite, which encodes information about the spin density wave and associated magnetic domain dynamics [169]. The authors were able to extract $g_2(t)$ (see figure 4.4) and found that there were two components to the relaxation: a slow and fast relaxation linked to local and collective reorientation dynamics.

Other XPCS studies have probed antiferromagnetic domain fluctuations more directly by measuring magnetic Bragg reflections at resonant X-ray edges [25, 26, 90, 167, 187]. Tuning the X-rays to a resonant edge is necessary to maximise the scattered flux, boost signal to noise ratios and reliably extract $g_2(t)$ (the details of resonant magnetic X-ray scattering are covered briefly in the following section).

In particular, the recent work by Chen *et al.* uses resonant XPCS to look at the spiral antiferromagnetic state in dysprosium. Here, they fit the form of the relaxation to $F(t) = exp[-(t/\tau)^{\beta}]$, where the coefficient $\beta = 1.5$ gives evidence for *jamming* or glass-like domain dynamics. The idea here is that domain wall motion requires a cooperative reorientation of many spins. This behaviour is similar to the case of chromium and also a wide range of other systems from colloidal gels [28] to dense ferrofluids [153].

It would be interesting to realise whether this jamming behaviour is seen in the domain dynamics of USb; or if the relaxation occurs by another route, such as quantum

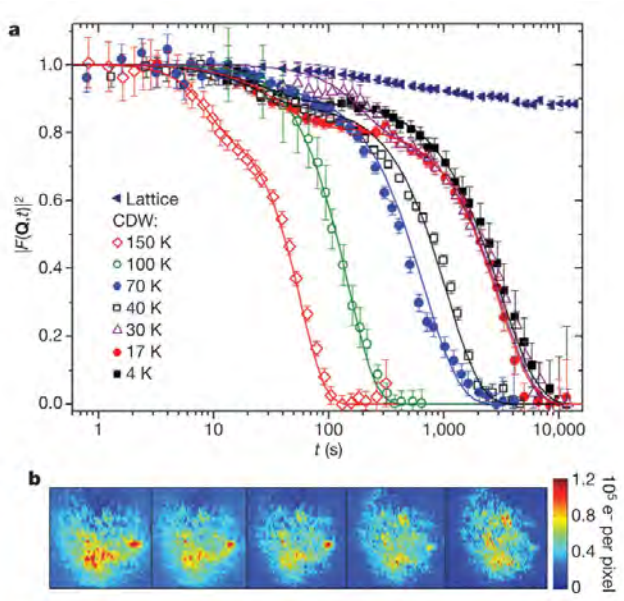

Figure 4.4: a) Upper panel: the correlation function *vs.* time for the charge density wave superlattice peak (2-2δ, 0, 0) at different temperatures. There are two characteristic timescales present in the relaxation, which are modelled by the solid curves. Also shown is the correlation function from the (2, 2, 0) structural Bragg peak and show little relaxation (which is due to the partially coherent beam) and is marked as "Lattice". b) lower panel: a time sequence of charge density wave speckle pattern evolution at 17 K, with subsequent images 1,000 s apart, which shows the gradual loss of correlation with increasing time. Figure from reference [169].

mechanical tunnelling [44, 169].

4.3.3 Magnetic X-ray scattering

So far it has been asserted that the X-rays are sensitive to magnetic order. This is to be expected to some extent, as X-rays are *electromagnetic* radiation and so are able to scatter from not only charge distributions, but also a magnetisation density. Some of the details behind magnetic and resonant magnetic X-ray scattering will now be presented.

Magnetic X-ray diffraction from an antiferromagnet was first demonstrated for NiO in the pioneering work of Bergevin and Brunel [36]. The tiny observed diffraction peak ($\approx$2 counts/min on a background of 15 counts/min) was visible below T_N due to selecting a structurally forbidden reflection where there is a magnetic superlattice lattice reflection only (the onset of magnetic order leads to doubling of the unit cell, allowing new reflections to be accessed).

This non-resonant magnetic scattering process comes from relativistic effects due to the coupling between the electromagnetic field with the spin and orbital components of the electron [11, 12]. This is a relatively weak effect; roughly 10^6 orders of magnitude smaller than Thompson scattering [18]. However, by tuning the incoming X-ray energy to excite a transition between electron states in an atom, this can lead to a large enhancement of the scattered intensity that can also be sensitive to the magnetism.

Resonant scattering occurs when an electron is excited from a core level to a higher unfilled atomic shell (or a narrow band) and then decays back to the original state (i.e. elastic scattering), releasing a photon. This process is described by second order perturbation theory and the transition probability between states (which is proportional

to the scattered intensity) is given by

$$W = \frac{2\pi}{\hbar} \left| \left\langle \psi_f \left| \hat{O} \right| \psi_i \right\rangle + \sum_n \frac{\left\langle \psi_f \left| \hat{O}^+ \right| \psi_n \right\rangle \left\langle \psi_n \left| \hat{O} \right| \psi_f \right\rangle}{E_g - E_n + \hbar\omega_i} \right|^2 \rho(E) \tag{4.6}$$

where the initial and final states are labelled by i and f, respectively, $\hat{O}$ is an operator describing the electron-photon interaction, E_g is the ground state energy, $\hbar\omega_i$ is the incoming photon energy, and ρ is the density of states [18]. At the resonant condition (i.e. $\hbar\omega = E_g - E_n$), the denominator in the second term will vanish, massively increasing the scattering rate.

This resonant scattering process samples the magnetism indirectly, with the strongest resonant enhancements to the scattering found at low-order *electric* multipole transitions ($E1$ or $E2$). Here it is the transitions to either the d- and f-levels, which are exchange split by the magnetism of the outer electrons, that gives rise to the magnetic sensitivity [18, 68].

Resonant magnetic X-ray scattering was first reported at the L_3 edge of holmium by Gibbs *et al.*, where the 50-fold increase in the magnetic diffracted intensity was used to study the spin spiral structure in elemental holmium [59]. Since then there have been many other resonant magnetic scattering studies, particularly ones looking at the $5f$ magnetism where there are huge resonant enhancements to be found [103, 104]. For the actinides, the relevant resonances are the M_4 and M_5 resonant edges that correspond to E1 transitions from $3d$ to the magnetic $5f$ orbitals.

The details behind magnetic, and particularly resonant magnetic, X-ray scattering are subtle; with the former a result of interaction between the electromagnetic field with spin and orbital magnetism, and the latter associated with transitions linked to magnetically exchange-split outer levels. The aims of this section were to provide a brief motivation behind the physics and to represent the flavour of X-ray magnetic scattering[1]. The key messages are that:

[1]For a more detailed and thorough approach, the reader should consult reference [12] and [11] and

- X-rays are sensitive to magnetism, either by non-resonant or resonant scattering, and the scattered intensity is typically weak.

- The magnetic signal can be separated from the intense charge scattering by selecting a forbidden structural reflection where only the magnetic signal is present.

- The magnetic scattering can be greatly enhanced by resonantly exciting a transition to exchange-split outer electron states.

There are many complicated and useful techniques associated with resonant magnetic X-ray scattering (such as spectroscopic and polarisation analysis [70]), but it should be emphasised in the context of this XPCS study, that the scattered intensity is used simply as a high resolution Bragg peak that is sensitive to the magnetic order of the sample.

4.3.4 Magnetic XPCS work carried out during this thesis

During this thesis work, I have used XPCS to study other magnetic systems. Although the physics are quite different to that of a 3-**k** magnet, the approaches and lessons developed were important in applying this technique to USb.

XPCS studies of the spin ice $Ho_2Ti_2O_7$

I have tried using XPCS to study spin dynamics in the magnetic frustrated spin ice $Ho_2Ti_2O_7$. In $Ho_2Ti_2O_7$, localised Ho spins sitting on a pyrochlore lattice point along local $\langle 1\ 1\ 1 \rangle$ directions, with two spins pointing to the centre of each local tetrahedra and two out. There is no unique ground state for this configuration and the system is highly frustrated. This *two in, two out* configuration for spins on a pyrochlore lattice

references therein.

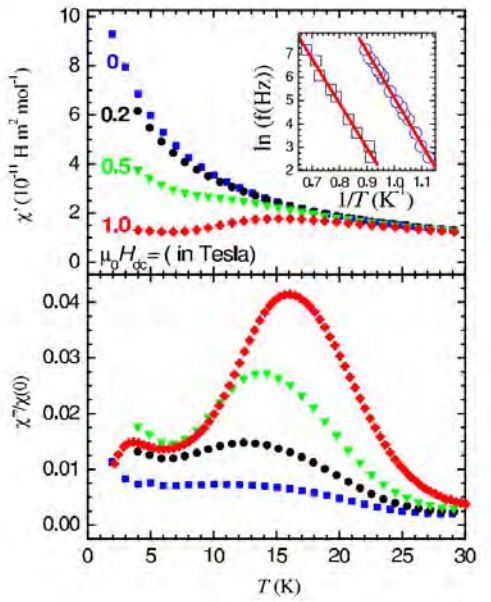

Figure 4.5: AC susceptibility measurements showing the real and imaginary parts of the AC magnetic susceptibility versus temperature for different applied fields in $Ho_2Ti_2O_7$ (from Ref. [45]). The effect of the field appears to slow down the low process allowing the high process to dominate. Inset: Arrhenius plot for the frequency shift of the low process peak for polycrystalline $Ho_2Ti_2O_7$ (□) and $Ho_{1.9}La_{0.1}Ti_2O_7$ (◯). This shows doping to slow down the low process.

directly maps onto the proton displacements due to hydrogen bonding in water ice - so $Ho_2Ti_2O_7$ is referred to as a *spin ice*[2].

As seen in Chapter 2, magnetic susceptibility measurements are a useful tool in realising the bulk response of a system. Figure 4.5 shows the AC magnetic susceptibility data for $Ho_2Ti_2O_7$, where two distinct features are noticeable as peaks in the imaginary part of the dynamic susceptibility, χ'' [44, 45]. The higher temperature process is seen in other $RE_2TM_2O_7$ (where RE is a rare earth element, e.g. Dy, Tb, Er and TM is either Ti or Sn) and is indicative of the material entering a glassy phase; the spins are

[2]An excellent introduction and review to the geometrically frustrated magnetic materials can be found in reference [58].

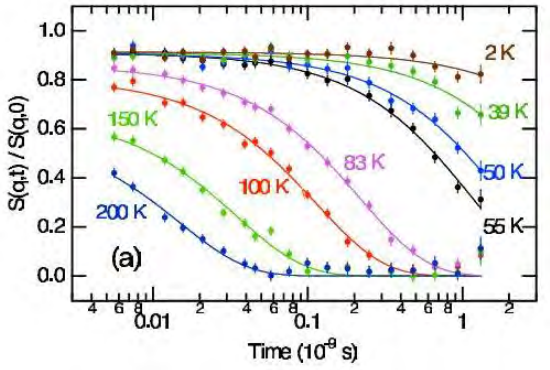

Figure 4.6: The normalised intermediate scattering function response as a function of time integrated over a range $0.5\text{Å}^{-1} \leqslant Q \leqslant 1.0\ \text{Å}^{-1}$ also showing fits for the relaxation time, $\tau(T)$ (from Ref. [45]). At low temperatures the exponential relaxation cannot be measured by neutron spin echo.

unable to follow the applied field as the dynamical response of the system is slowed [69, 127, 152, 176]. At lower temperatures, another feature is present in χ'' only when a field is applied. This behaviour is different from other rare earth titanates, where it is present even in the absence of field.

To study the slow microscopic dynamics of $Ho_2Ti_2O_7$ using neutrons, high energy resolution is needed which the neutron spin echo technique is able to provide. The experiment measures the intermediate scattering function $S(\mathbf{Q}, t)$, which unlike susceptibility measurements of the bulk, contains both temporal and *spatial* correlations. Indeed, Ehlers *et al.* found the suppressed high process of $Ho_2Ti_2O_7$ is also observable in the neutron spin echo data: by taking the Fourier transform of $S(\mathbf{Q}, t)$ and by Kramers-Kronig inversion, the real and imaginary parts of the AC susceptibility can be found [45].

The results for $S(\mathbf{Q}, t)$ across a given $\mathbf{Q}$ range are shown in figure 4.6 and can be fitted by a simple exponential decay using a parameter, $\tau(T)$, that characterises the relaxation rate for a given temperature which is similar to the bulk susceptibility measurement for relaxation. Measurements show $S(\mathbf{Q}, t)$ to be largely $\mathbf{Q}$ independent

at high temperature which reflects the likely origin of the process. This gives negligible evidence for two spin correlations and so the high process is likely to be a single spin flip mechanism, as expected.

Speculation into the origin of the low process is that a *cooperative* quantum tunnelling of spins is the dominant mechanism, with Ehlers *et al.* suggesting that the unusually strong dipolar field plays an important role in its origin [44]. However, it is clear from figure 4.6 that at these low temperatures, the process lies outside of the neutron spin echo time measurement window and as yet no microscopic measure of the spatial and temporal spin correlations exist for low temperatures.

The motivation of our research in this field was to use X-ray photon correlation spectroscopy to reveal the microscopic dynamics at the lowest possible temperatures, and hence the physics at the longest timescales where other probes fall short.

In order to pick out the magnetic signal, this study used X-rays tuned to the M-resonant edges of holmium (M_4 = 1394 eV, M_5 = 1351 eV) which provided an amplification of the magnetic signal [144]. Unlike the studies of antiferromagnetic domains where a magnetic Bragg reflection is often selected, this was not available for the frustrated spin ice which does not order.

Instead the plan was to measure close to the $\mathbf{Q} = 0$ position, where the magnetic signal would be boosted by the nearest neighbour ferromagnetic exchange interaction. This corresponds to grazing incidence scattering in reflection geometry and straight though scattering in transmission geometry.

The relatively large beam footprint in the grazing incidence scattering geometry was very susceptible to small motion of the sample, which made it impossible to correlate frames over the required timescales.

We also found that switching to transmission geometry also proved problematic, as it requires a thinned sample to be prepared (to minimise X-ray attenuation) which limits the signal from a process that is already signal-to-noise starved.

The stability in the transmission geometry was much improved, which could prove useful in other systems. In XPCS, the energy (and hence wavelength) is determined by the resonant energies meaning that often, the associated 2θ angle may not be easily accessible. In the case of low angle scattering, we have been able to prepare samples by focused ion beam milling and mechanical film polishing that can be used in this geometry (see Fig. 4.7).

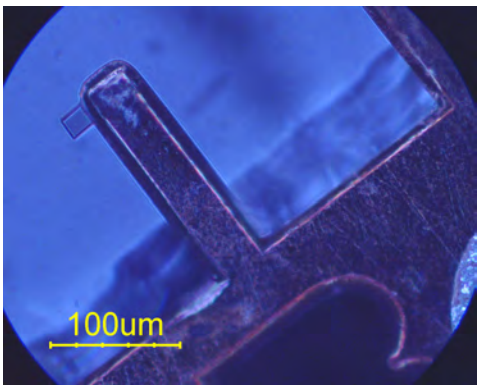

Figure 4.7: An optical microscope image of the focused ion beam milled prepared $Ho_2Ti_2O_7$ sample attached to a copper support grid for use in transmission geometry.

From this work, we were unable to clearly observe speckle and so unable to extract the autocorrelation function and characteristic relaxation of $Ho_2Ti_2O_7$. Systematic changes were observed in the scattering pattern when reversing the field which seem to coincide with temperatures where there are magnetic and electronic transitions - however, the data is not of high quality and is difficult to interpret (see appendix 4.A on page 135 for details).

XPCS studies of the magnetostrictive $Fe_{1-x}Ga_x$ alloys

$Fe_{1-x}Ga_x$ is a magnetostrictive material with a rich phase diagram as a function of doping, showing a number of different structures [85]. On cooling, there exists a metastable phase x between 0.15 and 0.27, which is made of a coexistence of the perfect solid so-

lution (the bcc A2 phase) and a Ga-rich $D0_3$ phase. However, the equilibrium phase at room temperature should be face centred cubic (the $L1_2$ phase). This transition from $D0_3$ to $L1_2$ occurs at room temperature and must pass through a tetragonal phase ($D0_{22}$). It is thought that a rotation through this intermediary tetragonal phase is induced by ferromagnetic interactions which may be key to generating the large structural change observed as a function of magnetic field [85].

Small angle neutron scattering has shown that in $Fe_{0.81}Ga_{0.19}$, there is a close link between the macroscopic magnetostriction and magnetisation in and around the nanoscale heterogeneities (the $D0_{22}$ precipitates) [114]. From this work it was anticipated that there are two different dynamical processes on the application of a magnetic field: magnetic domain wall motion and also the rotation of the tetragonal $D0_{22}$ precipitates to align the magnetic easy access of the tetragonal structure parallel to the field. Mechanical stress measurements, indicating loss due to magnetoelastic hysteresis of domain wall motion, show a resonance around 1 Hz [75].

The aim was to use XPCS to monitor the dynamic processes and changes as a function of magnetic field by studying the scattering at the Fe (L_{II} = 1143 eV) and Ga (L_{II} = 1116 eV, L_{III} = 707 eV) edges [185], as well as off resonance, to discern magnetic and structural information.

Speckle patterns were obtained at room temperature (for example, Fig. 4.8); however no dynamical speckle was observed on the timescales measured and the speckle pattern remained static. Due to the limited scattered intensity and slow read-out times, it was not possible to probe dynamics on timescales faster than 1 Hz.

Outcomes from XPCS work

These studies on $Ho_2Ti_2O_7$ and Fe-Ga system highlight some important lessons for magnetic XPCS:

- The setup must be stable over the timescales measured - without stability, the

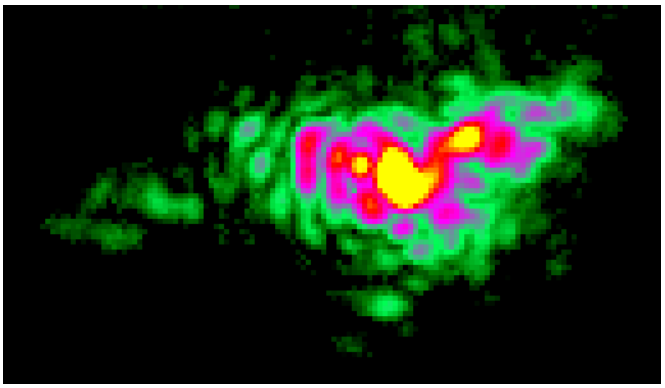

Figure 4.8: The magnetic speckle pattern obtained from a magnetic reflection in $Fe_{0.81}Ga_{0.19}$ at the resonant L_3 edge of Fe showing clear speckles arising from constructive and destructive interference.

optical contrast is hugely reduced and extraction of dynamics impossible.

- It is important to collect a large number of photons in order to be able to meaningfully measure the relaxation. In the case of the $Fe_{1-x}Ga_x$ system, the small flux limited the dynamical range we were able to probe.

4.4 Experimental setup

4.4.1 XPCS setup

XPCS measurements on USb were carried out on the I16 beamline at Diamond in the UK, which is optimised for high coherence and resonant hard X-ray measurements, so well suited for this study looking at the uranium M-edge. An overview of the beamline layout detailing focusing and monochromating elements is shown in figure 4.9.

The relevant resonant energies for the $Ho_2Ti_2O_7$ and $Fe_{1-x}Ga_x$ systems were both in the soft X-ray regime. In the case of uranium, the resonant energies lie in the hard X-ray range and so at much shorter wavelength. This means the angular spread of the scattered pattern will be much smaller. The key features of this setup are to extend the

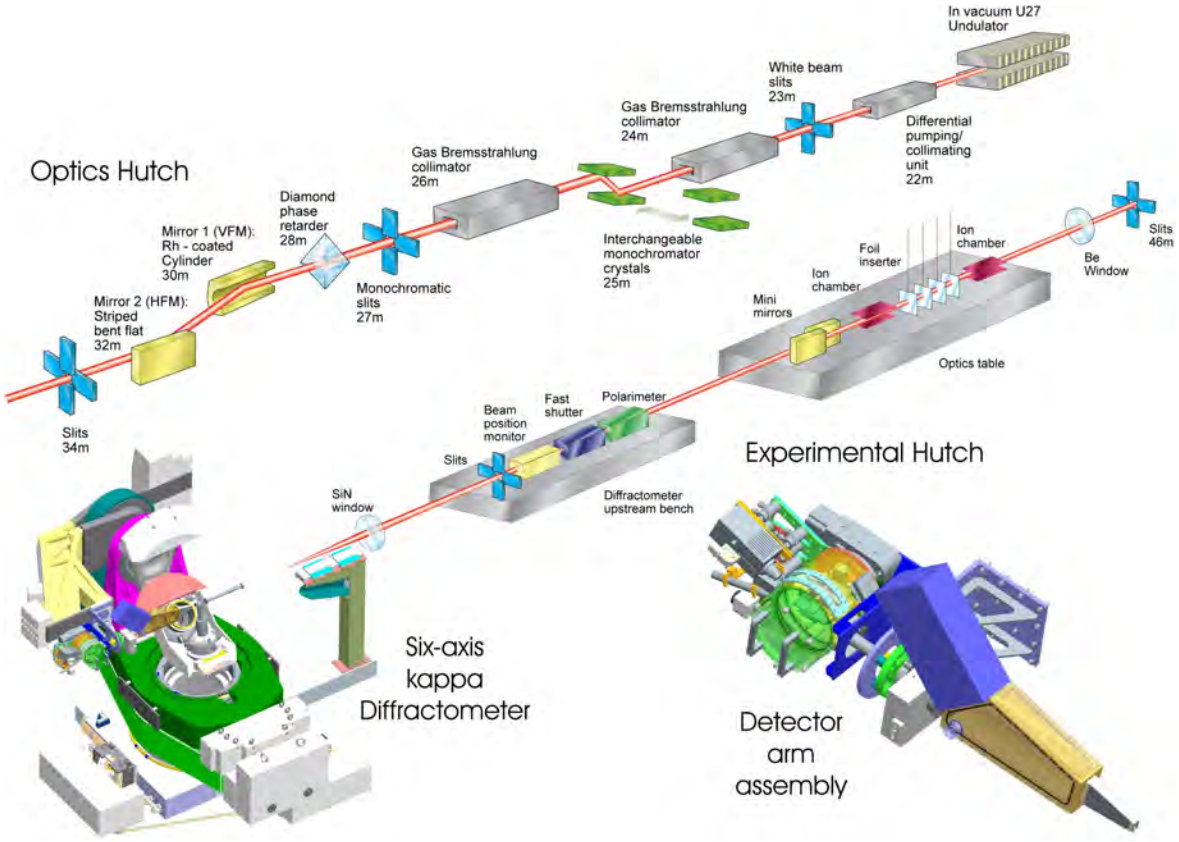

Figure 4.9: Overview of the optics layout on I16, Diamond (from [179]).

detector arm in order to obtain enough resolution on the detector to resolve the speckles that are needed for the correlation procedure. This is obtained by a ∼1 m evacuated PVC pipe with Kapton® windows (see figure 4.10) that allows the scattered X-rays to travel through to the detector with minimal losses and noise from air scattering. The detector to sample distance was 1.26 m.

The high beam coherence required is obtained by closing sample slits to ∼10 μm square (this could be optimised to maximise the number of photons whilst keeping high coherence), approximately 70 cm before the sample. Excellent beam stability and higher harmonic rejection was achieved with a set of slits 0.35 m upstream, acting as a secondary source, and additional mini-mirrors [7] (resulting in 0.1% of contamination from charge diffraction from higher harmonics at the $\mathbf{Q}$ = (0, 0, 3) position).

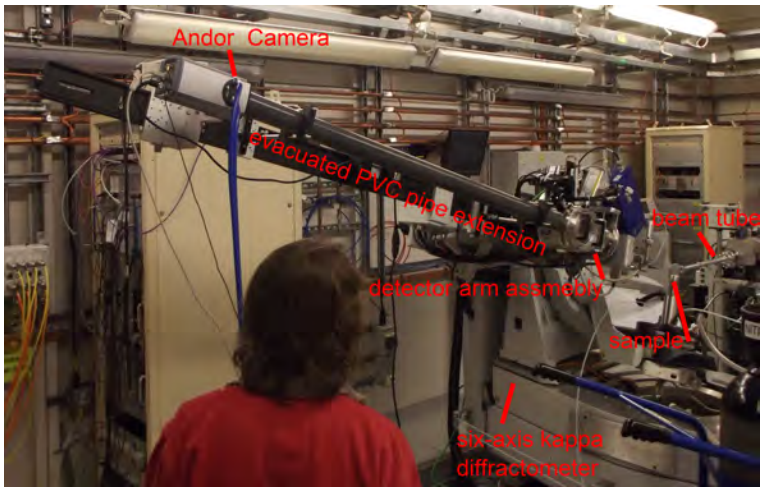

Figure 4.10: Picture of the detector setup on beamline I16 at Diamond. X-rays emerge from the beam tube, scatter from the sample and then into the detector arm assembly. The detector arm houses many different detectors and is also the mounting point for the extension. A black optics rail (visible below the pipe extension) supports the vacuum tube extension and the ANDOR® detector.

Reflections from the uranium M_4 edge (3.728 keV) provided a large enhancement of the magnetic scattering [184], enough to mitigate against the loss of intensity from a pinhole aperture. The feasibility of this approach has been demonstrated by preliminary studies on the isostructural compound UAs at the ESRF where, in similar conditions, up to 2000 cts/s from the $\mathbf{Q} = (0, 0, 1)$ reflection and static speckle was observable [193]. The scattering can be further enhanced by measuring at $\mathbf{Q} = (0, 0, 3)$ due to the greater 2θ angle, where there is a nine times intensity gain over $\mathbf{Q} = (0, 0, 1)$ [11]. Furthermore, the $\mathbf{Q} = (0, 0, 3)$ is a forbidden structural reflection for the face centred cubic lattice, meaning that the resulting speckle pattern is purely magnetic in origin and the resulting speckle pattern is due to the magnetic domains.

The energy resolution of the setup at the M_4 edge was 4.0 ± 0.2 eV at FWHM [10]. This corresponds to a longitudinal coherence length of $\sim 4\mu$m that is comparable to the maximum optical path difference (governed by the X-ray attenuation length and

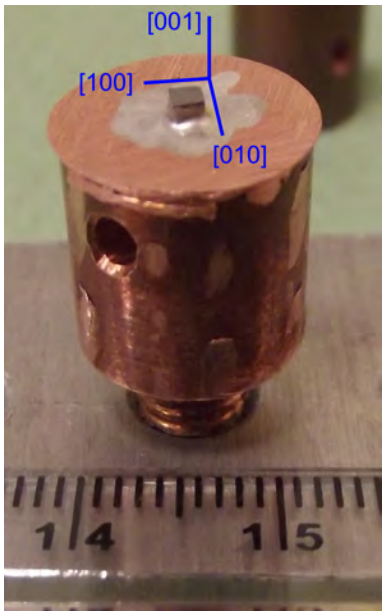

Figure 4.11: The mounted USb sample prior to loading into cryostat (with cm-scale ruler visible) with the underlying crystallographic axes illustrated.

scattering geometry).

The aim was to firstly confirm the presence of magnetic speckle and the suitability of I16 in this new setup. Once established, the next step was to look for slow dynamics ($\sim$1 Hz) by recording speckle patterns of the $\mathbf{Q}$ = (0, 0, 3) magnetic reflection on a CCD camera. As the timescales associated with the fluctuations were unknown, it was planned to search for faster dynamics ($\sim$kHz) using a MediPix detector, if the flux were large enough. However, it was found that during the experiment that the relatively low scattered X-ray flux would make it impossible to correlate processes occurring on such short timescales ($>$1 Hz). The detector used to capture snapshots of the speckle pattern was an ANDOR® iKon-M 934 (1024 x 1024 13 μm pixels), continuously cooled at -65°C.

Snapshots of the speckle pattern were then obtained across a range of temperatures, with exposure times of 1, 3 and 10 seconds. By correlating series of images at fixed temperature, it was possible to calculate the autocorrelation function to look for the

characteristic timescale of the magnetic fluctuations (this method is detailed in the next section 4.4.2). Speckle images were recorded 10 minutes after changing temperature; however, at least 1 hour was left for the setup to stabilise before the speckle patterns could be used for the correlation procedure, which was justified by checking that the values of $g_2(t)$ (at fixed delay time) versus acquisition time showed a random, and not a transient, response.

We aimed to measure at several different temperatures: from low temperature below T^* (where we expect slow domain dynamics) to above both T^* and T_N (where there are expected to be many domains). Close to the transitions and in the critical regime, we expected the dynamics to increase dramatically [25, 167, 169].

Several high quality crystals of USb for X-ray scattering were available. The chosen crystal had polished faces $\sim$2 mm^2 (see figure 4.11) and the most reflective was selected to be scattered from. The illuminated sample area is determined by the pinhole setup and the sample-beam angle (2θ). The sample was orientated with the [0, 0, 1] direction out of the sample surface and the [1, 0, 0] and [0, 1, 0] along the edges (due to the underlying rock-salt structure). The sample was mounted on a copper puck and with silver paint to ensure good thermal contact and sample stability.

Alignment to the magnetic reflections was carried out with a photodiode, which has high photon detection efficiency. Using a Dectris 100K-S Pilatus© detector, magnetic order parameter measurements [based on the magnetic $\mathbf{Q} = (0, 0, 3)$ diffracted intensity] were quickly obtained ($\sim$ 1 hour) by virtue of the area based detector. Note that whilst the Pilatus detector was more sensitive to X-rays than the ANDOR® CCD, the small pixel size of a CCD is needed to resolve the speckle patterns for XPCS.

4.4.2 Data analysis methods

The data was imported and analysed in MATLAB®. Whilst the detailed calculations of $g_2(\mathbf{Q}, t)$ would have been faster in other programming environments (e.g. Python,

C++, etc.), this was offset by MATLAB's support to load a range of different data types which enabled rapid prototyping and importantly displaying the processed data - this was extremely useful for *on-the-fly* analysis during the experiments. Details about the analysis program can be found in appendix 4.D.

The correlation function, $g_2(\mathbf{Q}, t)$, was calculated in the discrete limit using the formula in equation 4.4.

To improve statistics, the whole speckle pattern was used for the correlation, rather than dividing into individual ΔQ bins. This approach was shown to be justified for the data (in the following section) and also supports the findings in other magnetic XPCS studies that the dynamics are not ΔQ dependent [25, 167, 169] (although this may be due to the relatively low scattered intensities and limitations of the scattering geometry [25]). The results were independent of choosing overly large regions for analysis, due to a thresholding procedure (detailed in appendix 4.B) that meant pixels with low counts did not increase the background [125].

It was found that looking at the distribution of $g_2(t)$ values for a given delay time, t, there was a notable distribution in values, highlighting the need to use as much available data as possible. Furthermore, by checking a series of $g_2(t)$ at a fixed delay against acquisition time, transient responses could be identified and only speckle patterns after this settling were used. To avoid correlated errors, each frame was used only once in the calculation procedure.

It will be shown in section 4.6, that the response of $g_2(t)$ is largely static. In order to attempt to extract a small dynamical response on top of the large static magnetic signal, an alternative correlation procedure was used that subtracts a modelled static response (this is detailed in appendix 4.C). This analysis presented other problems and is not presented here, although it largely supports the dynamical picture put forward in the following sections.

Parallel analysis was carried out by F. Livet, using a droplet algorithm [15, 120] to

count photons and also calculate the intensity autocorrelation. The principle behind this is that a single X-ray photon generates a distribution of charges in neighbouring pixels on a CCD. By looking over the whole CCD and using a statistical process to model each of these impacts as a droplets, individual photon counting can be achieved with low background and sub-pixel resolution. In the limit of low noise and large intensity this gives the same result as other methods.

4.5 Results

The sample was rocked through the Bragg condition at the $\mathbf{Q} = (0, 0, 3)$ position. The intensity was integrated over this rocking curve using a Voigt function, which forms a measure of the order parameter and fits the data well. The order parameter as a function of temperature can then be extracted and is shown in figure 4.12.

The integrated intensity near the transition was fitted with a general order parameter function (see Eqn. 3.51); and the critical exponent, $\beta = 0.33 \pm 0.05$ and Néel temperature, $T_N = 218 \pm 1$ K were extracted. These results were in close agreement with the neutron data and published values [87, 111, 118, 139].

Bragg diffraction from rastering around the sample surface showed an alpine-like structure to the diffracted intensity at a single Bragg condition (see Fig. 4.13), despite the polished smooth surface. This is typical of the rock-salt structure of USb that contains many grain boundaries, dislocations and other defects. Regardless of the beam position, the sample showed an average mosaic width of 0.08° at full width half maximum.

Using the ANDOR® camera setup, as described in Section 4.4.1, series of speckle patterns were obtained at fixed temperatures. The obtained speckle patterns showed clear and well defined speckles - a typical magnetic speckle pattern is shown in the top upper panel of figure 4.14.

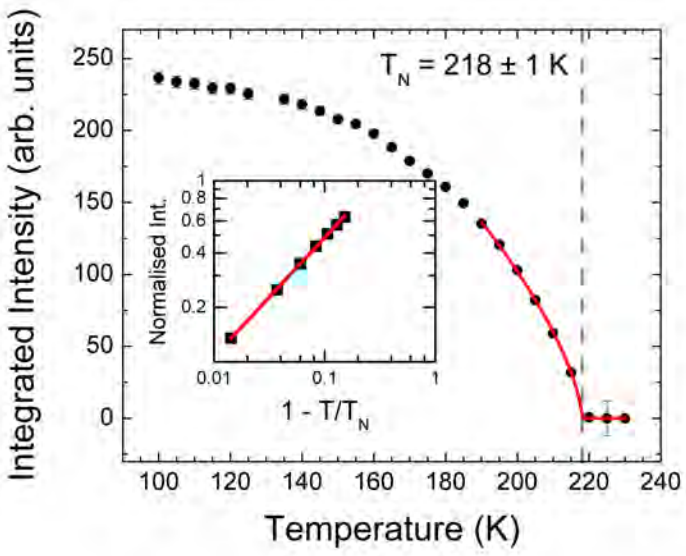

Figure 4.12: Integrated intensity of the $\mathbf{Q} = (0, 0, 3)$ reflection as a function of temperature, which forms a measure of the magnetic order parameter. The solid points are shown with errorbars, and the solid red curve is a fit to the data as described in the text. The error bars are based on the fit errors on the integrated intensity. Inset: log-log plot of the $\mathbf{Q} = (0, 0, 3)$ integrated intensity against reduced temperature.

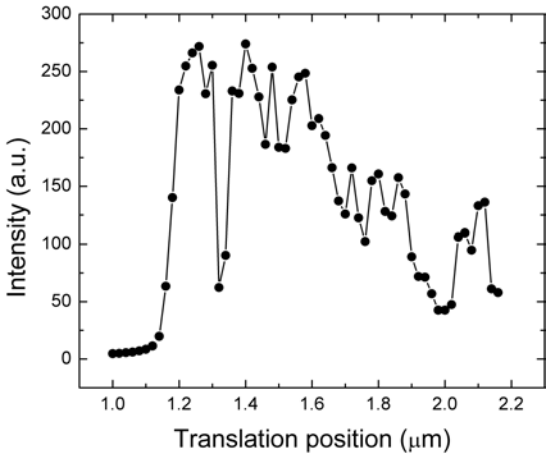

Figure 4.13: Translational scan of the sample surface at fixed θ and 2θ, showing the intensity from the $\mathbf{Q} = (0, 0, 3)$ reflection.

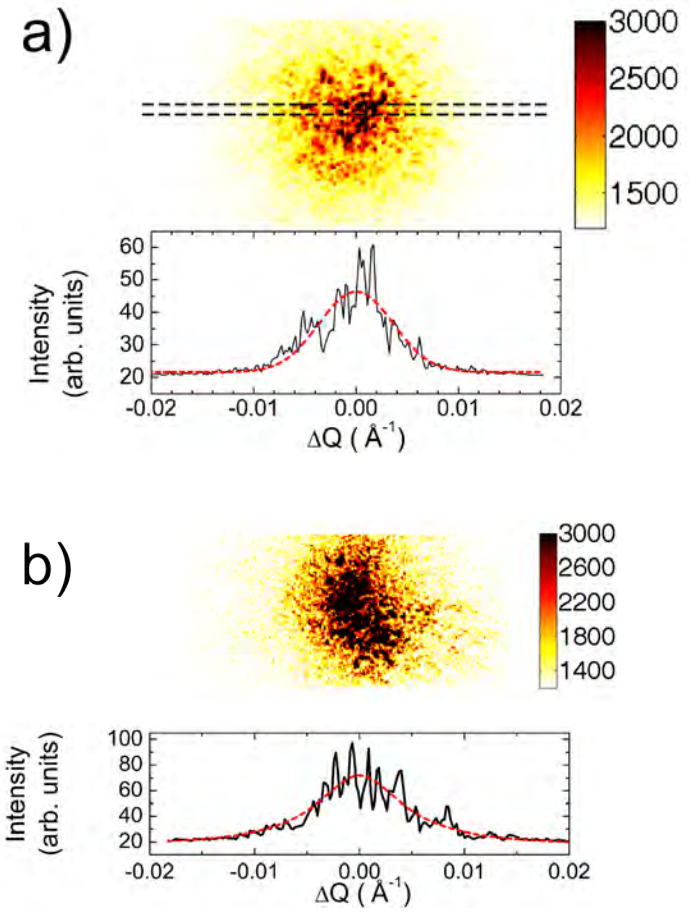

Figure 4.14: Upper halves: Typical speckle pattern obtained from the magnetic $\mathbf{Q}$ = (0, 0, 3) and structural $\mathbf{Q}$ = (0, 0, 2) reflection at the M_4 resonant edge of uranium (a and b, respectively). The exposure time was 1 s and 25 x 25 μm or 10 x 10 μm slits were used for the structural and magnetic patterns, respectively. The black dashed lines show the region for the intensity profile in each lower panel. Lower halves: The intensity profile (solid line) of a slice through the speckle pattern showing intensity fluctuations that arise from the beam coherence. The red curve (Gaussian) shows the expected non-coherent intensity profile.

The top lower panel of figure 4.14 shows a intensity slice through the magnetic speckle pattern at 150 K. The smooth curve (Gaussian) shows the expected diffracted intensity profile in the absence of coherent speckle. The large intensity deviations from this curve come from constructive and destructive interference indicating high coherence of the setup. The speckle pattern and profile for the charge peak, at 100 K, is shown in the lower half of figure 4.14.

4.6 Analysis & discussion

The spread of the static speckle pattern on the CCD gives information about the characteristic length scales of the domains. The central intensity profiles of the speckle patterns fit well to a Lorentzian lineshape, and the half width at half maximum, ΔQ, is then inversely related to the average domain size [193]. Figure 4.15 shows the results of this process, showing magnetic correlations on length scales on of 100 Å and above.

For comparison, the same method gives the size of structural domains to be 100 Å [as measured from the $\mathbf{Q} = (0, 0, 2)$ peak] indicating that the magnetic domain size is not limited by the structure. This feature was also observed in the 1-$\mathbf{k}$ magnet UAs [193]. This can be explained by strong magnetic interactions *healing* over small structural defects [71, 177].

Near T_N, there is a reduction in magnetic domain size, which is expected as the sample fragments into many smaller 3-$\mathbf{k}$ domains. Interestingly, this behaviour is also seen near T^*, which indicates there are changes to the domain configurations around this temperature.

The autocorrelation function, $g_2(t)$, was extracted using the procedure detailed in section 4.4.2 and appendix 4.B. The calculation of $g_2(t)$ for each temperature typically used 1000 frames (where available), which corresponds to a dynamic range from $\sim$1 second to 1 hour. Speckle patterns were measured from temperatures below T^* to

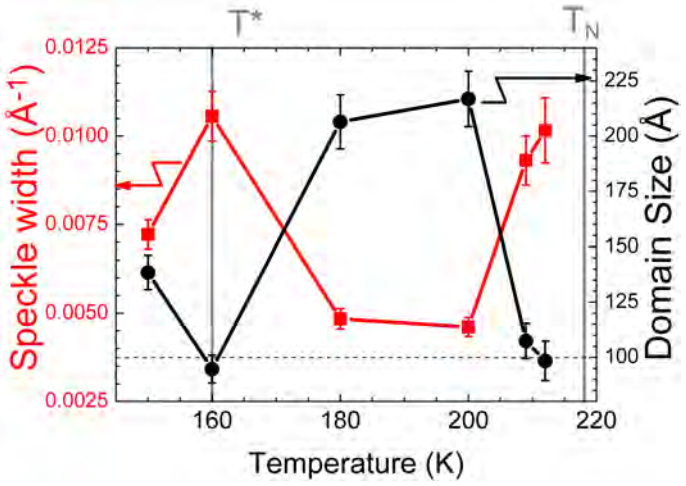

Figure 4.15: The extracted width of the magnetic speckle pattern and associated real space length as a function of temperature. The critical temperatures T^* and T_N are marked by the vertical lines. The dashed horizontal line denotes the average real space domain size based on the $\mathbf{Q} = (0, 0, 2)$ reflection, as measured at 100 K.

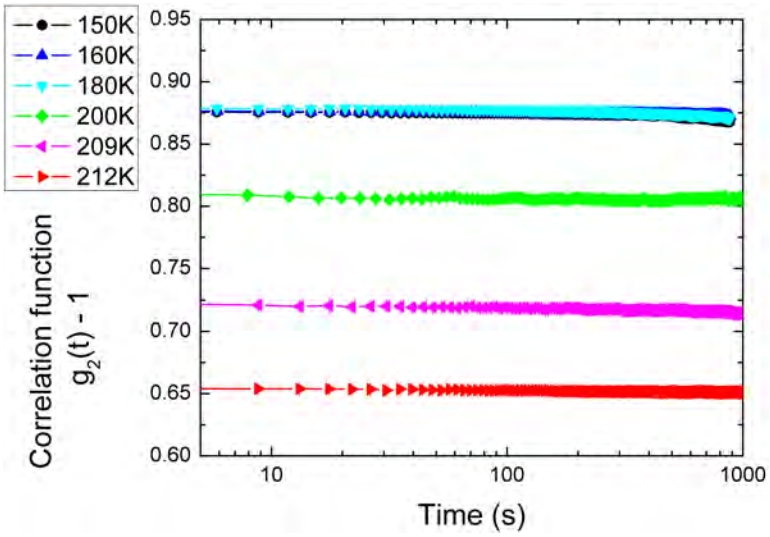

Figure 4.16: The calculated correlation function, $g_2(t)$, for different temperatures (error bars displayed) showing largely a static response.

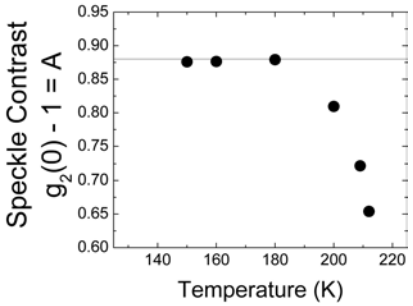

Figure 4.17: Magnetic speckle contrast as a function of temperature, which shows a maximum (the solid line) at $A = 0.88$.

right up to T_N. The results are shown in figure 4.16 and broadly show the correlation to not change with time. This apparent time independent result corresponds with the visual inspection of the speckles that appear to be static, reflecting the large static magnetisation of the 3-**k** state.

Complementary analysis by F. Livet, using a droplet algorithm [15, 120] to count photons, supports this analysis but is not presented here. In particular, there was no evidence for any ΔQ dependence to the results, validating the approach to integrate over many speckles and increase statistics.

A measure of the coherence contrast can be estimated to be equal to A [recall $g_2(t) = 1 + A[f(\mathbf{Q}, t)]^2$ (Eqn. 4.2)], which finds the contrast to decrease with decreasing flux as the temperature is raised (see figure 4.17). At low temperatures (< 180 K) this saturates at a maximum, $A = 0.88$. The contrast was found to decrease with the scattered flux [193], but does not follow the same scaling relationship as the order parameter, indicating that other factors are also at play. High contrast for the $\mathbf{Q} = (0, 0, 2)$ charge peak was measured ($A = 0.93$) due to the increased flux and reduced 10x10μm slits. Nonetheless, the constant response of $g_2(t)$ reflects the excellent stability of the setup on I16 and the high speckle contrast shows the suitability of this beamline for correlation spectroscopy over 100s of seconds.

Zooming in on the correlation function we see more detail and evidence for a small

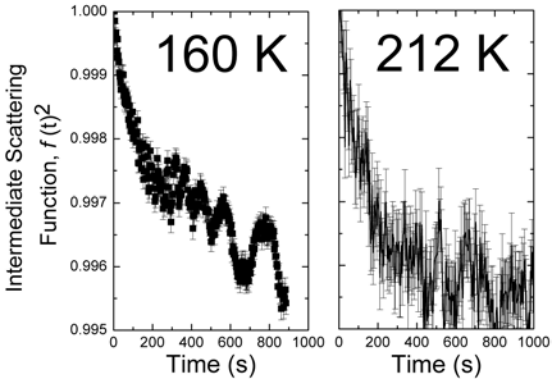

Figure 4.18: The normalised correlation response (the intermediate scattering function, $f(t)^2$), at temperatures near T^* and T_N zoomed in and showing the small decrease in correlation with increasing time.

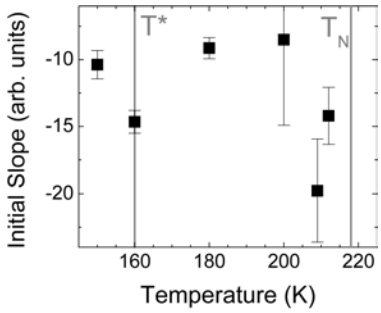

Figure 4.19: The initial linear gradient (first 100 s) of the intermediate scattering function against temperature (greater negative gradient corresponds to faster dynamics) showing faster dynamics near T^* and T_N (denoted by vertical lines).

relaxation on the order of 0.4% (figure 4.18). The full set of data can be found in appendix 4.E on page 148.

The oscillatory signal clearly visible at 160 K (and all other curves) is unlikely to be linked to the sample physics, but is possibly due to a property of the beamline setup. We are unable to rule out the occurrence of fast fluctuations that are outside the time interval probed by this technique.

It was not possible to fit the response for all the obtained curves (nor was it always possible to resolve the functional form [25, 167, 169]) due to the quality of the $g_2(t)$

data and the absence of a readily extractable background level. Instead, a proxy for the relaxation dynamics was estimated by looking at the initial linear slope over the first 100 s (figure 4.19).

This shows evidence for a faster dynamical response around T_N as expected, and also an increase in the rate of relaxation around T^*. This dynamical picture supports the static speckle information which gives evidence for a change in the domain configuration around T_N and also T^* (figure 4.15).

Using XPCS, we have observed a very slow response to domain motion, whilst the characteristic energies of the spin waves place the associated times in the gigahertz regime. For this reason, it is unlikely that the changes to the magnetic domains are driving the physics at T^* and the associated mode softening; rather it appears the decrease in magnetic domains size and increase in fluctuations is reflecting the spin wave mode softening. However, we note that our XPCS measurements are not sensitive to dynamics on timescales faster than 1 Hz, so continuation of the inelastic polarised neutron scattering experiments is important.

4.7 Conclusions & outlook

High quality speckle patterns were measured at the uranium M_4 resonant edge in bulk USb samples from the purely magnetic $\mathbf{Q}$ = (0, 0, 3) reflection, that showed high stability and an almost static response. The magnetic speckle contrast was found to be ~ 0.88 in the setup using a pinhole aperture of 25 x 25 μm and demonstrates the suitability of I16 in this setup for studying magnetic domain dynamics.

There are clear changes in the static and dynamical speckle patterns that show an increase in fluctuations and decrease in magnetic domain size around T_N and T^*. Additionally, these observations are entirely consistent with the idea of the soft magnon mode driving these domain changes around T^*. The cause behind the change of be-

haviour (which includes the magnon mode and other changes) around T^* remains unclear, although this work suggests that physics at T^* can not only be understood by changes in itinerancy [118].

These results are among the first XPCS measurements on a $5f$ electron system and this is one of the few studies to look at domains in a multi-**k** magnet[3]. This work shows the potential of the XPCS technique which combines coherent X-rays and resonant diffraction, for study of domain dynamics that is not otherwise accessible by other means. While there are distinct advantages to XPCS, to date there are still relatively few magnetic XPCS studies. This, as highlighted by the work in this thesis, is due to the necessity to match the physical timescales with the available coherent flux. In the case of USb the dynamics were not well aligned with the relevant timescales. However, useful static and dynamical domain information can be obtained, which widens the possibility for this fledgling technique.

[3]This XPCS work has been submitted for publication in the Journal of Physics: Conference Series.

Appendices:

XPCS investigations in USb

4.A Coherent X-ray studies on $Ho_2Ti_2O_7$

A brief summary will now be presented of the setup, results and analysis of the work on the spin ice, holmium titanate. The motivation and aims of this project are detailed in section 4.3.4 on page 113.

Setup

Resonant X-ray scattering from $\mathbf{Q} = (0, 0, 0)$ was studied, as this was expected to boost the magnetic intensity relative to the structural signal. The experiment was carried out in transmission geometry and the $Ho_2Ti_2O_7$ sample was appropriately thinned to allow the X-rays to pass through. The attenuation length of 1351 eV X-rays (the M_5 Ho resonant edge) in $Ho_2Ti_2O_7$ is 420 nm [51]. A single crystal sample of $Ho_2Ti_2O_7$ was thinned by focused ion beam milling to 400 nm thick and was roughly 10μm square.

The beamline layout is illustrated in figure 4.20. The main parameters to tune during the experiment were the undulator and monochromator energies, and also the focusing optics for maximising the X-ray flux on the sample. Not shown in the setup were pinholes of various sizes ($1\mu m - 10\mu m$) that could be positioned just before the sample (with *attocube*© piezo motors) to aperture the beam and improve beam coherence. The beam spot size at the sample is 10μm (FWHM) with coherent light.

Speckle patterns were recorded on an ANDOR® camera (2048x2048 CCD with an area of $\sim$2 cm) positioned 61 cm from the sample and collected intensity over a $\mathbf{Q}$ range 43 nm$< Q^{-1} <$ 300 nm at the resonant Ho M-edge.

The sample environment allowed control of field from -0.5 to 0.5 T and temperature from 20 to 330 K via a continuous flow cryostat operated by a needle valve. There was some evidence for drift in sample position as the temperature was changed that was hard to stabilise, which was problematic for the analysis and obtaining speckle patterns. Furthermore, as the pinhole and sample were comparable size to one another,

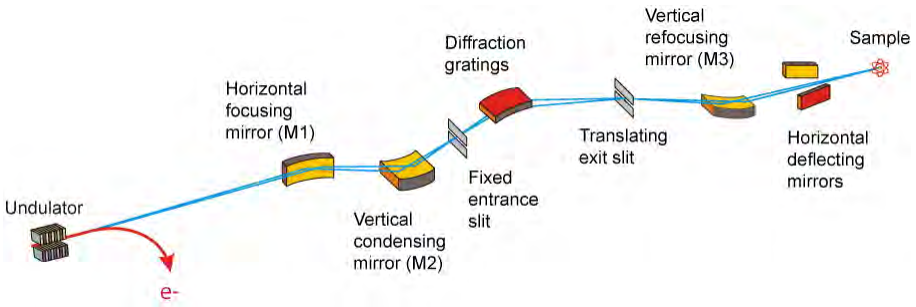

Figure 4.20: An illustration of the optics at the beamline that is used to collimate and preserve the beam brilliance at the ALS, whilst also setting the energy of the X-rays via the diffraction grating monochromator [3]. Not pictured is the pinhole and detector setup.

this exacerbated the drift problem and resulted in no observable speckle.

Results & analysis methods

The relative beam-sample drift and lack of speckle patterns makes XPCS impossible. However, the static systematics in the scattering were studied as a function of temperature. The idea was to look at *pairs* of images (chosen such that the drift between consecutive images is minimal) where the magnetic signature would change in some controlled way.

This was done by two methods: either flipping the magnetic field or detuning the energy from the holmium resonance. It was hoped that this would serve as a contrast mechanism and that by looking at systematic changes in consecutive images some useful static data could be extracted. In particular, it was of interest to see on what length scales correlations might develop.

The temperature was increased in steps and allowed to settle with approximately 20 images taken at each temperature (giving 19 contrast images) for both field and energy contrast methods. Before warming, the sample was either field cooled (FC) in 60 Oe or zero field cooled (ZFC).

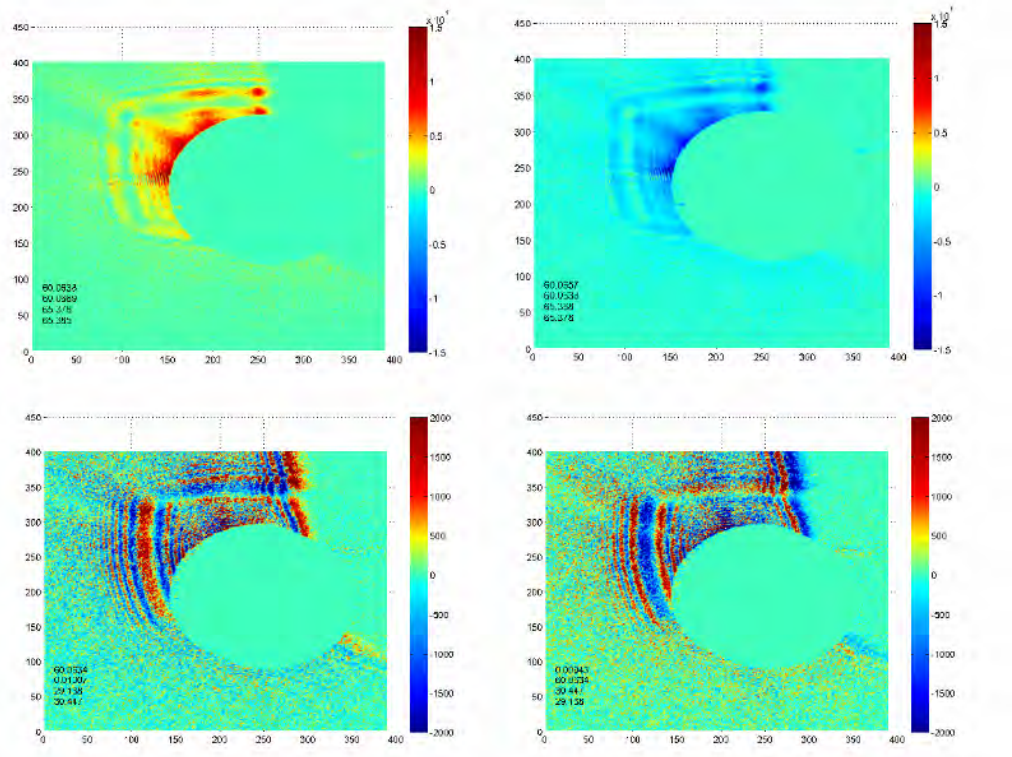

Figure 4.21: Analysed scattering patterns using the contrast method. The non-circular fringes arise from the small sample size and square shape. The support grid and beam stop are clearly visible as the places with zero intensity. Top: three consecutive captures make up two energy contrast images. Bottom: field contrast images showing the flip in the fringes as field is reversed.

To create these contrast images, either a magnetic field was applied that followed the series *[60, 0, -60, 0, ...]* Oe or alternatively the incident energy was switched from the Ho M_5 edge to 15 eV below the edge. The time to change the field or energy was on the order of a second, whilst the time for a single exposure was 15 s.

The files were read using an adapted MATLAB® script and several programs (written in MATLAB) were written to deal with the large number of images and study the systematics. The data analysis scheme comprised of subtracting the intensity of consecutive images, pixel by pixel to form a *contrast image* (figure 4.21 shows energy and field contrast images, showing systematic changes to the intensity when the energy or field was changed).

To quantify the contrast of each subtraction, the modulus of the each contrast image was taken and then summed over all pixels (in a given $\mathbf{Q}$ range): this value shall be referred to as the *energy* or *field contrast*, depending on the conditions of obtaining the images. Taking the sum of moduli of the contrast images avoids cancelling a negative difference from the subtraction process.

The non-circular fringes seen in figure 4.21 were moving, appearing/disappearing and varying in number from one image to the next. In general the definition of the fringes was not as clear as in figure 4.21. As it was problematic to find a reliable spot to focus on for data analysis, $\Delta\mathbf{Q}$ resolution was traded off to average over many fringes.

The temperature dependence of the contrast is shown in figure 4.22 for select $\mathbf{Q}$ regions. Across a broad range of scattering vector there is a characteristic hump around 48±2 K and 52±4 K for the ZFC and FC environments, respectively. The weak dependence of this feature on scattering vector is indicative of correlations occurring on many length scales: possibly an indication of glassy or frustrated behaviour.

The temperature of the peaks in contrast agree with the neutron spin echo data by Ehlers *et al.*, who found a change in the magnetic correlations at $\sim$ 55 K for *low* $\mathbf{Q}$, which they attributed to the onset of spatial correlations [44].

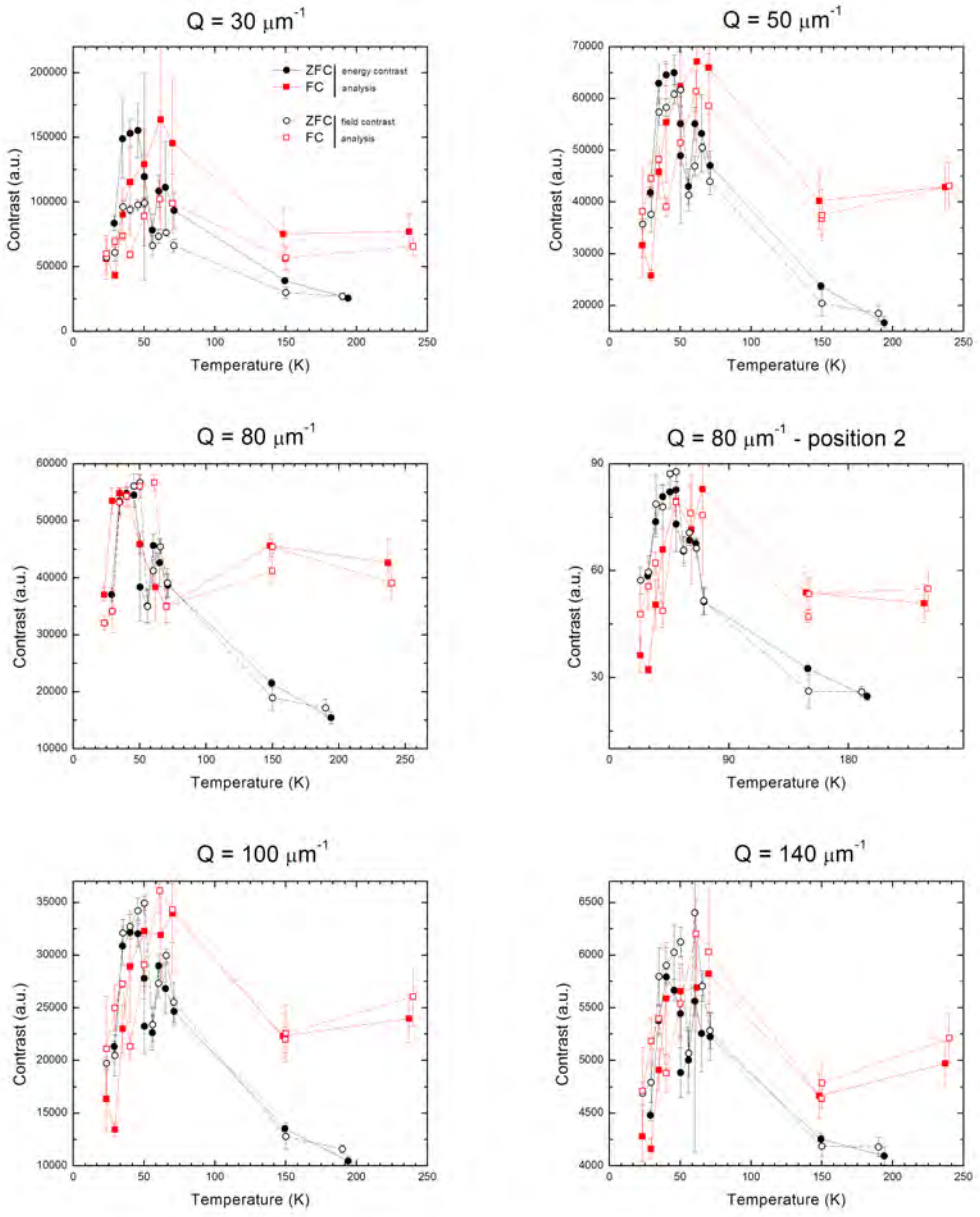

Figure 4.22: Contrast as function of temperature for different regions of **Q**. There is evidence for systematic differences between the FC and ZFC, but this remains largely **Q** independent.

There is some difference between the ZFC and FC behaviour, with the FC peak showing a change towards higher temperatures. The reason for this is unknown, but phenomenologically could arise from the FC state finding a more favourable spin arrangement that then persists to higher temperatures.

In Summary

XPCS measurements on $Ho_2Ti_2O_7$ were not possible due to beam-sample drift, but an alternative analysis scheme showed evidence for systematic static magnetic scattering from the sample. A peak in contrast was seen near temperatures where magnetic changes are known to occur.

There is some difference between ZFC and FC behaviour, with the FC showing a change in contrast towards higher temperatures. There is no microscopic explanation of this however, phenomenologically it may be understood by a favourable magnetisation state being created in the FC case which continues to higher temperatures.

4.B Pre-processing of images

This approach largely follows the procedure detailed by Lumma *et al.* [125].

When a speckle pattern is obtained, in addition to the coherent photons that are used for the auto-correlation, there will be unwanted noise. A large source of this comes from dark counts (i.e. when no X-ray are incident): approximately 1200 ADU, relative to 3000 ADU in the brightest speckles. It is found that there is significant dependence of the dark pattern across the CCD, whilst there are much smaller spatial changes in the standard deviation, σ_D.

To remove the dark count background, the dark counts are subtracted pixel-by-pixel from the recorded speckle pattern. If the difference is smaller than $4\sigma_D$, then the intensity is set to zero; otherwise the difference is left unaltered. This places a low end discrimination on the data to mask the dark noise.

When distinguishing small changes in autocorrelation (as is the case for USb), it is important to ensure that the appropriate normalisation is used. In addition to this thresholding procedure, it is important to list the pixels where the intensity has been set to zero and when cross-correlating set any corresponding pixels in the other frame to zero. This in effect forcibly removes some pixels from the correlation procedure and biases the correlation to be sensitive to high intensity speckles, rather than background fluctuations. The advantage of this is that this means the ΔQ averaged correlation is now largely independent of region size. It also avoids artificially increasing the intensity normalisation when no correlation exists and so losing sensitivity to fluctuations in the speckles.

4.C Alternative correlation calculation

In the case of apparent static speckle patterns, an alternative calculation was also made to pick out small dynamics on top of a large static background magnetisation. The principal idea is to subtract some average static signal, leaving only the fluctuations on top of this static background; and then correlate these fluctuations. An overview of this workflow is outlined in figure 4.23.

In order to subtract an appropriate "static background", the average intensity of temporally nearby frames was calculated. The number of frames to average over was varied: clearly if too few frames were taken then the result tends to zero; too many and the drift in sample setup becomes apparent. All the foreground frames were split into a fixed number of regions and the averages calculated within these regions. This sliding average approach means that frames at the extremes of the region had a sub-optimal average; but the drifts were very small meaning this could implemented to save computation effort without reducing the reliability of the average. The quantity after subtraction is referred to as $\Delta I_t(Q)$, where the subscript t denotes the time index of a particular frame.

The result from this subtraction would be approximately zero with some fluctuations remaining. The next step was to reject random fluctuations that are unrelated to the experiment. This noise filtering was done by looking at the size of the fluctuations, pixel by pixel, and setting it to zero if below a certain threshold - these pixels were also then excluded from the correlation procedure. This threshold was set as a multiple (typically 4) of the standard deviation of the dark noise, σ_D, obtained with no photons [125].

The output from the correlation procedure, referred to as $g_3(\mathbf{Q}, t)$, spans the range from $-1 < g_3(\mathbf{Q}, t) < 1$. Note, that it is not the sign of the $\Delta I_t(Q)$ that determines the sign of g_3, but rather the relative sign of pairs of pixels between frames.

"Subtract static background":	$\Delta I_t(Q) = I_t(Q) - \langle I(Q) \rangle$
	$\Delta I_t(Q) = \sim 0 \pm fluctuations$
	$\downarrow$
Filter:	if $\lvert fluctuations \rvert < N\sigma_D$
	set $fluctuations = 0$
	else
	$\Delta I_t(Q) = \pm fluctuations$
	$\downarrow$
Calculate correlation:	$g_3(Q,t) = \sum_{dt} \frac{\Delta I_t(Q) \Delta I_{t+dt}(Q)}{\sqrt{\langle \Delta I_t(Q) \rangle^2 \langle \Delta I_{t+dt}(Q) \rangle^2}}$
Output:	$g_3(Q,t) > 0 \Longrightarrow$ correlated
	$g_3(Q,t) = 0 \Longrightarrow$ uncorrelated
	$g_3(Q,t) < 0 \Longrightarrow$ anticorrelated

Figure 4.23: Schematic workflow for an alternative calculation of the correlation, $g_3(t)$. The aim of this method is to be more sensitive to any fluctuations that may be present on a large static background.

The interpretation of the $g_3(t)$ values is that if the fluctuations are correlated, then this will give a value greater than zero. If the values are randomly or uncorrelated, then g_3 will be zero. Alternatively negative values of g_3 imply that the system is anti-correlated: there is a flip in the sign of the fluctuation, ΔI_t from one frame to the next (relative to the average background).

It was found that adequately parametrising the average intensity was non-trivial and attempts to use local-time averages for the intensity produced additional artefacts in the correlation function, $g_3(t)$. It was possible, with some adjustment, to extract a dynamical response that was qualitatively similar to the calculated $g_2(t)$ values in the main text; however, it was decided to abandon this adaptive $g_3(t)$ approach in

favour of the looking at systematics in the $g_2(t)$ derived relaxation, which offers a more transparent interpretation.

4.D Matlab analysis program

From the Andor® camera, the data is saved as .tiff files and are loaded using the MATLAB built-in *imread* function. To carry out the autocorrelation procedure, there are two inputs the programs needs: the *Input* structure and *Settings* structures.

The *Input* structure contains information about the current data set; such as acquisition time, scan number, temperature, frames to correlate, region of interest and other information relating to the background subtraction.

The *Settings* structure contains information about what the program should run and parameters it should use (for example the colour bar scales, original data location, plot settings etc.). Whilst the *Input* structure will vary between different temperatures and different scan conditions, the *Settings* structure carries the settings that will be used to analyse a range of data.

The analysis can be run in batch mode from the MATLAB command prompt, however often it was useful to try different regions, background subtraction settings etc, and this was run using a simple GUI (see figure 4.24). The GUI would read and write data from the workspace so it is always available for batch scripting and saving.

Overview of GUI

The working of the main GUI options is detailed below.

Main window

- **Load Workspace** - based on the input name - this loads the corresponding MATLAB structure from the workspace.
- **Frames** - this specifies which frames should be loaded. It was found that after changing the temperature there was approximately a one hour transient that would disappear after this initial change (this was present for both structural and

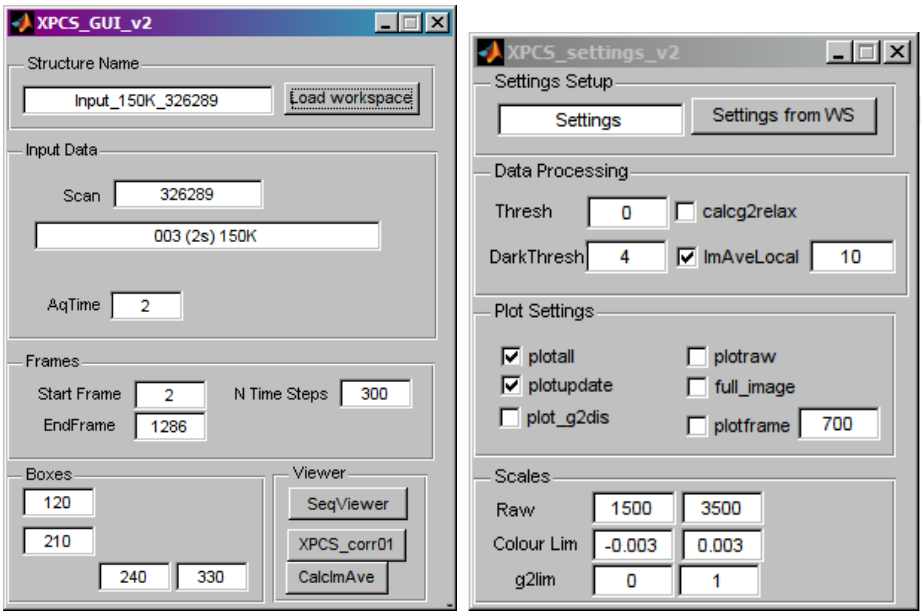

Figure 4.24: Screenshot of the MATLAB GUI to control data loading and execution of the autocorrelation calculation. Details about the calculation procedure are detailed in the main text.

magnetic peaks, so independent of the sample physics). Whilst the acquisition generally started after a delay, it is possible by specifying the frames to exclude these transient effects.

- **Boxes** - this allows a the region of interest box to be specified.
- **Viewer panel** - these buttons launch the program callbacks for running the correlation programs.

Settings window

- **Thresh** - this allows a constant noise floor to be subtracted from the raw data and was a simple means to treat the data during the experiment.
- **Dark Thresh** - this is a multiple of the standard deviation of intensity for the dark frames (i.e. electronic noise). Elements with fluctuations that are smaller

than $(DarkThresh) \times \sigma_{dark}$ from the average intensity are rejected and do not contribute to the calculation of the correlation function.

- **Calc g2 relax** if this option is checked, it correlates all the images relative to the first one (rather than summing together the pairs of similar correlation time). Often the sequence starts when there still may be transients present and by using this option, it is easy to identify when a transient response disappears.

- **ImAveLocal** - this parameter is set when calculating the alternative correlation method (see details in section 4.C). In addition to the fast transient response from changing temperature, there are slow random fluctuations/drifts in the speckle pattern that are not due to sample physics - this parameter specifies how many local bins to divide the data into for averaging, so it can then be subtracted.

- **Plot Settings** - this specifies which plots should be generated by during the program.

- **Scales** - this allows standard scales to be set on the colour bars and output plots to allow easy comparison between different fits.

4.E Overview of $g_2(t)$ data

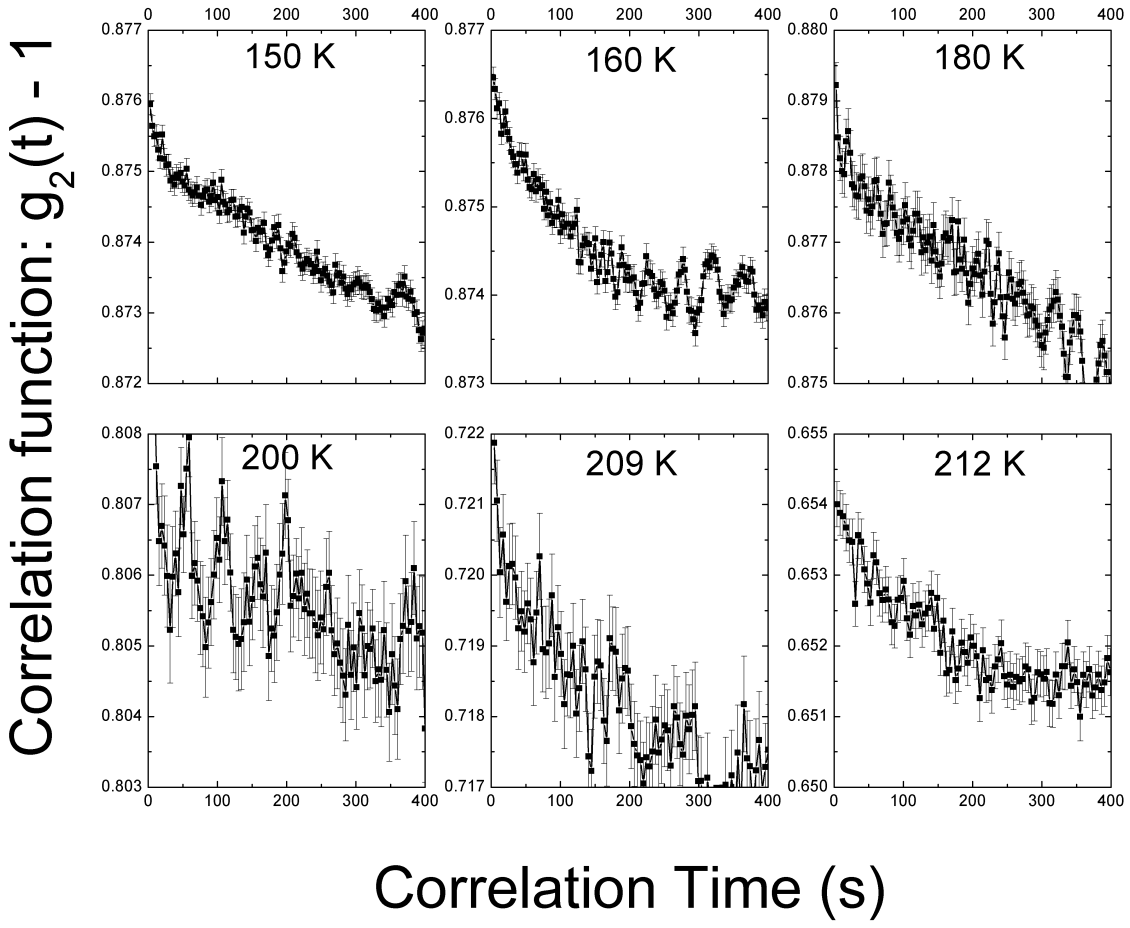

Figure 4.25: The calculated $g_2(t)$ values at different temperatures (plotted on a common y-axis span), showing an overall relaxation in addition to noise fluctuations.

Chapter 5

Conclusion & Perspectives

5.1 Characterisation of the possible dilute magnetic semiconductor, Cr-doped titanate

Single crystal $Cr_xTi_{2-x}O_2$ grown by float zone growth has been studied at a range of different dopings and characterised in terms of its structural and magnetic properties.

In contrast to previous findings [158], no evidence of ferromagnetism was found in the single crystal samples; however, small amounts of ferromagnetism were detected in the sintered powders. The presence of ferromagnetism in the Cr-doped TiO_2 system is attributed to defects, in agreement with other recent findings [92, 195]. This is an important result as it highlights the disparity between theoretical work and the thin-film prepared samples, whilst also providing a base-line for theoretical ideas. As no ferromagnetic component was measured, it is not possible to comment on the role of local versus itinerant magnetism in this system.

Looking forward, it is important to understand both experimentally and theoretically the variety of physics in these small samples. Whilst detailed calculations are important in understanding the properties, experimental characterisation of the im-

purities and physics at the interface will likely drive the development of this field, especially in finding novel and useful properties.

5.2 Studies of the 3-k magnet USb

The canonical 3-**k** magnet, USb has been studied using inelastic neutron scattering with tri-directional polarisation analysis. This has revealed that approaching the temperature, T^*, the softening of the spin waves is not due to de-phasing of the 3-**k** structure as was previously thought.

Instead, it is suggested that the softening of the spin waves is due to cross-over from local to more itinerant behaviour: a feature seen in other actinide compounds. A higher degree of itinerancy, could reduce the value of the magnetic moment, broaden the spin-wave transition and therefore also lower its energy range.

It was found that not only do the spin waves not de-phase, but remain phase-locked well above T_N. This leads us to propose phase domains (regions where quasielastic excitations preserve the low temperature 3-**k** phase information) which may also account for some of the behaviour around T^*.

This prompted an interest in magnetic domains in this system, which was studied using X-ray photon correlation spectroscopy (XPCS). Little was previously known about magnetic domains in a 3-**k** magnet and this is the first attempt at looking at this system with XPCS.

High quality speckle patterns were obtained from a magnetic reflection at the uranium M_4 edge. The domain evolution at all temperatures was found to be much slower than in other 1-**k** antiferromagnets: this was attributed to the breaking of the cubic symmetry required by the 3-**k** state.

It was found that there were structural and dynamic changes to the average domain configurations around T_N and interestingly, T^*. The reason behind the change in prop-

erties around T^* remains unclear; however, it is evident that the physics occurring at this temperature result in a break-up of magnetic domains, similar to the observations at T_N.

The change in physical properties at T^* in USb remains unexplained. In addition, to the softening of the spin wave mode, there are changes in the resistivity, lattice parameter and specific heat that have yet to be understood. Two possibilities have been put forward in this thesis: a change in itinerancy and evolution of phase domains. There are plans to test the latter hypothesis using polarised inelastic cold neutron scattering.

To understand changes in itinerancy, the theoretical work could be reformulated to include effects of temperature through change in the lattice parameter and the effect of excitations on the band structure. Alternatively, the experimental route could be taken and possibly use other techniques, such as angle resolved photoemission spectroscopy (ARPES) or resonant X-ray scattering, to study the Fermi surface and hybridisation of the $5f$ electron states as the temperature is changed.

Other work during thesis period

Interband Scattering in Superconducting $K_xFe_ySe_2$

The pairing symmetry in the recently discovered iron-based superconductors is not only important in understanding the mechanism behind superconductivity, but is also widely contested and poorly understood. I have conducted inelastic neutron scattering measurements at the ILL in France to search for interband scattering of electrons at particular momentum transfer vectors and energies. This resonance was observed and tracked through the superconducting phase and is thought to be important ingredient to superconductivity in the iron-selenides.

J. A. Lim, R. Morisaki, L. Lemberger, L.-P Regnault, E. M. Forgan, E. Blackburn, H. Kawano-Furukawa, *(submitted to the Journal of the Physical Society of Japan)*

Studies of the vortex lattice in superconductors

Vortex lattices in superconductors are an interesting state of matter in their own right and also can reveal important properties about the superconducting state. Also, doping a material is a well known method, especially in the cuprates, for applying "chemical pressure" to change the properties.

Using small angle neutron scattering to measure the vortex lattice, we have worked

on high quality samples of underdoped $YBa_2Cu_2O_{7-x}$ and have mapped out the vortex lattice structural phase diagram - this gives insight to non-local Fermi surface effects and vortex lattice transitions that are different from the optimally-doped parent compound.

N. Egetenmeyer, J. A. Lim, J. S. White, J. L. Gavilano, L. Lemberger, A. T. Holmes, E. M Forgan T. Loew, D. S. Inosov, V. Hinkov, M. Kenzelmann *(in preparation)*

Coupled magneto-structural transitions

In materials where structural and magnetic transitions are coupled, a number of interesting and useful phenomena are seen, such as the giant magnetocaloric effect and shape memory. I have studied epitaxial Ni_2MnGa films and $Ni_{50}Mn_{25+x}Sb_{25-x}$ using a variety of neutron techniques to try to reveal details of the magnetic structure and fluctuations.

In the case of Ni_2MnGa, polarised neutron reflectivity measurements were used to probe the depth dependent magnetisation (which is thought to be highly structured), however we were unable to resolve this due to the large film thicknesses. Recently, I have proposed using low energy muons as an alternative way to study this magnetic heterostructure and plan to carry out an depth-dependent implantation study later in 2013.

Dynamics of the liquid crystal *fd* virus in magnetic fields

Using small angle neutron scattering, we have studied the dynamical reorientation (Frederiks) transition across a range of different sample concentrations. Using 2D fit-

ting and modelling, we have successfully used small angle scattering to directly extract the elasticity constants (a novel result) and reveal differences between the wild-type and mutated strains.

This work, distinct from my projects in hard condensed matter, has challenged me to work in a new field as a part of an interdisciplinary team; which has helped improved my understanding of international collaboration, teamwork and project management.

J. A. Lim, A. T. Holmes, E. Mossou, E. Blackburn, V. T. Forsyth, E. M. Forgan, P. Lettinga *et al. (in preparation)*

List of Figures

List of Tables

References

[1] S. C. Abbi and S. A. Ahmad. *Nonlinear Optics and Laser Spectroscopy*. Alpha Science International, Limited, 2001.

[2] A. Abragam and B. Bleaney. Enhanced nuclear magnetism: some novel features and prospective experiments. *Proceedings of the Royal Society of London. A. Mathematical and Physical Sciences*, 387(1793):221–256, 1983.

[3] Advanced Light Source LBNL. Beamline 10.0.1 at the ALS. http://ssg.als.lbl.gov/ssgbeamlines/beamline10-0-1.

[4] P. W. Anderson. Antiferromagnetism. theory of superexchange interaction. *Phys. Rev.*, 79:350–356, Jul 1950.

[5] K. Andres, J. E. Graebner, and H. R. Ott. $4f$-virtual-bound-state formation in $CeAl_3$ at low temperatures. *Phys. Rev. Lett.*, 35:1779–1782, Dec 1975.

[6] V. N. Antonov, L. V. Bekenov, O. Jepsen, D. V. Mazur, and L. P. Germash. X-ray magnetic dichroism in the (Zn, Co)O diluted magnetic semiconductors from first principle calculations. *Journal of Applied Physics*, 111(7):073702, 2012.

[7] M. A. G. Aranda, F. Berenguer, R. J. Bean, X. Shi, G. Xiong, S. P. Collins, C. Nave, and I. K. Robinson. Coherent X-ray diffraction investigation of twinned microcrystals. *Journal of Synchrotron Radiation*, 17(6):751–760, Nov 2010.

[8] L. Asch, G. M. Kalvius, A. Kratzer, and F. J. Litterst. Phase de-locking in cubic 3-**k**-antiferromagnets. *Hyperfine Interactions*, 85:193–196, 1994.

[9] L. Balagurov, S. Klimonsky, S. Kobeleva, A. Orlov, N. Perov, and D. Yarkin. On the origin of ferromagnetism in semiconducting $TiO_{2-\delta}$:Co oxide. *JETP Letters*, 79:98–99, 2004.

[10] Z. Bao, R. Springell, H. C. Walker, G. Nisbet, S. Langridge, R. C. C. Ward, T. Gouder, R. Caciuffo, and G. H. Lander. Studies of antiferromagnetism in UO_2 thin epitaxial films. *Phys. Rev. B*, (012268), 2013. submitted.

[11] E. Beaurepaire, H. Bulou, F. Scheurer, and K. Jean-Paul, editors. *Magnetism: a synchrotron radiation approach.* Springer, 2006.

[12] E. Beaurepaire, H. Bulou, F. Scheurer, and K. Jean-Paul, editors. *Magnetism and synchrotron radiation - new trends.* Springer Proceedings in Physics, 2010.

[13] L. V. Bekenov, V. N. Antonov, S. Ostanin, A. N. Yaresko, I. V. Maznichenko, W. Hergert, I. Mertig, and A. Ernst. Electronic and magnetic properties of $(Zn_{1-x}V_x)O$ diluted magnetic semiconductors elucidated from X-ray magnetic circular dichroism at V $L_{2,3}$ edges and first-principles calculations. *Phys. Rev. B*, 84:134421, Oct 2011.

[14] N. Bernhoeft, A. Hiess, S. Langridge, A. Stunault, D. Wermeille, C. Vettier, G. H. Lander, M. Huth, M. Jourdan, and H. Adrian. Probe coherence volume and the interpretation of scattering experiments. *Phys. Rev. Lett.*, 81:3419–3422, Oct 1998.

[15] G. Beutier, G. van der Laan, A. Marty, and F. Livet. Back-illuminated CCD for coherent soft X-ray imaging. *The European Physical Journal Applied Physics*, 42:161–167, 4 2008.

[16] E. Blackburn, R. Caciuffo, N. Magnani, P. Santini, P. J. Brown, M. Enderle, and G. H. Lander. Spherical neutron spin polarimetry of anisotropic magnetic fluctuations in UO_2. *Phys. Rev. B*, 72:184411, Nov 2005.

[17] T. Bland, K. Lee, and S. Steinmüller. The spintronics challenge, physicsworld.com 2008.

[18] M. Blume. Magnetic scattering of X-rays (invited). *Journal of Applied Physics*, 57(8):3615–3618, 1985.

[19] S. Blundell. *Magnetism in Condensed Matter (Oxford Master Series in Condensed Matter Physics)*. OUP Oxford, 4 edition, 2001.

[20] B. N. Brockhouse. Scattering of neutrons by spin waves in magnetite. *Phys. Rev.*, 106:859–864, Jun 1957.

[21] J. D. Bryan, S. A. Santangelo, S. C. Keveren, and D. R. Gamelin. Activation of high-T_C ferromagnetism in Co^{2+}:TiO_2 and Cr^{3+}:TiO_2 nanorods and nanocrystals by grain boundary defects. *Journal of the American Chemical Society*, 127(44):15568–15574, 2005.

[22] R. Caciuffo, N. Magnani, P. Santini, S. Carretta, G. Amoretti, E. Blackburn, M. Enderle, P. J. Brown, and G. H. Lander. Anisotropic magnetic fluctuations in 3-**k** antiferromagnets. *Journal of Magnetism and Magnetic Materials*, 310(2, Part 2):1698 – 1702, 2007.

[23] A. Chakraborty, P. Wenk, R. Bouzerar, and G. Bouzerar. Spontaneous magnetization in the presence of nanoscale inhomogeneities in diluted magnetic systems. *Phys. Rev. B*, 86(21):214402, Dec. 2012.

[24] S. A. Chambers, C. M. Wang, S. Thevuthasan, T. Droubay, D. E. McCready, A. S. Lea, V. Shutthanandan, and C. F. W. Jr. Epitaxial growth and properties

of MBE-grown ferromagnetic Co-doped TiO_2 anatase films on $SrTiO_3(001)$ and $LaAlO_3(001)$. *Thin Solid Films*, 418(2):197 – 210, 2002.

[25] S.-W. Chen, H. Guo, K. A. Seu, K. Dumesnil, S. Roy, and S. K. Sinha. Jamming behavior of domains in a spiral antiferromagnetic system. *Phys. Rev. Lett.*, 110:217201, May 2013.

[26] K. Chesnel, M. Belakhovsky, G. van der Laan, F. Livet, A. Marty, G. Beutier, S. P. Collins, and A. Haznar. Tracking the local reversal processes in nanostructures by magnetic speckles. *Phys. Rev. B*, 70:180402, Nov 2004.

[27] N. J. Chesser and J. D. Axe. Derivation and experimental verification of the normalized resolution function for inelastic neutron scattering. *Acta Crystallographica Section A*, 29(2):160–169, Mar 1973.

[28] L. Cipelletti, L. Ramos, S. Manley, E. Pitard, D. A. Weitz, E. E. Pashkovski, and M. Johansson. Universal non-diffusive slow dynamics in aging soft matter. *Faraday Discuss.*, 123:237–251, 2003.

[29] W. Cochran. Crystal stability and the theory of ferroelectricity. *Phys. Rev. Lett.*, 3:412–414, Nov 1959.

[30] J. M. D. Coey. Dilute magnetic oxides. *Current Opinion in Solid State and Materials Science*, 10(2):83 – 92, 2006.

[31] J. M. D. Coey, M. Venkatesan, and C. B. Fitzgerald. Donor impurity band exchange in dilute ferromagnetic oxides. *Nature materials*, 4:173–179, 2005.

[32] M. J. Cooper and R. Nathans. The resolution function in neutron diffractometry. I. The resolution function of a neutron diffractometer and its application to phonon measurements. *Acta Crystallographica*, 23(3):357–367, Sep 1967.

[33] F. Da Pieve, S. Di Matteo, T. Rangel, M. Giantomassi, D. Lamoen, G.-M. Rignanese, and X. Gonze. Origin of Magnetism and Quasiparticles Properties in Cr-Doped TiO_2. *Physical Review Letters*, 110(13):136402, Mar. 2013.

[34] S. Das Sarma, E. H. Hwang, and A. Kaminski. Temperature-dependent magnetization in diluted magnetic semiconductors. *Phys. Rev. B*, 67:155201, Apr 2003.

[35] E. S. Dayhoff. Antiferromagnetic resonance in Cr_2O_3. *Phys. Rev.*, 107(1):84–91, Jul 1957.

[36] F. De Bergevin and M. Brunel. Observation of magnetic superlattice peaks by x-ray diffraction on an antiferromagnetic nio crystal. *Physics Letters A*, 39(2):141–142, 1972.

[37] A.-J. Dianoux and G. H. Lander, editors. *Neutron Data Booklet*. OCP Science, 2 edition, 2003.

[38] T. Dietl. Spintronics and ferromagnetism in wide-band-gap semiconductors. *AIP Conference Proceedings*, 772:56, 2005.

[39] T. Dietl, H. Ohno, F. Matsukura, J. Cibert, and D. Ferrand. Zener model description of ferromagnetism in zinc-blende magnetic semiconductors. *Science*, 287(5455):1019–1022, 2000.

[40] S. Donovan, A. Schwartz, and G. Grüner. Observation of an optical pseudogap in UPt_3. *Phys. Rev. Lett.*, 79:1401–1404, Aug 1997.

[41] S. V. Dordevic, D. N. Basov, N. R. Dilley, E. D. Bauer, and M. B. Maple. Hybridization gap in heavy fermion compounds. *Phys. Rev. Lett.*, 86:684–687, Jan 2001.

[42] P. V. Dorpe, V. F. Motsnyi, M. Nijboer, E. Goovaerts, V. I. Safarov, J. Das, W. V. Roy, G. Borghs, and J. D. Boeck. Highly efficient room temperature spin injection in a metal-insulator-semiconductor light-emitting diode. *Japanese Journal of Applied Physics*, 42(Part 2, No. 5B):L502–L504, 2003.

[43] T. Droubay, S. M. Heald, V. Shutthanandan, S. Thevuthasan, S. A. Chambers, and J. Osterwalder. Cr-doped TiO_2 anatase: A ferromagnetic insulator. *Journal of Applied Physics*, 97(4):046103, 2005.

[44] G. Ehlers, A. L. Cornelius, T. Fennell, M. Koza, S. T. Bramwell, and J. S. Gardner. Evidence for two distinct spin relaxation mechanisms in 'hot' spin ice $Ho_2Ti_2O_7$. *Journal of Physics: Condensed Matter*, 16(11):S635, 2004.

[45] G. Ehlers, A. L. Cornelius, M. Orendác, M. Kajnaková, T. Fennell, S. T. Bramwell, and J. S. Gardner. Dynamical crossover in 'hot' spin ice. *Journal of Physics: Condensed Matter*, 15(2):L9, 2003.

[46] T. Eimüller, P. Fischer, M. Köhler, M. Scholz, P. Guttmann, G. Denbeaux, S. Glück, G. Bayreuther, G. Schmahl, D. Attwood, et al. Transmission x-ray microscopy using X-ray magnetic circular dichroism. *Applied Physics A*, 73(6):697–701, 2001.

[47] J. Felber, R. Gähler, R. Golub, and K. Prechtel. Coherence volumes and neutron scattering. *Physica B: Condensed Matter*, 252(1):34–43, 1998.

[48] G. Fischer, N. Sanchez, W. Adeagbo, M. Lüders, Z. Szotek, W. M. Temmerman, A. Ernst, W. Hergert, and M. C. Muñoz. Room-temperature p-induced surface ferromagnetism: First-principles study. *Phys. Rev. B*, 84:205306, Nov 2011.

[49] P. Fischer, T. Eimüller, G. Schütz, and G. Denbeaux. Imaging magnetic domain structures with soft x-ray microscopy. *Structural Chemistry*, 14(1):39–47, 2003.

[50] I. C. for Diffraction Data. Jcpds no. 30-0413.

[51] C. for X-ray Optics. X-ray attenuation length calculator, www.henke.lbl.gov.

[52] A. J. Freeman, G. H. Lander, and C. Keller. *Handbook on the Physics and Chemistry of the Actinides*, volume 1. North-Holland, 1991.

[53] J. L. Friar, B. F. Gibson, G. L. Payne, A. M. Bernstein, and T. E. Chupp. Neutron polarization in polarized ^{3}He targets. *Phys. Rev. C*, 42:2310–2314, Dec 1990.

[54] T. Fukumura, Y. Yamada, H. Toyosaki, T. Hasegawa, H. Koinuma, and M. Kawasaki. Exploration of oxide-based diluted magnetic semiconductors toward transparent spintronics. *Proceedings of the Second Japan-US Workshop on Combinatorial Materials Science and Technology*, 223(1-3):62 – 67, 2004.

[55] P. Fulde. *Electron correlations in molecules and solids.* Springer series in solid-state sciences. Springer-Verlag, 1991.

[56] J. K. Furdyna. *Diluted Magnetic Semiconductors.* National Academy Press, 1991.

[57] J. S. Gardner, B. D. Gaulin, and D. M. Paul. Single crystal growth by the floating-zone method of a geometrically frustrated pyrochlore antiferromagnet, $Tb_2Ti_2O_7$. *Journal of Crystal Growth*, 191(4):740 – 745, 1998.

[58] J. S. Gardner, M. J. P. Gingras, and J. E. Greedan. Magnetic pyrochlore oxides. *Rev. Mod. Phys.*, 82(1):53, Jan 2010.

[59] D. Gibbs, D. R. Harshman, E. D. Isaacs, D. B. McWhan, D. Mills, and C. Vettier. Polarization and resonance properties of magnetic x-ray scattering in holmium. *Phys. Rev. Lett.*, 61:1241–1244, Sep 1988.

[60] V. L. Ginzburg and L. D. Landau. *Zh. Eksp. Teor. Fiz*, 20:1064, 1950.

[61] J. B. Goodenough. Theory of the role of covalence in the perovskite-type manganites La, M (II) MnO_3. *Phys. Rev.*, 100:564–573, Oct 1955.

[62] F. A. Grant. Properties of rutile (titanium dioxide). *Rev. Mod. Phys.*, 31(3):646–674, Jul 1959.

[63] G. Grübel and F. Zontone. Correlation spectroscopy with coherent x-rays. *Journal of Alloys and Compounds*, 362(1-2):3 – 11, 2004. Proceedings of the Sixth International School and Symposium on Synchrotron Radiation in Natural Science (ISSRNS).

[64] J. Grunzweig-Genossar, M. Kuznietz, and F. Friedman. Magnetic properties of uranium compounds with elements of the Va and VIa groups. I. compounds of Ux type. *Phys. Rev.*, 173:562–573, Sep 1968.

[65] A. Guinier. *X-ray Diffraction in crystals, imperfect cystals and amorphous bodies.* Dover Publications, 1994.

[66] M. Hagen, W. G. Stirling, and G. H. Lander. Temperature dependence of the low-frequency magnetic excitations in USb. *Phys. Rev. B*, 37:1846–1859, Feb 1988.

[67] B. Hälg and A. Furrer. Anisotropic exchange and spin dynamics in the type-I (-IA) antiferromagnets CeAs, CeSb, and USb: A neutron study. *Phys. Rev. B*, 34:6258–6279, Nov 1986.

[68] J. P. Hannon, G. T. Trammell, M. Blume, and D. Gibbs. X-ray resonance exchange scattering. *Physical Review Letters*, 61(10):1245, 1988.

[69] M. J. Harris, S. T. Bramwell, D. F. McMorrow, T. Zeiske, and K. W. Godfrey. Geometrical frustration in the ferromagnetic pyrochlore $Ho_2Ti_2O_7$. *Phys. Rev. Lett.*, 79(13):2554–2557, Sep 1997.

[70] J. P. Hill and D. F. McMorrow. Resonant exchange scattering: polarization dependence and correlation function. *Acta Crystallographica Section A: Foundations of Crystallography*, 52(2):236–244, 1996.

[71] R. Holm and W. Meissner. *Zeitschrift für Physik*, 74(11-12):715–735, 1932.

[72] N. H. Hong, J. Sakai, W. Prellier, A. Hassini, A. Ruyter, and F. Gervais. Ferromagnetism in transition-metal-doped TiO_2 thin films. *Phys. Rev. B*, 70:195204, Nov 2004.

[73] E. Hotta, A. Ochiai, Y. Suzuki, T. Shikama, K. Suzuki, Y. Haga, and T. Suzuki. Purification of USb and its de Haas van Alphen effect. *Journal of Alloys and Compounds*, 219(1-2):252 – 255, 1995.

[74] IN22 homepage. IN22 instrument layout, 2013.

[75] M. Ishimoto, H. Numakura, and M. Wuttig. Magnetoelastic damping in Fe-Ga solid-solution alloys. *Materials Science and Engineering: A*, 442(1-2):195 – 198, 2006. Proceedings of the 14th International Conference on Internal Friction and Mechanical Spectroscopy.

[76] Z. G. J. Mulak. *The Effective Crystal Field Potential*. Elsevier Science, 2000.

[77] E. Jakeman. *Photon Correlation and Light Beating Spectroscopy*. Plenum, New York, 1973.

[78] R. Janisch, P. Gopal, and N. A. Spaldin. Transition metal-doped TiO_2 and ZnO - present status of the field. *Journal of Physics: Condensed Matter*, 17(27):R657, 2005.

[79] J. Jensen and P. Bak. Spin waves in triple-$\mathbf{q}$ structures. *Phys. Rev. B*, 23:6180–6183, Jun 1981.

[80] X. Jiang, R. Wang, R. M. Shelby, R. M. Macfarlane, S. R. Bank, J. S. Harris, and S. S. P. Parkin. Highly spin-polarized room-temperature tunnel injector for semiconductor spintronics using MgO(100). *Phys. Rev. Lett.*, 94(5):056601, Feb 2005.

[81] J. Kanamori. Superexchange interaction and symmetry properties of electron orbitals. *Journal of Physics and Chemistry of Solids*, 10(2):87–98, 1959.

[82] T. C. Kaspar, T. Droubay, V. Shutthanandan, S. M. Heald, C. M. Wang, D. E. McCready, S. Thevuthasan, J. D. Bryan, D. R. Gamelin, A. J. Kellock, M. F. Toney, X. Hong, C. H. Ahn, and S. A. Chambers. Ferromagnetism and structure of epitaxial Cr-doped anatase TiO_2 thin films. *Phys. Rev. B*, 73(15):155327, Apr 2006.

[83] T. Kasuya. Electrical resistance of ferromagnetic metals. *Progress of Theoretical Physics*, 16(1):58–63, 1956.

[84] T. Kasuya. Fermi surface in USb due to orbit split $5f$ band. *Journal of the Physical Society of Japan*, 65(10):3394–3395, 1996.

[85] A. G. Khachaturyan and D. Viehland. Structurally heterogeneous model of extrinsic magnetostriction for Fe-Ga and similar magnetic alloys: Part I. decomposition and confined displacive transformation. *Metallurgical and Materials Transactions A*, 38(13):2308–2316, 2007.

[86] K. Knöpfle and L. M. Sandratskii. Multiple **k** magnetic structure and Fermi surface of USb. *Phys. Rev. B*, 63:014411, Dec 2000.

[87] H. W. Knott, G. H. Lander, M. H. Mueller, and O. Vogt. Search for lattice distortions in UN, UAs, and USb at low temperatures. *Phys. Rev. B*, 21:4159–4165, May 1980.

[88] L. Koester and A. Steyerl. *Springer Tracts in Modern Physics*, volume 80. Springer-Verlag., 1977.

[89] M. Köhler, J. Zweck, G. Bayreuther, P. Fischer, G. Schütz, G. Denbeaux, and D. Attwood. Micromagnetic investigation of sub-100-nm magnetic domains in atomically stacked Fe (001)/Au (001) multilayers. *Journal of magnetism and magnetic materials*, 240(1):79–82, 2002.

[90] S. Konings, C. Schüßler-Langeheine, H. Ott, E. Weschke, E. Schierle, H. Zabel, and J. B. Goedkoop. Magnetic domain fluctuations in an antiferromagnetic film observed with coherent resonant soft X-ray scattering. *Phys. Rev. Lett.*, 106:077402, Feb 2011.

[91] S. M. Koohpayeh, D. Fort, and J. S. Abell. The optical floating zone technique: A review of experimental procedures with special reference to oxides. *Progress in Crystal Growth and Characterization of Materials*, 54(3-4):121 – 137, 2008.

[92] S. M. Koohpayeh, D. Fort, A. I. Bevan, A. J. Williams, and J. S. Abell. Study of ferromagnetism in Co-doped rutile powders and float-zone grown single crystals. *Journal of Magnetism and Magnetic Materials*, 320(6):887 – 894, 2008.

[93] S. M. Koohpayeh, J.-J. Wen, M. Mourigal, S. E. Dutton, R. J. Cava, C. L. Broholm, and T. M. McQueen. Optical floating zone crystal growth and magnetic properties of $MgCr_2O_4$. *Journal of Crystal Growth*, 2013.

[94] S. M. Koohpayeh, A. J. Williams, J. S. Abell, J. Lim, and E. Blackburn. Cr-doped TiO_2 (rutile): Ferromagnetism in bulk form? *Journal of Applied Physics*, 108(7):073919, 2010.

[95] N. Koshizuka and S. Ushioda. Inelastic-light-scattering study of magnon softening in $ErFeO_3$. *Phys. Rev. B*, 22:5394–5399, Dec 1980.

[96] H. A. Kramers. L'interaction entre les atomes magnétogènes dans un cristal paramagnétique. *Physica*, 1:182–192, 1934.

[97] A. Kratzer. *μSR-Messungen an Uranverbindgungen und Aufbau eines Meßplatzes für gepulste Myonenstrahlen.* PhD thesis, Technische Universität München, 1989.

[98] W. Kuch, L. I. Chelaru, F. Offi, J. Wang, M. Kotsugi, and J. Kirschner. Three-dimensional noncollinear antiferromagnetic order in single-crystalline FeMn ultrathin films. *Phys. Rev. Lett.*, 92:017201, Jan 2004.

[99] H. Kumigashira, T. Ito, A. Ashihara, H.-D. Kim, H. Aoki, T. Suzuki, H. Yamagami, T. Takahashi, and A. Ochiai. High-resolution angle-resolved photoemission study of USb: Dual character of $5f$ electrons. *Phys. Rev. B*, 61:15707–15713, Jun 2000.

[100] M. Kuznietz, P. Burlet, J. Rossat-Mignod, and O. Vogt. The magnetic phase diagram of the $UAs_{1-x}Se_x$ system studied by neutron diffraction from single crystals. *Journal of Magnetism and Magnetic Materials*, 69(1):12 – 26, 1987.

[101] M. Kuznietz, G. H. Lander, and Y. Baskin. Magnetic phase diagram of the $UP_{1-x}S_x$ system. *Journal of Applied Physics*, 40(3):1130–1131, 1969.

[102] M. Kuznietz, G. H. Lander, and F. P. Campos. Antiferromagnetic structures of USb and UBi. *Journal of Physics and Chemistry of Solids*, 30(6):1642 – 1643, 1969.

[103] G. H. Lander. Studies of magnetism with synchrotron x-rays. *Journal of alloys and compounds*, 250(1):544–551, 1997.

[104] G. H. Lander. Magnetic scattering with synchrotrons: new developments. *Journal of magnetism and magnetic materials*, 242:3–8, 2002.

[105] G. H. Lander and P. Burlet. On the magnetic structure of actinide monopnictides. *Physica B: Condensed Matter*, 215(1):7 – 21, 1995.

[106] G. H. Lander, M. Kuznietz, and D. E. Cox. Neutron-diffraction study of magnetic ordering in $UP_{0.75}S_{0.25}$. *Physical Review*, 188(2):963, 1969.

[107] G. H. Lander and M. H. Mueller. Magnetically induced lattice distortions in actinide compounds. *Phys. Rev. B*, 10:1994–2003, Sep 1974.

[108] G. H. Lander, M. H. Mueller, and J. F. Reddy. Magnetic phase diagram of the UAs-US system. *Phys. Rev. B*, 6:1880–1888, Sep 1972.

[109] G. H. Lander, M. H. Mueller, D. M. Sparlin, and O. Vogt. Neutron diffraction study of USb: The ordered state. *Physical Review B*, 14(11):5035–5045, 1976.

[110] G. H. Lander and S. M. Shapiro. Possible observation of a new magnetic phase transition in USb. *Physica B: Condensed Matter*, 213:125–127, 1995.

[111] G. H. Lander, S. K. Sinha, D. M. Sparlin, and O. Vogt. Spin correlations in actinide materials: A neutron study of USb. *Phys. Rev. Lett.*, 40:523–526, Feb 1978.

[112] G. H. Lander and W. G. Stirling. Neutron-inelastic-scattering measurements on uranium antimonide. *Phys. Rev. B*, 21:436–447, Jan 1980.

[113] S. Langridge, W. G. Stirling, G. H. Lander, and J. Rebizant. Resonant magnetic X-ray-scattering studies of NpAs. I. magnetic and lattice structure. *Phys. Rev. B*, 49:12010–12021, May 1994.

[114] M. Laver, C. Mudivarthi, J. R. Cullen, A. B. Flatau, W.-C. Chen, S. M. Watson, and M. Wuttig. Magnetostriction and magnetic heterogeneities in iron-gallium. *Phys. Rev. Lett.*, 105:027202, Jul 2010.

[115] J. Leciejewicz, A. Murasik, and R. Troć. The antiferromagnetic ordering in uranium monoarsenide and monoantimonide. *Physica Status Solidi (b)*, 30(1):157–162, 1968.

[116] J. Leciejewicz, A. Murasik, R. Troć, and T. Palewski. The influence of sulphur substitution on the magnetic properties of uranium monoarsenide. *Physica Status Solidi (b)*, 46(1):391–395, 1971.

[117] C. W. Lee. *Ber. Dtsch. Keram. Ges.*, 47:169, 1970.

[118] J. A. Lim, E. Blackburn, N. Magnani, A. Hiess, L.-P. Regnault, R. Caciuffo, and G. H. Lander. Unexpected phase locking of magnetic fluctuations in the multi-**k** magnet USb. *Phys. Rev. B*, 87:064421, Feb 2013.

[119] L. Liu, J. Kang, Y. Wang, X. Zhang, and R. Han. Hydrogen annealing induced the enhancement of ferromagnetism in Cr-Doped TiO_2 anatase films. *Japanese Journal of Applied Physics*, 47(12):8787–8789, 2008.

[120] F. Livet, F. Bley, J. Mainville, R. Caudron, S. G. J. Mochrie, E. Geissler, G. Dolino, D. Abernathy, G. Grübel, and M. Sutton. Using direct illumination CCDs as high-resolution area detectors for x-ray scattering. *Nuclear Instruments and Methods in Physics Research Section A: Accelerators, Spectrometers, Detectors and Associated Equipment*, 451(3):596 – 609, 2000.

[121] M. J. Longfield, W. G. Stirling, E. Lidström, D. Mannix, G. H. Lander, A. Stunault, G. J. McIntyre, K. Mattenberger, and O. Vogt. $U(As_{1-x})Se_x$ solid solutions. I. resonant x-ray and neutron scattering study of the magnetic phase diagram. *Phys. Rev. B*, 63:134401, Feb 2001.

[122] S. W. Lovesey. *Theory of neutron scattering from condensed matter*, volume 1. Oxford University Press, 1986.

[123] S. W. Lovesey. *Theory of neutron scattering from condensed matter*, volume 2. Oxford University Press, 1986.

[124] F. Lucassen, M. Koch-Müller, M. Taran, and G. Franz. Coupled H and Nb, Cr, and V trace element behavior in synthetic rutile at 600 C, 400 MPa and possible geological application. *American Mineralogist*, 98(1):7–18, 2013.

[125] D. Lumma, L. B. Lurio, S. G. J. Mochrie, and M. Sutton. Area detector based photon correlation in the regime of short data batches: Data reduction for dynamic X-ray scattering. *Review of Scientific Instruments*, 71(9):3274–3289, 2000.

[126] N. Magnani, R. Caciuffo, G. H. Lander, A. Hiess, and L.-P. Regnault. Polarized-neutron-scattering study of the spin-wave excitations in the 3-k ordered phase of uranium antimonide. *Journal of Physics: Condensed Matter*, 22(11):116002, 2010.

[127] K. Matsuhira, Y. Hinatsu, and T. Sakakibara. Novel dynamical magnetic properties in the spin ice compound $Dy_2Ti_2O_7$. *Journal of Physics: Condensed Matter*, 13(31):L737, 2001.

[128] Y. Matsumoto, M. Murakami, T. Hasegawa, T. Fukumura, M. Kawasaki, P. Ahmet, K. Nakajima, T. Chikyow, and H. Koinuma. Structural control and combinatorial doping of titanium dioxide thin films by laser molecular beam epitaxy. *Applied Surface Science*, 189(3-4):344 – 348, 2002.

[129] Y. Matsumoto, M. Murakami, T. Shono, T. Hasegawa, T. Fukumura, M. Kawasaki, P. Ahmet, T. Chikyow, S.-y. Koshihara, and H. Koinuma. Room-temperature ferromagnetism in transparent transition metal-doped titanium dioxide. *Science*, 291(5505):854–856, 2001.

[130] F. Mezei. Novel polarized neutron devices: supermirror and spin component amplifier. *Commun. Phys*, 1:81–85, 1976.

[131] F. Mezei. *Neutron spin echo spectroscopy*. Springer, 2003.

[132] B. Mills. Public Domain, 2007.

[133] S. G. J. Mochrie, A. M. Mayes, A. R. Sandy, M. Sutton, S. Brauer, G. B. Stephenson, D. L. Abernathy, and G. Grübel. Dynamics of block copolymer micelles revealed by X-ray intensity fluctuation spectroscopy. *Phys. Rev. Lett.*, 78:1275–1278, Feb 1997.

[134] R. M. Moon, T. Riste, and W. C. Koehler. Polarization analysis of thermal-neutron scattering. *Phys. Rev.*, 181:920–931, May 1969.

[135] S. Mughabghab, M. Divadeenam, and N. Holden. Neutron cross sections, vol. 1 academic. *New York*, page 3, 1981.

[136] L. Néel. Propriétées magnétiques des ferrites; férrimagnétisme et antiferromagnétisme. *Annales de Physique (Paris)*, pages 137–198, 1948.

[137] F. Nolting, A. Scholl, J. Stöhr, J. W. Seo, J. Fompeyrine, H. Siegwart, J.-P. Locquet, S. Anders, J. Lüning, E. E. Fullerton, et al. Direct observation of the alignment of ferromagnetic spins by antiferromagnetic spins. *Nature*, 405(6788):767–769, 2000.

[138] P. S. Normile, M. Rotter, C. Detlefs, J. Jensen, P. C. Canfield, and J. A. Blanco. Magnetic ordering in $GdNi_2B_2C$ revisited by resonant X-ray scattering: Evidence for the double-q model. *Physical Review B*, 88(5):054413, 2013.

[139] W. Nuttall, S. Perry, W. Stirling, P. Mitchell, S. Kilcoyne, and R. Cywinski. Antiferromagnetic critical phenomena in USb. *Physica B: Condensed Matter*, 315(1-3):179 – 186, 2002.

[140] A. Ochiai, Y. Suzuki, T. Shikama, K. Suzuki, E. Hotta, Y. Haga, and T. Suzuki. Transport properties and specific heat of UTe and USb. *Physica B: Condensed Matter*, 199(0):616 – 618, 1994.

[141] H. Ohldag, A. Scholl, F. Nolting, S. Anders, F. U. Hillebrecht, and J. Stöhr. Spin reorientation at the antiferromagnetic NiO(001) surface in response to an adjacent ferromagnet. *Phys. Rev. Lett.*, 86:2878–2881, Mar 2001.

[142] H. Ohno. Making nonmagnetic semiconductors ferromagnetic. *Science*, 281(5379):951–956, 1998.

[143] M. Opel. Spintronic oxides grown by laser-MBE. *Journal of Physics D: Applied Physics*, 45(3):033001, 2012.

[144] H. Ott, C. Schüßler-Langeheine, E. Schierle, A. Y. Grigoriev, V. Leiner, H. Zabel, G. Kaindl, and E. Weschke. Magnetic X-ray scattering at the M_5 absorption edge of Ho. *Phys. Rev. B*, 74(9):094412, Sep 2006.

[145] C. Pappas, F. Mezei, A. Triolo, and R. Zorn. Going to the limits of NSE. *Physica B: Condensed Matter*, 356(1-4):206 – 212, 2005.

[146] S. K. S. Patel and N. S. Gajbhiye. Strong correlation between induced ferromagnetism and oxygen deficiency in hydrothermally synthesized Cu-doped TiO_2 nanorods. In *SPIE NanoScience+ Engineering*, pages 84611T–84611T. International Society for Optics and Photonics, 2012.

[147] S. K. S. Patel, S. Kurian, and N. S. Gajbhiye. Phase dependent room-temperature ferromagnetism of Fe-doped TiO_2 nanorods. 2012.

[148] S. J. Pearton, W. H. Heo, M. Ivill, D. P. Norton, and T. Steiner. Dilute magnetic semiconducting oxides. *Semiconductor Science and Technology*, 19(10):R59, 2004.

[149] R. Pecora. *Dynamic light scattering: applications of photon correlation spectroscopy*. Springer, 1985.

[150] J. F. Peters, M. A. de Fries, J. Miguel, O. Toulemounde, and J. Goedkoop. *ESRF Newsletter*, 34:15, 2000.

[151] P. V. Radovanovic and D. R. Gamelin. High-temperature ferromagnetism in Ni^{2+}-doped ZnO aggregates prepared from colloidal diluted magnetic semiconductor quantum dots. *Phys. Rev. Lett.*, 91(15):157202, Oct 2003.

[152] A. P. Ramirez, A. Hayashi, R. J. Cava, R. Siddhartan, and B. S. Shastry. Zero-point entropy in 'spin ice'. *Nature*, 399:333, 1999.

[153] A. Robert, E. Wandersman, E. Dubois, V. Dupuis, and R. Perzynski. Glassy dynamics and aging in a dense ferrofluid. *EPL (Europhysics Letters)*, 75(5):764, 2006.

[154] D. Rodbell and R. DeVries. On the decomposition of CrO_2 in air. *Materials Research Bulletin*, 2(4):491 – 495, 1967.

[155] J. Rossat-Mignod, P. Burlet, S. Quezel, and O. Vogt. Magnetic ordering in cerium and uranium monopnictides. *Physica B+C*, 102(1-3):237 – 248, 1980.

[156] M. A. Ruderman and C. Kittel. Indirect exchange coupling of nuclear magnetic moments by conduction electrons. *Phys. Rev.*, 96(1):99, Oct 1954.

[157] J. Rudolph, D. Hagele, H. M. Gibbs, G. Khitrova, and M. Oestreich. Laser threshold reduction in a spintronic device. *Applied Physics Letters*, 82(25):4516–4518, 2003.

[158] L. Sangaletti, M. C. Mozzati, P. Galinetto, C. B. Azzoni, A. Speghini, M. Bettinelli, and G. Calestani. Ferromagnetism on a paramagnetic host background:

the case of rutile TM:TiO_2 single crystals (TM = Cr, Mn, Fe, Co, Ni, Cu). *Journal of Physics: Condensed Matter*, 18(32):7643, 2006.

[159] K. Sato and H. Katayama-Yoshida. Materials and device design with ZnO-based diluted magnetic semiconductors. *MRS Proceedings*, 666, 2001.

[160] K. Sato and H. Katayama-Yoshida. First principles materials design for semiconductor spintronics. *Semiconductor Science and Technology*, 17(4):367, 2002.

[161] O. Schaerpf and N. Stuesser. Recent progress in neutron polarizers. *Nuclear Instruments and Methods in Physics Research Section A: Accelerators, Spectrometers, Detectors and Associated Equipment*, 284(1):208 – 211, 1989.

[162] R. I. Schermer and M. Blume. Polarization effects in slow-neutron scattering. iii. nuclear polarization. *Physical Review*, 166:554–561, 1968.

[163] H. Schmidt. Phase transition of perovskite-type ferroelectrics. *Phys. Rev.*, 156:552–561, Apr 1967.

[164] J. Schoenes, B. Frick, and O. Vogt. Transport properties of uranium monochalcogenide and monopnictide single crystals. *Phys. Rev. B*, 30:6578–6585, Dec 1984.

[165] M. P. Schulhof, P. Heller, R. Nathans, and A. Linz. Critical magnetic scattering in manganese fluoride. *Phys. Rev. B*, 1:2304–2311, Mar 1970.

[166] V. F. Sears. Neutron scattering lengths and cross sections. *Neutron News*, 3(3):26–37, 1992.

[167] K. A. Seu, S. Roy, J. J. Turner, S. Park, C. M. Falco, and S. D. Kevan. Cone phase and magnetization fluctuations in Au/Co/Au thin films near the spin-reorientation transition. *Phys. Rev. B*, 82:012404, Jul 2010.

[168] A. A. Sharif, A. Misra, and T. E. Mitchell. Strength of $MoSi_2$-based crystals at ultra-high temperature. *Scripta Materialia*, 52(5):399 – 402, 2005.

[169] O. G. Shpyrko, E. D. Isaacs, J. M. Logan, Y. Feng, G. Aeppli, R. Jaramillo, H. C. Kim, T. F. Rosenbaum, P. Zschack, M. Sprung, et al. Direct measurement of antiferromagnetic domain fluctuations. *Nature*, 447(7140):68–71, 2007.

[170] C. G. Shull and J. S. Smart. Detection of antiferromagnetism by neutron diffraction. *Phys. Rev.*, 76:1256–1257, Oct 1949.

[171] I. Sikharulidze, I. P. Dolbnya, A. Fera, A. Madsen, B. I. Ostrovskii, and W. H. de Jeu. Smectic membranes in motion: Approaching the fast limits of X-ray photon correlation spectroscopy. *Phys. Rev. Lett.*, 88:115503, Feb 2002.

[172] M. S. Silberberg, R. Duran, C. G. Haas, and A. D. Norman. *Chemistry: The molecular nature of matter and change*, volume 4. McGraw-Hill New York, 2006.

[173] G. P. Singh, S. Ram, J. Eckert, and H. J. Fecht. Synthesis and morphological stability in CrO_2 single crystals of a half-metallic ferromagnetic compound. In *Journal of Physics: Conference Series*, volume 144, page 012110. IOP Publishing, 2009.

[174] R. K. Singhal, S. Kumar, P. Kumari, Y. T. Xing, and E. Saitovitch. Evidence of defect-induced ferromagnetism and its "switch" action in pristine bulk TiO_2. *Applied Physics Letters*, 98(9):092510–092510, 2011.

[175] S. K. Sinha, G. R. Kline, C. Stassis, N. Chesser, and N. Wakabayashi. Neutron scattering study of the spin dynamics and spin-wave form factor of chromium. *Phys. Rev. B*, 15:1415–1421, Feb 1977.

[176] J. Snyder, J. S. Slusky, R. J. Cava, and P. Schiffer. How 'spin ice' freezes. *Nature*, 413:48, 2001.

[177] Y.-A. Soh, G. Aeppli, N. D. Mathur, and M. G. Blamire. Mesoscale magnetism at the grain boundaries in colossal magnetoresistive films. *Phys. Rev. B*, 63:020402, Dec 2000.

[178] S. Somiya, S. Hirano, and S. Kamiya. Phase relations of the Cr_2O_3 - TiO_2 system. *Journal of Solid State Chemistry*, 25(3):273 – 284, 1978.

[179] D. L. Source. Beamlines I16: Materials and Magnetism - Homepage, 2012.

[180] G. L. Squires. *Introduction to the theory of thermal neutron scattering*. Cambrdige University Press, 1978.

[181] S.-J. Sun and H.-H. Lin. Softening of spin-wave stiffness near the ferromagnetic phase transition in diluted magnetic semiconductors. *The European Physical Journal B - Condensed Matter and Complex Systems*, 49(4):403–406, 2006.

[182] M. Sutton. A review of x-ray intensity fluctuation spectroscopy. *C. R. Physique*, 9(5):657–667, 2008.

[183] T. Takahashi, N. Sato, T. Yokoya, A. Chainani, T. Morimoto, and T. Komatsubara. Dual character of $5f$ electrons in UPd_2Al_3 observed by high-resolution photoemission spectroscopy. *Journal of the Physical Society of Japan*, 65(1):156–159, 1996.

[184] C. C. Tang, W. G. Stirling, G. H. Lander, D. Gibbs, W. Herzog, P. Carra, B. T. Thole, K. Mattenberger, and O. Vogt. Resonant magnetic x-ray scattering in a series of uranium compounds. *Phys. Rev. B*, 46:5287–5297, Sep 1992.

[185] A. C. Thompson, D. Vaughan, et al. *X-ray data booklet*. Lawrence Berkeley National Laboratory, University of California Berkeley, CA, 2001.

[186] O. K. C. Tsui and S. G. J. Mochrie. Dynamics of concentrated colloidal suspensions probed by X-ray correlation spectroscopy. *Phys. Rev. E*, 57(2):2030–2034, Feb 1998.

[187] J. J. Turner, K. J. Thomas, J. P. Hill, M. A. Pfeifer, K. Chesnel, Y. Tomioka, Y. Tokura, and S. D. Kevan. Orbital domain dynamics in a doped manganite. *New Journal of Physics*, 10(5):053023, 2008.

[188] L. Van Hove. Correlations in space and time and born approximation scattering in systems of interacting particles. *Physical Review*, 95(1):249, 1954.

[189] S. Vitale, A. Cavalleri, M. Cerdonio, A. Maraner, and G. A. Prodi. Thermal equilibrium noise with 1/f spectrum in a ferromagnetic alloy: Anomalous temperature dependence. *Journal of Applied Physics*, 76(10):6332–6334, 1994.

[190] J. Vogel, W. Kuch, M. Bonfim, J. Camarero, Y. Pennec, F. Offi, K. Fukumoto, J. Kirschner, A. Fontaine, and S. Pizzini. Time-resolved magnetic domain imaging by x-ray photoemission electron microscopy. *Applied Physics Letters*, 82(14):2299–2301, 2003.

[191] Z. Wang, J. Tang, H. Zhang, V. Golub, L. Spinu, and L. D. Tung. Ferromagnetism in chromium-doped reduced-rutile titanium dioxide thin films. *Journal of Applied Physics*, 95(11):7381–7383, 2004.

[192] A. D. B. Woods, T. M. Holden, B. M. Powell, and M. W. Stringfellow. Soft spin-wave modes and the cone-to-spiral transition in holmium metal. *Phys. Rev. Lett.*, 23:81–83, Jul 1969.

[193] F. Yakhou, A. Létoublon, F. Livet, M. De Boissieu, and F. Bley. Magnetic domain fluctuations observed by coherent X-ray scattering. *Journal of magnetism and magnetic materials*, 233(1):119–122, 2001.

[194] H. Yamagami. Fully relativistic noncollinear magnetism in spin-density-functional theory: Application to USb by means of the fully relativistic spin-polarized LAPW method. *Phys. Rev. B*, 61:6246–6256, Mar 2000.

[195] S. D. Yoon, Y. Chen, A. Yang, T. L. Goodrich, X. Zuo, D. A. Arena, K. Ziemer, C. Vittoria, and V. G. Harris. Oxygen-defect-induced magnetism to 880 K in semiconducting anatase $TiO_{2-\delta}$ films. *Journal of Physics: Condensed Matter*, 18(27):L355, 2006.

[196] K. Yosida. Magnetic properties of Cu-Mn alloys. *Phys. Rev.*, 106(5):893–898, Jun 1957.

[197] C. Zener. Interaction between the d shells in the transition metals. *Phys. Rev.*, 81(3):440–444, Feb 1951.

[198] S. S. Zumdahl and D. J. DeCoste. *Chemical principles*. Brooks/Cole, 2012.